Trinity College Dublin
Coláiste na Tríonóide, Baile Átha Cliath
The University of Dublin

New Technologies for Ultra-low Dose-rate Digital Imaging in the STEM

A PhD thesis by:

Tiarnan Mullarkey

Under the supervision of:

Lewys Jones

Submitted to Trinity College Dublin

for the degree of:

Doctor of Philosophy

School of Physics

August 2023

Declarations

I have read and I understand the plagiarism provisions in the General Regulations of the University Calendar for the current year, found at http://www.tcd.ie/calendar.

I have also completed the Online Tutorial on avoiding plagiarism 'Ready Steady Write', located at https://libguides.tcd.ie/plagiarism/ready-steady-write.

I declare that this thesis has not been submitted as an exercise for a degree at this or any other university and it is entirely my own work.

I agree to deposit this thesis in the University's open access institutional repository or allow the Library to do so on my behalf, subject to Irish Copyright Legislation and Trinity College Library conditions of use and acknowledgement.

Parts of this thesis have been previously published by the author, and are cited appropriately wherever reproduced. Any figures reproduced from other publications are cited, including reference to the applicable licence. All other work is by the author, except for the following:

- The human monocyte derived macrophage sample was provided by A. Porter and K. Müller.
- The silver nanowire sample was provided by A. Sanchez.
- The first version of the signal streaking code was written by M. Geever.
- The simulation of STO was provided by P. McBean.
- The STEM-DPC simulations were provided by J. M. Bekkevold.

Contents

Abstract

Electron microscopy arose from the need to image materials beyond the resolution optical microscopes could achieve. Though taking many years and technological advancements, the modern scanning transmission electron microscope (STEM) can readily image a diverse range of materials at atomic resolution. However, using such intense electron beams causes sample-damage to such an extent that it often becomes the limiting factor, instead of the microscope's performance.

Therefore, new low-dose imaging techniques are required. Imaging with a low beam current and a short pixel dwell time is identified as a universally accessible approach to low-dose imaging. However, images captured under these conditions are often excessively noisy due to signal streaking, caused by the "streaking" of signal from one pixel into subsequent pixels due to finite detector response times. When imaging at short dwell times this becomes unavoidable, and a solution is needed.

New hardware which digitises the signal from the detector is developed, recording all electrons with equal intensity and localising them to a single time value, eliminating signal streaking. As *only* electrons are detected as signal, Gaussian noise and detector afterglow are also eliminated. Image comparisons of a biological tissue are shown, demonstrating how the technique produces low-dose, high signal-to-noise ratio images of fragile specimens. A lamella is imaged to show the absence of detector afterglow and a cluster of five silicon atoms on graphene is imaged at 31 f.p.s., demonstrating both high temporal and spatial resolution in the same dataset.

As all electrons are now recorded with equal intensity, detector inhomogeneity is reduced. Eight detector maps are analysed, with their flatness, roundness, and smoothness values improving by 6.78 %, 9.97 %, and 32.06 % respectively after digitisation. The response time of these same detectors range from 200 ns to over 1.5 μs, but have an instant response in the digital signal. Signal streaking is added to image simulations to isolate its effects, and is used to show the loss of information in Fourier transform of images with signal streaking, allowing detector performance to be evaluated virtually.

The line flyback time occupies an increasingly larger portion of the imaging time with reducing dwell time, lowering scanning efficiency. While the line flyback time can be reduced, this results in a compression artefact due to hysteresis in the scanning coils. A semi-empirical model of this compression is created, allowing it to be corrected at any imaging settings. This increases scanning efficiency by 20 %, with the route to increase this a further 25 % identified.

The findings of this thesis are accessible, retrofittable, and sustainable ways to increase microscope performance, whether to allow low-dose imaging, or extend the lifespan of existing microscopes.

Acknowledgements

I extend my heartfelt appreciation to all those who supported me during my PhD, both academically and emotionally, whether they are individuals or institutions.

It would be difficult to overstate the guidance of my supervisor Lewys Jones. Never short of ideas for new experiments (or feedback!) and having the uncanny ability to explain any concept in a way I was sure to understand. I also owe thanks to my co-supervisor Alexandra Porter, particularly for providing an excellent sample and a wealth of information alongside it. Another person especially deserving of praise is Jonathan Peters. His expertise in seemingly all research areas meant that I was never short of support, and I consider it a privilege to have been able to spend much of my PhD working alongside him.

I could not fail to mention the entire Ultramicroscopy Research Group, and indeed other researchers and staff of the Advanced Microscopy Laboratory (AML). The benefits of their assistance are rivalled only by their ability to create such an incredible place to work. Beyond the AML, I must also thank my cohort of the Centre for Doctoral Training in the Advanced Characterisation of Materials for feeling like a second, extended research family.

The entire team of technical and support staff deserve especial recognition for being the beating heart, and where necessary, the life support system, of the AML. Keeping such a variety of instruments performing at such a high standard, especially through the unexpected, is thoroughly impressive. I must single out Clive Downing for working closely on many of my projects and his in-depth knowledge of the microscopes. I hope it is reflection upon his skill, and not my own knowledge, that I have never been able to ask him a question he could not answer.

I had the privilege of spending two months in the University of Tokyo during my PhD, and I owe much to those who made this daunting experience easier. I am extremely grateful to Yuichi Ikuhara, Naoya Shibata, Ryo Ishikawa, and other members of the Crystal Interface Laboratory for making me feel welcome despite being on the opposite side of the globe where I could not speak the language. In particular, the numerous hours Ryo Ishikawa spent at the microscope with me (and also assisting in my visa application) were essential to the great outcomes of my visit, and my fantastic experience in such a beautiful country.

Last but not least, I am extremely grateful to my friends, family, and Jill, for all their love and support. A PhD is a difficult journey, one I'm not sure would have been possible without such brilliant network of people outside of work. I truly hope I did not neglect to mention anyone who has supported me during my PhD, and I reiterate my sincere gratitude to all.

And, of course, I must mention my dog, Louis.

COVID-19 Impact Statement

As part of the Centre for Doctoral Training in the Advanced Characterisation of Materials, my PhD began by spending three months in London with my time divided between Imperial College London and University College London. While there I received training on various characterisation techniques, before joining the Ultramicroscopy Research Group in January 2020 and beginning my project.

Upon return, much of my time was spent on different inductions and training, and I returned to the United Kingdom again in February for another week of training. Just one week after this, the AML closed due to COVID-19. Unsurprisingly, at this point I had completed very little work related to my project. Thankfully however, some previous data captured during a final-year undergraduate research project was available for analysis, and lead to publication of my first paper when experimental work was not possible.

The laboratory opened in a minimal capacity during Autumn 2020, and I began training to operate the STEM as an independent user. However, due to a surge in COVID-19 cases in mid-Winter restrictions increased and this training was paused. Although cases rose and fell, major restrictions remained in place until mid-Autumn 2021. During this period, any data collection was reliant on the availability of others to operate the microscopes, and so progress was possible, but slower than it would have been otherwise. As conferences moved online during this period, I had the opportunity to present at more conferences than I would have been able to travel to in-person under normal circumstances, which was one silver-lining.

After this, with reliable laboratory access I could begin to independently obtain data, and progress more quickly with data capture. Any restrictions due to COVID-

19 at this point were minimal, and thankfully progress has been smooth since then. Overall, the main effect of COVID-19 on my research was heavily delaying my ability to independently capture data, however this did mean front-loading more writing, presentation and poster making. Although this did have a small net loss in data captured overall, I felt the effect was thankfully minimal enough to proceed with the initial timeline of my PhD, finishing in time for August 2023.

Publications List

Original Articles

Peters, J.J.P., **Mullarkey, T.**, Hedley, E., Müller, K., Porter, A., Mostaed, A., Jones, L., *Electron counting detectors in scanning transmission electron microscopy via hardware signal processing*, Nature Communications, accepted for publication.

Mullarkey, T., Geever, M., Peters, J.J.P., Griffiths, I., Nellist, P., Jones, L., *How Fast is Your Detector? The Effect of Temporal Response on Image Quality*, Microscopy and Microanalysis **29** (2023), 1402 - 1408.

Peters, J.J.P., **Mullarkey, T.**, Gott, J.A., Nelson, E., Jones, L., *Interlacing in atomic resolution scanning transmission electron microscopy*, Microscopy and Microanalysis **29** (2023), 1373 - 1379.

Gambini, L., **Mullarkey, T.**, Jones, L., Sanvito, S., *Machine-learning approach for quantified resolvability enhancement of low-dose STEM data*, Machine Learning: Science and Technology **4** (2023), 015025.

Mullarkey, T., Peters, Jonathan J.P., Downing, C., Jones, L., *Using your beam efficiently: reducing electron dose in the STEM via flyback compensation*, Microscopy and Microanalysis **28** (2022), 1428 - 1436.

Mullarkey, T., Downing, C., Jones, L., *Development of a practicable digital pulse readout for dark-field STEM*, Microscopy and Microanalysis **27** (2021), 99 - 108.

Conference Proceedings

Bekkevold, J.M., Peters, J.J.P., **Mullarkey, T.**, Jones, L., *Retrofitting and Reconfiguring Existing Microscopes for Digital DPC: an Accessible Approach to Low-dose Phase Mapping*

Peters, J.J.P., Moldovan, G., **Mullarkey, T.**, Jones, L., *Developments in scan strategies for high-speed and low-dose microscopy*, MMC 2023 Incorporating EMAG 2023, Manchester, United Kingdom, July 4-6 (2023).

Peters, J.J.P., **Mullarkey, T.**, Moldovan, G., Garel, J., Jones, L., *Making Every Electron Count: Improving STEM Quantification, Speed, and Data Throughput with Solid State Detectors and Pulse Counting Hardware*, 16MCM, 16$^{\text{th}}$ Multinational Congress on Microscopy, Brno, Czech Republic, September 4-9 (2022).

Mullarkey, T., Peters, J.J.P., Geever, M., Jones, L., *How Low Can You Go: Pushing the Limits of Dose and Frame-time in the STEM*, M&M 2022, Microscopy and Microanalysis

2022 Meeting, Portland, Oregon, July 31 - August 4 (2022).

Peters, J.J.P., **Mullarkey, T.**, Jones, L., *Improving the Noise Floor and Speed of Your Detector: A Modular Hardware Approach for Under $1000*, M&M 2022, Microscopy and Microanalysis 2022 Meeting, Portland, Oregon, July 31 - August 4 (2022).

Mullarkey, T., Peters, J.J.P., Moldovan, G., Garel, J., Jones, L., *Fast Solid-state Segmented Detectors: Improvements and Implications for DPC-STEM*, M&M 2022, Microscopy and Microanalysis 2022 Meeting, Portland, Oregon, July 31 - August 4 (2022).

Peters, J.J.P., **Mullarkey, T.**, Gott, J.A., Jones, L., *Fast frame-rates from STEM interlacing: Two frames for the price of one?*, EMAG 2022: Multidimensional Electron Microscopy, London, United Kingdom, July 5-7 (2022).

Peters, J.J.P., **Mullarkey, T.**, Jones, L., *Improving the Noise Floor and Speed of Your Detector: A Modular Hardware Approach for Under £1000*, EMAG 2022: Multidimensional Electron Microscopy, London, United Kingdom, July 5-7 (2022).

Mullarkey, T., Geever, M., Peters, J.J.P., Mostaed, A., Jones, L., *How Fast is Your Detector? The Effect of Temporal Response on Image Quality*, 2nd Joint Symposium of Microscopy Society of Ireland and Scottish Microscopy Society, Galway, Ireland, April 6-8 (2022).

Peters, J.J.P., **Mullarkey, T.**, Gott, J.A., Jones, L., *Fast frame-rates from STEM interlacing: Two frames for the price of one?*, 2nd Joint Symposium of Microscopy Society of Ireland and Scottish Microscopy Society, Galway, Ireland, April 6-8 (2022).

Mullarkey, T., Peters, J.J.P., Downing, C., Jones, L., *Expanding Performance and Usability of High-speed / Low-dose STEM Scanning*, MC 2021, Microscopy Conference 2021, Online, August 22-26 (2021).

Peters, J.J.P., **Mullarkey, T.**, Downing, C., Jones, L., *Increasing the Usable Frame-rate of you Existing STEM*, MMC 2021 Incorporating EMAG 2021, Microscience Microscopy Congress 2021, Online, July 6-8 (2021).

Mullarkey, T., Peters, J.J.P., Downing, C., Jones, L., *Expanding Performance and Usability of High-speed / Low-dose STEM Scanning*, MMC 2021 Incorporating EMAG 2021, Microscience Microscopy Congress 2021, Online, July 6-8 (2021).

Mullarkey, T., Peters, J.J.P., Downing, C., Jones, L., *Enabling the Use of Low Flyback Times in the STEM via Fast-scan Flyback Correction*, Microscopy Society of Ireland Symposium 2021, Queen's University Belfast, Online, January 6-8 (2021).

Mullarkey, T., Downing, C., Jones, L., *Retaining Precision at Low-dose and High-speed*

STEM Imaging Conditions, Virtual Early Career European Microscopy Congress, Online, November 24-26 (2020).

Mullarkey, T., Downing, C., Jones, L., *Retaining Precision at Low-dose and High-speed STEM Imaging Conditions*, M&M 2020, Microscopy and Microanalysis Virtual Meeting, Online, August 4-7 (2020).

Mullarkey, T., Downing, C., Jones, L., *Digital HAADF STEM Imaging by Counting Electrons*, Microscopy Society of Ireland Symposium 2020, Trinity College Dublin, Ireland, January 8-10 (2020).

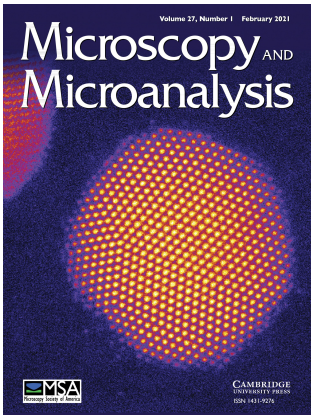

Cover image of Microscopy and Microanalysis, Volume 27 Issue 1, awarded to [1].

Chapter 1.

Introduction

1.1. From the Ground Up

Many texts in fields of nanotechnology begin with reference to Richard Feynman's famous talk *"There's Plenty of Room at the Bottom"* [2]. This talk, delivered in December 1959 to the American Physical Society espouses the supposed benefits of approaching many fields of science from the ground up; by controlling and manipulating things on a small scale. Whether the topic is machines built atom-by-atom or performing chemical syntheses by physical manipulation, it comes as no surprise that the electron microscope plays a large part in inspiring the musings of this work. Feynman even suggests that with more powerful electron microscopes that *"It is very easy to answer many of these fundamental biological questions; you just look at the thing!"* While perhaps not as straightforward as Feynman hoped, the electron microscope has been instrumental in key discoveries underpinning much of modern technology and has achieved feats such as atom-by-atom structural analysis and ferroelectric property mapping on the scale of unit cells [3, 4, 5].

For many decades, instrument performance was the limiting factor in electron microscopy imaging, however with recent advances such as aberration correction it is more likely than ever that *damage* to the sample caused by the instrument may now limit progress. While there is still much research to be done in improving fundamental hardware, improving the ability of current microscopes to capture data of suitable quality without damaging our samples is more important than ever.

The work presented in this thesis introduces why sample damage is a limiting factor, how it can be reduced, what issues arise when trying to reduce it, and my solutions to these issues. But before answering these questions, we first begin with an introduction to microscopy, beginning with light, not electrons.

1.2. Microscopy - From Light to Electrons

The scanning transmission electron microscope (STEM) is a versatile and powerful instrument capable of producing images of a wide range of materials with resolutions better than 1Å. This can be achieved through an intricate arrangement of an electron gun, apertures, scan coils, and detectors, just to name a few components, with a typical layout shown in **Figure 1.1**.

Each component has a storied history which alone could readily fill a thesis, so this section will largely focus on the history of the detector. Before arriving at that discussion however, we first turn to the transmission electron microscope (TEM), where the history of the STEM begins.

Although it is now known that image formation in a TEM is quite different to that of an optical microscope, originally in the 1930s, research into the TEM was based on the principles of light microscopy [6]. The driving force behind the developments

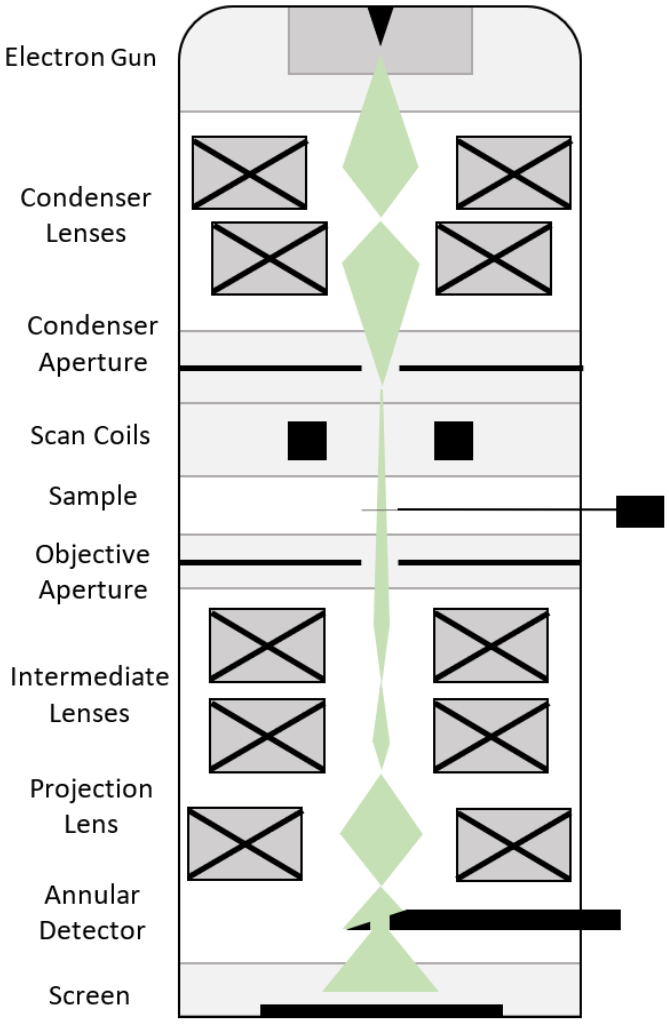

Figure 1.1.: Schematic of a typical (S)TEM, capable of both conventional TEM and STEM. Electrons emitted from the gun are first demagnified by the condenser lens, where a condenser aperture can be used to alter the size of the beam. Scan coils raster this finely focused beam across the sample, with transmitted electrons continuing down the column. In the case of STEM, these electrons hit a detector, while in TEM mode the electrons are instead focused onto the viewing screen or camera.

of the TEM was the ultimate resolution-limit of a microscope: the diffraction limit. This is demonstrated simply by the Rayleigh criterion, which states that the angular resolution, θ, of a *diffraction-limited* microscope with a circular aperture of diameter D, using illuminating radiation of wavelength λ is [7].

$$\theta \approx 1.22\lambda/D. \tag{1.1}$$

Visible light encompasses a range of wavelengths of the order of hundreds of nanometres, giving a resolution limit of ∼200 nm in the lateral dimension for a standard optical microscope [8]. However, techniques which go beyond this barrier have been developed, with the Nobel Prize in Chemistry in 2014 being awarded "*for the development of super-resolved fluorescence microscopy*" [9]. The resolution achieved with an optical microscope plateaued in the early 1900s, but at the same time de Broglie's formulation of the wave nature of electrons indicated a path forwards [10].

Electrons accelerated through a large potential difference (hundreds of kV) can reach wavelengths in the range of picometres. If used as a source of illuminating radiation, the resolution limit of such a microscope would be far lower than that of an optical microscope. Combined with the theoretical prediction that a cylindrical magnetic lens could be used to focus electrons, development of the TEM began in earnest [11].

While electron microscopes at the time, and still today, are very far from the diffraction limit, this massive reduction in wavelength lead to jumps forward in the highest imaging resolutions achieved, such as Max Knoll and Ernst Ruska's first TEM [12]. Before diving into the history, it is instructive to first cover basic imaging

theory to allow greater understanding of the developments which will be discussed.

1.3. Electron Microscopy Imaging Theory

In perhaps the simplest terms, a STEM forms an image by scanning a finely focused electron beam across a region of a sample pixel by pixel, spending a fixed amount of time, the dwell-time, at each one. During this dwell time a detector captures signals of interest produced by the interaction of the electron beam and the sample, and an image is created pixel by pixel. Each pixel's value, and therefore brightness, corresponds to the output of the detector during its dwell time.

Conventionally, the path the electron beam follows is to first scan an image line in the fast scan direction (left to right), and then move in the slow scan direction (top to bottom) by one pixel while also returning to the first pixel of the next image line. This latter motion occurs during what is referred to as the line flyback time. After the beam has reached the final pixel of the image (the bottom right) it then jumps to the top left during the frame flyback time, with this illustrated in **Figure 1.2**.

By using appropriately designed and placed detectors, we can detect only electrons which underwent certain interactions with the sample. By knowing which material properties causes these interactions, we can then relate image intensities to these properties. For example, if an electron in the beam passes very close to a nucleus in the sample, the strong attraction between the negatively charged electron and positively charged protons may cause the electron to deflect widely from its straight path.

For a sample of fixed thickness, the more protons in the sample's nuclei, i.e.,

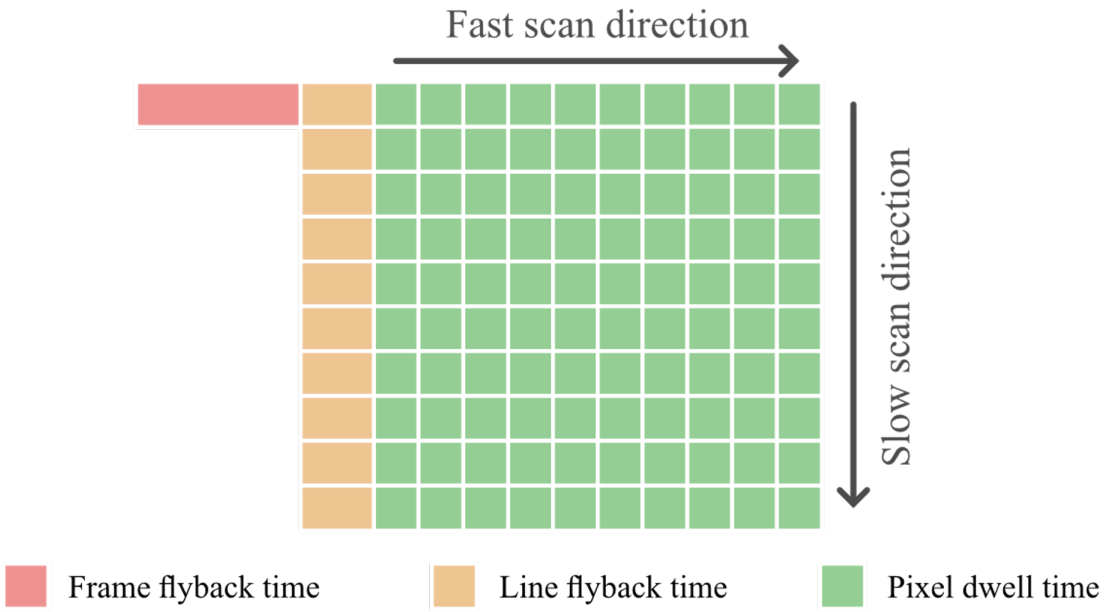

Figure 1.2.: Overview of the time spent during a conventional scanning transmission electron microscope image. In this image, the beam first moves from left to right before quickly moving down a line and back to the left during the line flyback time. At the final pixel (bottom right), the beam returns to the first pixel during the frame flyback time. Image adapted with permission from [13].

the greater its atomic mass number, the more electrons which will be deflected to high angles. If a detector is used which collects these highly scattered electrons, then image pixels will be brighter when the beam is positioned where the sample contains heavier nuclei, as more electrons will be being scattered. This *imaging mode* is referred to as high-angle annular dark-field (HAADF) imaging, and will be introduced in more detail later.

In this way, by designing different imaging modes sensitive to different sample properties, electron microscopy can be used not just to take pictures of materials, but to learn various properties of the sample. Although STEM imaging is the focus of this thesis, it is instructive to begin understanding its history by first discussing

the TEM.

1.4. History of Electron Microscopy

Although fundamentally different, TEM imaging can be broadly understood with analogues to optical microscopy. An illumination source (light or electrons) is focused and modified using lenses and apertures onto the sample to be imaged. Through interactions with the sample (absorption or scattering), the illuminating radiation is modified and is again focused, now onto an imaging plane (eyepiece or camera film).

Manufacturing the TEM was of course far more complex, requiring high vacuum conditions, samples thin enough to be transparent to electrons, and the design and construction of electromagnetic lenses. Despite these complexities, the potential of the instrument was well appreciated in its early days, and research into the underpinning physics was keen, with many interesting retellings of the history found in [14, 15].

Parallel to this research was the development of scanning electron microscopes (SEMs), where instead of a broad beam of electrons being used to image the whole field-of-view simultaneously, a finely focused electron-beam is used. This beam is scanned point-by-point in a raster fashion, collecting signals of interest at each, and in turn building an image point-by-point. The concept of using a scanning system to form an image was not new, with the fax machine patented nearly one hundred years earlier in 1843, and concurrent research was being performed on electron-beam scanning devices for use with televisions [16, 17].

Indeed, Max Knoll was working on this research, and so perhaps it is not surprising

that the first images obtained via a scanned electron-beam were published by Knoll in 1935 [18]. The SEM used to do so was fundamentally quite similar to today's instruments, which demonstrated that magnification could be changed by scanning a smaller sample area while keeping the display size fixed. This same understanding was reached by Zworykin, an early pioneer in scanning image systems [19, 20].

With both TEM and SEM now developed, Manfred von Ardenne then combined their underpinning ideas to produce the first STEM [21]. There was ample motivation for this invention, such as the desire to image thicker samples, and the knowledge that the lack of post sample lenses meant less aberrations, and greater flexibility in the choice of detectors used [22].

In a prolific writing period, von Ardenne produced multiple works on the performance and design of probe-forming electron optics using magnetics lenses. Numerous topics were covered, such as calculating the electron-beam current, the effects of lens aberrations of probe size, how dark-field (DF) and bright-field (BF) STEM detectors should be positioned, and even the effects of amplifier noise on image quality [20, 23, 24, 25, 26, 27].

Despite this great understanding, the technology available at the time unfortunately held back progress. High-resolution STEM imaging requires a small electron-probe, and without an effective electron source, producing a suitably small probe meant very low beam-currents were available, and in turn, signal levels.

While this could, in theory, be combatted through longer exposure times, there were no suitable low-noise detectors available, and so high-resolution STEM imaging was effectively impossible. While it was still possible to use larger probe sizes and obtain lower magnification images, this offered no advantages over using the more well established TEM techniques of the time. Due to this, and the destruction of

von Ardenne's STEM equipment in a World War II air raid, development of the STEM paused for many years until the 1960s.

Research into the STEM began again with Albert Crewe, part inspired through realisation of the aforementioned key issue: getting large enough beam currents into small enough electron probes [28, 29]. Crewe reached this realisation after studying the available probe forming lenses used in SEMs of the time [30, 31], and had the idea of using field emission from a small tungsten tip as an electron source to reach great enough beam currents [32]. Using these advances, Crewe constructed a STEM capable of imaging single atoms of molecules stained with uranium and thorium supported on a carbon film, the first observation of single atoms using an electron microscope [33, 34]. Some of these advances are shown in **Figure 1.3**.

Both an annular detector and axial electron spectrometer were used to form these images. An annular shaped detector positioned to collect electrons scattered outside the principal electron beam collected a large fraction of elastically scattered electrons. This had strong Z (atomic number) contrast, as the elastic scattering cross section has an approximately $Z^{3/2}$ dependence.

Simultaneously the axial spectrometer detected the majority of the inelastic scattering, which produced a signal proportional to the sample's thickness, and having only a weak, $Z^{1/2}$, dependence. The ratio of these images was taken, which suppressed image contrast due to thickness variations in the carbon background while retaining the visibility of the heavy atoms in the ADF signal. As the ratio of two images with $Z^{3/2}$ and $Z^{1/2}$ dependences was taken, this imaging mode was intuitively referred to as Z-contrast imaging.

It was believed that images formed using the ADF detector were incoherent, meaning that interference effects between electrons did not lead to contrast changes

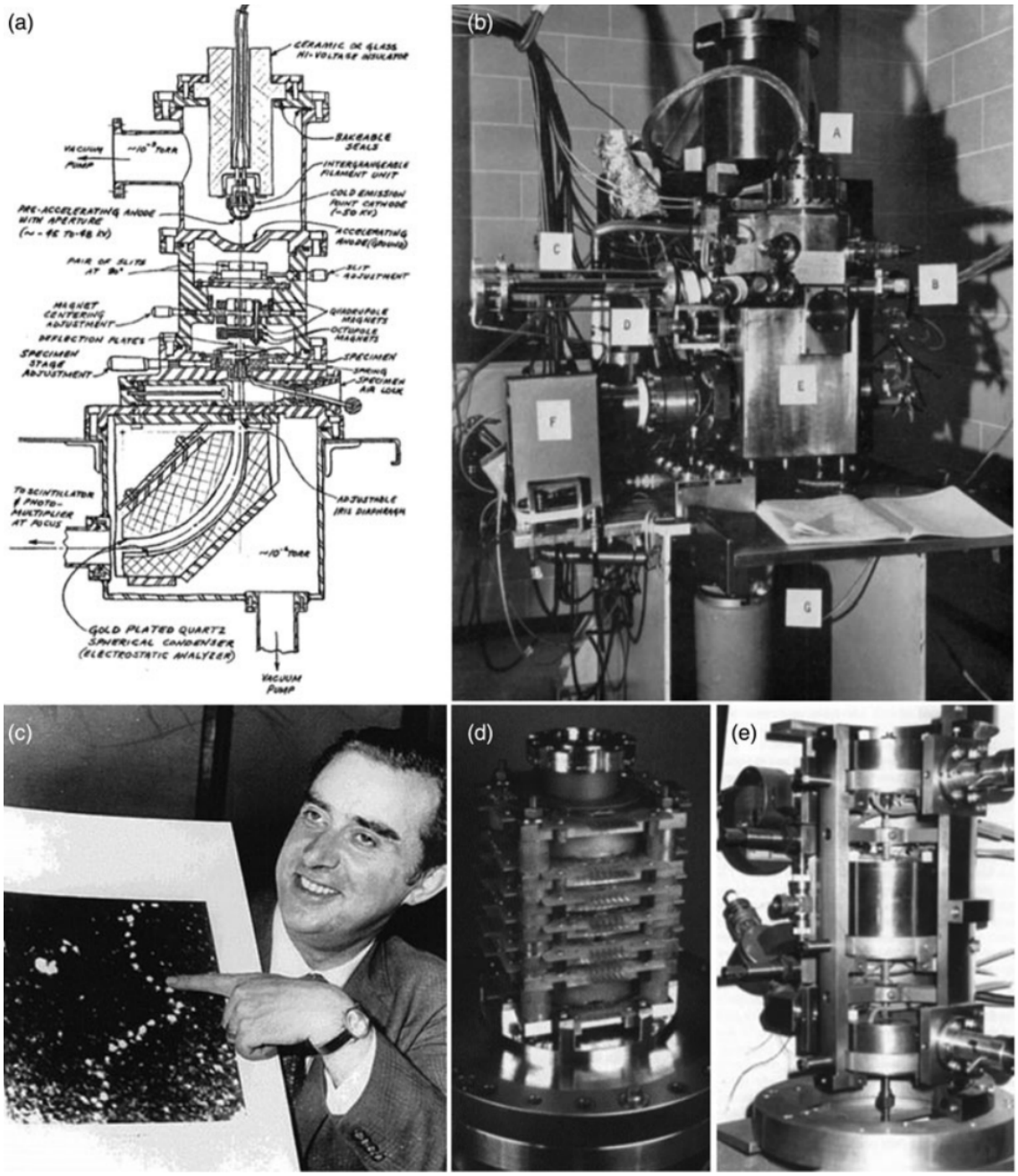

Figure 1.3.: Compilation of some of Albert Crewe's designs, innovations, and results. **(a)**, Albert Crewe's first STEM design. **(b)**, an early STEM capable of 0.5 nm resolution. **(c)**, a chain of thorium atoms imaged in 1970. **(d)** and **(e)** are images of early quadrupole-octupole and sextupole correctors respectively. Image from [20], published under a CC BY 4.0 License (https://creativecommons.org/licenses/by/4.0/).

in the image. When using a coherent imaging mode, contrast which may appear to arise due to sample thickness variations for example, may actually be caused by diffraction effects. This meant that the apparent coherent nature of ADF imaging was very useful for image interpretability, and controversial papers by Engel and Missell spread this idea [35, 36]. However, it did not take long to show that while this assumption was reasonable for separate scatterers, such as single heavy atoms, it did not hold in other scenarios, such as when imaging a crystal [37].

As high-energy electrons readily diffract from crystals, this results in distinct peaks in scattered intensity at certain angles, and not a smooth, incoherent distribution as required to exclude interference effects. While the goal was still to find an incoherent STEM imaging mode, ADF detectors still found wide use in imaging biological samples, as their lack of crystallinity meant that diffraction contrast did not occur and images were directly interpretable.

ADF detectors then began to have quite small inner angles to maximise their collection efficiency, increasing signal-to-noise ratios (SNR) [38]. While this was the path ADF followed, in turns out that the solution to creating incoherent images in the STEM was to do the opposite; increase the inner angle to create the high-angle annular dark field (HAADF) detector.

The first proposal for a HAADF detector was in 1973 by Humphreys, as electrons which scattered to these higher angles would do so via Rutherford scattering with protons in the sample's nuclei, having a Z^2 dependence as opposed to the $Z^{3/2}$ dependence of elastically scattered electrons [39]. Similar suggestions were made by Crewe and Treacy, noting that the higher Z dependence would improve the visibility of heavier atoms, while also being less sensitive to the crystalline nature of the sample [40, 41].

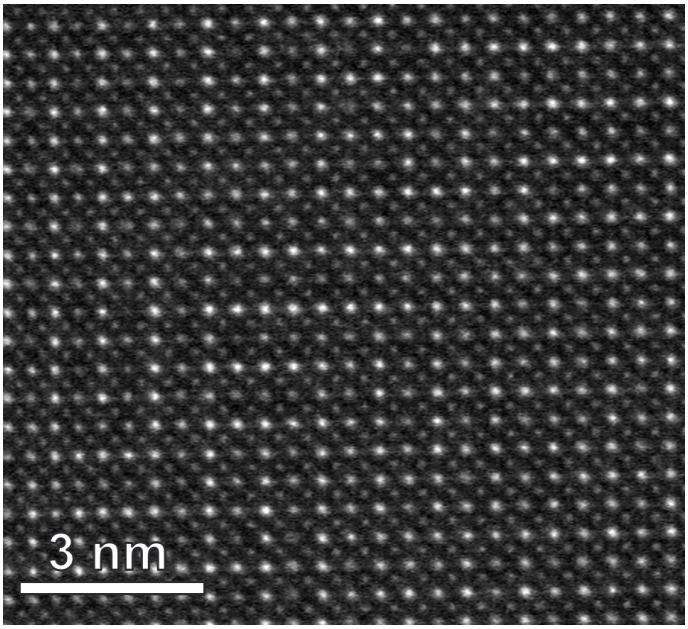

Figure 1.4.: HAADF image of lithium lanthanum titanium oxide (LLTO). LLTO has atomic columns containing varying concentrations of lanthanum. Due to lanthanum's large atomic number (Z = 57), columns containing higher concentrations of lanthanum appear brighter.

While the underlying detector technology will be covered in a different section, the first HAADF STEM images reported were by Treacy in 1980, displaying increased contrast of platinum particles on an aluminium background when compared to BF, ADF, and Z-contrast images of the same [42]. This increase in contrast allowed for easier finding of such small particles for use in conjunction with other techniques, such as electron energy loss spectroscopy (EELS), and as HAADF images were incoherent they could be used for quantitative studies, such as calculating dopant concentrations [43, 44]. An example of a modern, atomic-resolution HAADF STEM image is shown in **Figure 1.4**.

The increased contrast can be understood intuitively through consideration of the geometry of the detector. The only electrons which scatter to a great enough angle

to reach the HAADF detector do so by passing very close to the nuclei of atoms in the sample. These electrons see the unscreened charge of the nuclei, and so the strength of their interaction is proportional to Z^2, as can be seen by considering the force, F, due to the Coulomb interaction

$$F \propto q_1 q_2 / r^2, \tag{1.2}$$

where q_1 and q_2 are the charges of two interacting particles, and r the distance between them.

Understanding why this signal is incoherent however, is less obvious. While diffraction effects cause electrons to scatter coherently in a fixed direction, it can be shown that additional scattering effects from crystal vibrations (phonons), referred to as thermal diffuse scattering (TDS), effectively "blur" this scattering angle [45]. This acts like a diffuse broadening of scattered wave vectors dependant on the range of phonon momenta present in the crystal, reducing coherence.

However, it was shown that this alone is not enough to fully break coherence, and that we must also consider the physical size of the detector [46]. Although the maths is not reproduced here, it is shown that 1s-type Bloch states impart the most transverse momentum to electrons and therefore contribute most to image contrast when using a detector with a large inner angle. Coupled with the fact that these Bloch states are highly localised and depend very weakly on neighbouring atomic columns, scattered electrons reaching the HAADF detector act quite similarly to those scattering from single atoms and are not coherent [45].

It was previously said the electron microscopes are still not at the diffraction limit. One reason for this is aberrations in the lenses, where an aberration is any devia-

tion of a lens from ideal behaviours. Examples being electrons of different energies being brought to focus at different points (chromatic aberration), or electrons at different distances from the optical axis being focused to different points (spherical aberration), with both shown in **Figure 1.5**.

Correcting such aberrations is a key step in increasing the performance of an electron microscope. However, while glass lenses can be manufactured to any specification with advanced enough fabrication methods, the magnetic fields used to shape electron beams cannot be arbitrarily chosen due to physical laws such as Gauss's Law for Magnetism. Though it was known that aberrations were inherent to electron microscopes from as early as 1936, this did not mean that they could not be partially corrected, improving signal-to-noise ratio (SNR) and image resolution [47, 48, 49]. Despite this advanced theoretical knowledge, attempts to increase resolution using the required quadrupole/octupole correctors and sextupole correctors were long unsuccessful, largely limited by the technology of the time [50].

Towards the turn of the century, successful implementations of aberration correction were finally seen, first by Zach and Haider in the SEM, and afterwards by Haider et al. in the TEM, based on Rose's 1990 work [51, 52, 53]. Contemporaneously, Krivanek et al. constructed a dedicated STEM with computer-controlled aberration correction using a quadrupole/octupole corrector [54, 55].

Despite the undue brevity of these paragraphs, the effects of aberration correction on advancing electron microscopy perhaps cannot be understated, with an excellent review written by Pennycook in 2017 [56]. Indeed, the 2020 Kavli Prize in nanoscience was awarded to Harald Rose, Maximilan Haider, Knut Urban, and Ondrej Krivanek for their research into, and creation of, aberration correctors for electron microscopes [57]. Contemporaneous with the development of the STEM

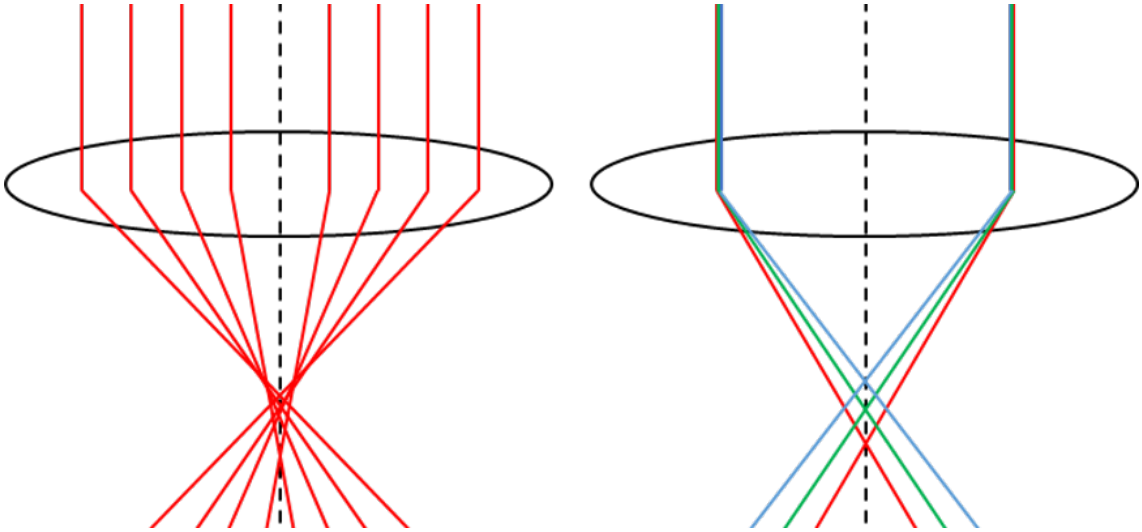

Figure 1.5.: The effect of aberrations on an optical system. **Left**: Light rays at differing distances from the optical axis (the dashed black line) are focused at different points due to spherical aberration. **Right**: Chromatic aberration causes light rays of different energies, represented here by colours, to be brought to focus at different points.

was also development of the detectors used in the STEM, with this covered in the following section.

1.5. Evolution of Detector Technology

The first electron microscopes used a widely available technique at the time to record their images: photographic film. Although this may seem rudimentary to those unfamiliar, this was a mainstay of TEM for many decades and had many strengths. With suitably fine-grained film, good resolution can be achieved as detection efficiency is quite large, and due to its large dynamic range, images with very high information content could be captured [58].

However, despite these strengths, film had downsides both as an image capturing

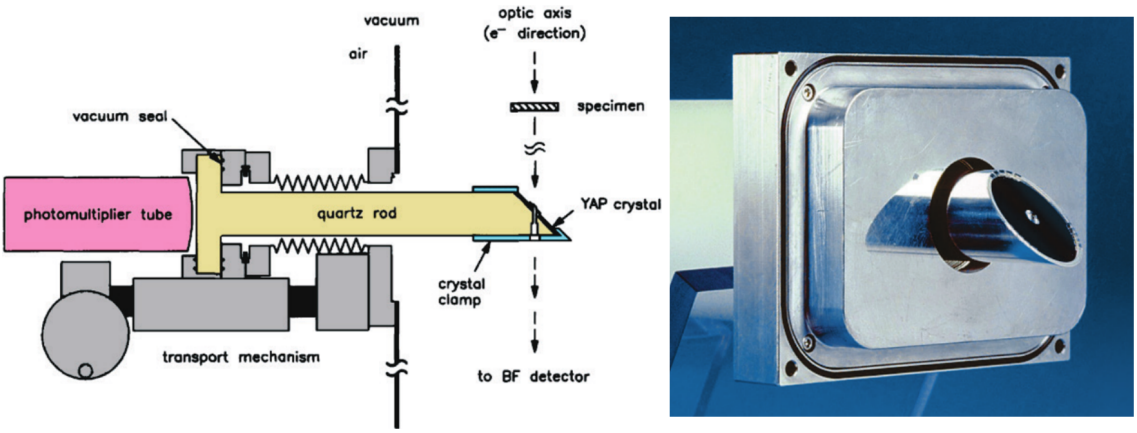

Figure 1.6.: Left: Diagram of a typical HAADF STEM detector. **Right**: Photograph of a Fischione ADF 3000 detector. Image adapted from [60], published under a CC BY 3.0 license (https://creativecommons.org/licenses/by/3.0/).

medium, and on practical levels. Film is not completely linear in converting electron beam intensities to optical intensities, and the intrinsic fog level present in unexposed film causes noise, particularly in low-dose images. Also, the number of images which could be captured in a single session was limited by the space available for photographic plates (approximately 30-50), and the process of capturing a single image took several seconds, limiting temporal resolution [58, 59].

Not only was temporal resolution limited in an experimental sense, but the images could not be viewed until the film was removed from the microscope and processed, so no feedback was provided to the microscope user. Furthermore, to produce the Fourier transform of an image, the use of an optical bench, lenses, and exposure of new film was required. While electronic cameras provided immediate feedback and greater temporal resolution, initially their performance was quite poor compared to film [59].

As previously stated, early STEMs could not simultaneously get high beam currents while using fine probes, and the resulting low signal level meant the intrinsic

noise in film dominated images. An alternate approach was required, and this was to develop electronic detectors. The first HAADF detector was intended to be a solid-state detector, but this was regrettably damaged upon fabrication and instead the combination of a scintillator and recently constructed cathodoluminescence detector was used [61, 62, 63]. This design evolved into a design still readily seen today which uses a more efficient scintillator and photomultiplier tube (PMT) combination, as shown in **Figure 1.6** [64]. Initial designs were similar to other detectors of the time, such as the Everhart-Thornley detector used in SEMs, and many related detectors used in radiation detection [65, 66].

This style of detector functions by the scintillator first converting electrons to photons, which are guided along a quartz light-pipe before being converted back to electrons via the photoelectric effect at the PMT. This quartz rod couples the scintillator, which is inside the vacuum of the STEM, to the PMT, which is not.

Next, a series of increasingly positive charged anodes, called dynodes, attract these photoelectrons causing them to collide with the dynode, successively producing more electrons each impact. This multi-stage increase in the number of electrons means that a single electron impact at the detector can result in millions of electrons in the PMT, resulting in a readily detectable signal [67].

Plastic was used as a scintillator in nuclear physics experiments, however the much higher doses used in electron microscopy meant that this was not a suitable choice as it damaged to perhaps 10 % of its initial efficiency within a matter of days or weeks [64]. A single crystal of yttrium aluminium garnet (YAG) was suggested due to its high tolerance to damage and high detective quantum efficiency (DQE), however the wavelength of light it emits (550 nm) did not match the maximum sensitivity of a typical PMT near 400 nm [68].

The solution then was to use single crystal yttrium aluminium perovskite (YAP), which had the same positive properties of YAG, but emitted light at a more suitable wavelength (370 nm), had a higher radiation efficiency (7% vs. 4%), and a shorter decay time (30 ns vs. 70 ns) [68].

Although some development continued on scintillator-based detectors, such as combining P47 scintillating powder with a single crystal scintillator, most have moved towards direct electron detection [69, 58]. These detectors are so named as the detected electrons do not undergo any intermediate detection stage, e.g., conversion to photons, and are instead converted directly to electrical signals.

A popular choice of direct electron detectors consist of an array of pixels which capture the full scattered, post-specimen, electron beam instead of just an angular range as with a HAADF detector. By later masking the captured data, an image can be formed as it would appear using only the unmasked pixels initially. This type of detector is often referred to as a 4D detector, and correspondingly the technique as 4D STEM, as a two-dimensional image of the full diffraction pattern is captured at each two-dimensional probe position [70].

While a very powerful technique, these 4D STEM detectors are costly, slow to capture images, produce enormous datasets, and require extensive onwards processing, although many members of the microscopy community have produced packages for processing such data, such as py4DSTEM [71]. Due to these limitations, this technique is not explored further in this thesis, however this is not intended to dismiss the exciting results this technique has already produced and promises to generate.

The previous sections have demonstrated that for decades, the development of (S)TEM was driven by a need to increase microscope performance. Yet now it has reached a stage where for many samples the instrument is in fact no longer the limit-

ing factor, and it is instead damage to the samples caused by these intense electron beams. Aberration correction for example, dramatically increased the number of electrons which could be focused into ever smaller probes. While research and development are still ongoing on improving microscopes, there is an ever-increasing interest in low-dose techniques in order to avoid this issue of sample damage.

1.6. The Necessity of Low-dose

As previously stated, the motivation for using high-energy electrons is that they have low wavelengths (after $E = hc/\lambda$), however, using high-energy electrons comes with downsides. The primary downside is the damage that these electrons cause to the sample being imaged. While some inorganic samples can readily withstand electron doses in the order of 10^8 $e^{-}Å^{-2}$, this if often many millions of times too great for other samples [72, 73].

While biological tissues are the most common example of samples which are readily damaged in an electron microscope, there are many examples of modern, technologically important materials which also easily damage, such as zeolites, low-dimensional materials, covalent-organic frameworks, polymers, and metal-organic frameworks [74]. Before discussing dose further, it is important to define it, as the terminology is not fixed in the electron microscopy community:

$$Dose = \frac{I \cdot C \cdot \delta_{\mathrm{t}}}{dx^2} \cdot F, \tag{1.3}$$

where I is the electron beam current used, C is Coulomb's number, δ_t is the dwell-time, dx^2 is the area of the pixels, and F is the fraction of pixels illuminated if using

a method such as compressed sensing.

It is common to see this definition referred to as the electron fluence, while the word dose is used to refer to the fluence *times* the charge of the electron, with typical units of C/cm^2 [75]. Following from the definition used here, the dose-rate can also be defined, which is **Equation 1.3** divided by the duration of the sample's exposure, with units of $e^{-}Å^{-2}s^{-1}$.

The way in which electrons damage a sample can be categorised into primary, secondary, and tertiary mechanisms [76]. The two main primary damage mechanisms are knock-on damage and radiolysis. Knock-on damage is where an electron in the beam transfers enough energy to directly displace an atom from the sample, resulting in point defects. Radiolysis occurs when incident electrons interact with electrons in the sample, breaking chemical bonds, resulting in ionisation. While knock-on damage affects inorganic samples more, radiolysis is more damaging to organic materials. Raising the energy of the electron beam increases the chance of knock-on damage but decreases the likelihood of radiolysis events [77]. An example of primary damage is shown in **Figure 1.7**.

Secondary damage is caused by the propagation of the effects of primary damage. For example, secondary electrons or phonons may propagate, causing further scattering or sample heating, and therefore damage [76]. The majority of organic and biological specimens are not good thermal conductors, and the amount of heating can be considerable, damaging, if not melting, the sample. When considering heating, not only is the dose important, but so too is the dose-rate. At low enough dose-rates some samples may have time to dissipate their heat, preventing damage, with simulations suggesting proteins imaged at liquid nitrogen temperature may not be badly affected by heating if the dose-rate is kept below 50 $e^{-}Å^{-2}s^{-1}$. [78].

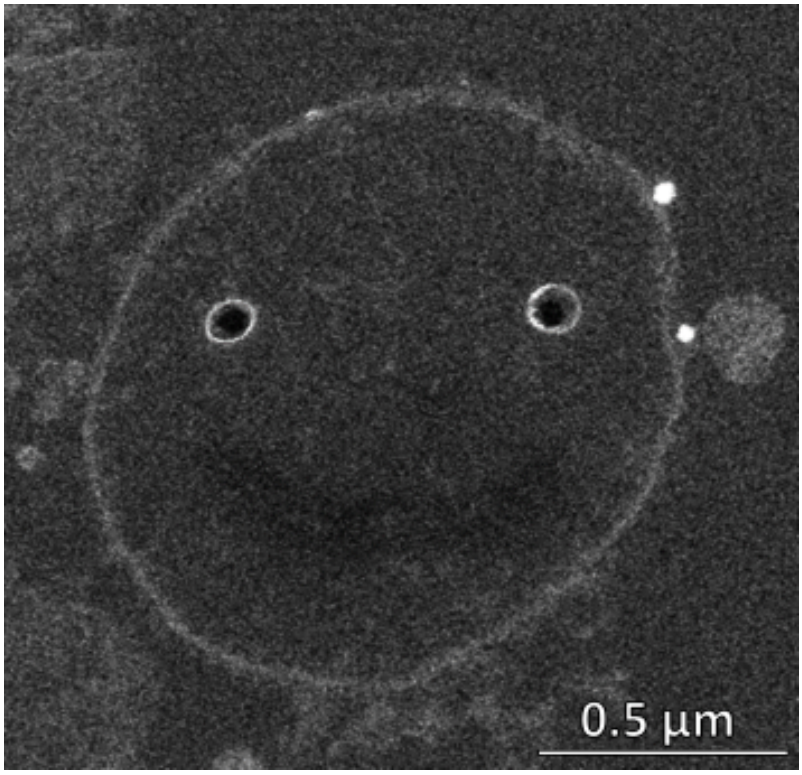

Figure 1.7.: Image of biological tissue where two holes have been intentionally burned into the sample, an example of primary beam damage.

Tertiary damage occurs when gasses, generally hydrogen and oxygen, are released from the sample when bonds break due to radiolysis, and then build up within the sample. For example, hydrogen bonding is common in biological systems, and when hydrogen atoms are released due to radiolysis they are trapped due to the sample being frozen (to increase its resistance to beam-damage). Gas bubbles then begin to form, damaging the sample as they continue to grow [79]. With these mechanisms so readily able to remove the ability to capture useful data, it is no wonder that many low-dose techniques have been investigated, which will be briefly touched upon now.

As has already been implied, understanding these damage mechanisms, such as the sample types they are more likely to occur in and under what conditions, is the

first step in minimising their effects. Appropriate experiment design, such as a TEM user reducing the incident beam current, beam diameter, or changing the incident energy, is an essential part of lessening the effects of beam damage [80].

Also hinted at is cooling / freezing the sample to increase its resistance to damage, with this family of techniques often referred to as cryo-electron microscopy (CryoEM), a technique which was awarded the 2017 Nobel Prize in Chemistry [81]. The benefits to this are numerous, one is that vitrification of the aqueous medium of a cell, for example, locks the molecular contents in place without adding or removing any material, which is advantageous for morphological or compositional studies [82]. While cooling also provides some resistance to the heating effects of the electron beam, this is not a dramatic effect, and is not the main benefit to the majority of samples [80].

CryoEM is generally performed using either liquid nitrogen (at temperatures of approximately 77 K) or liquid helium at 4 K, with studies on protein crystals of bacteriorhodopsin showing a near ten times increase in its damage resistance upon cooling from room temperature to liquid nitrogen temperatures [83]. This was measured by calculating the critical dose (the dose required for the intensity of diffraction spots to reduce to 1/e of their original intensity) at these two temperatures. The strong dependence of damage on temperature is likely largely caused by diffusion's dependence on temperature [84]. As diffusion occurs far more slowly at low temperatures, secondary damage mechanisms which are caused by the propagation of primary damage effects also occur far more slowly, resulting in less damage.

A STEM specific approach to reducing beam damage is the change the pattern in which the electron beam is scanned. This may mean changing the path the beam follows to reduce or eliminate line or frame-flyback times (**Figure 1.2**), or

even skipping certain pixels, later recovering the skipped information. Both of these approaches have challenges and difficulties, namely that the majority of microscopes do not come with the ability to generate custom scan patterns, or blank the beam where necessary, but offer potentially exciting results.

Using the necessary hardware, many scan patterns have been investigated such as snake/serpentine scanning, using Hilbert space-filling curves, or variations of spiral scanning such as Archimedean, Fermat, and constant linear velocity scans [85, 86]. Serpentine and Hilbert scan patterns have the advantage of eliminating line-flyback time, reducing both the electron-dose and increasing scan speed, while spiral scanning reported similar outcomes. However, a trade-off is made between non-uniform distortions introduced into the image and uniform sampling density, and therefore dose density.

Sampling less than the full number of pixels corresponds to changing the value for F in **Equation 1.3**, with sampling only 50 % of the pixels in an image promising an immediate reduction in the electron-dose by half. While this of course reduces the amount of information captured by the same amount, we can assume that images are not completely random and contain some structure and that this structure can be recovered, with this family of techniques often referred to as compressed sensing or sparse sampling [87].

Such techniques have demonstrated impressive results for a range of sample types and interpolation techniques, however, when applied to data with only Poisson noise present compressed sensing has been shown to not increase the amount of information present [88, 89, 90, 91]. Not only are techniques to reduce the electron-dose important, but so too are those which maximise the information return for the dose which is used. One common way of doing so is multiframe imaging.

1.7. Multiframe Imaging

With the concept of a critical-dose having been introduced, it is constructive to think about how one can spend their *dose-budget*. For example, it is possible to capture a single image using a pixel dwell-time of 40 μs, two images with a 20 μs dwell-time (later summing them), ten images with a 4 μs dwell-time, and so on. Ignoring for now the effects of flyback time, these variations produce final images which have experienced the same electron-dose, however it has been shown that these final images are not equal.

While great lengths are taken to isolate the electron microscope from the effects of the environment it is in, many sources of external noise can affect images; electromagnetic fields, vibrations, changes in temperature, and air pressure fluctuations [92, 93]. The reason for mentioning this is that these sources of noise change with time, but the sample (ideally) does not. Therefore, splitting the electron-budget across multiple image frames means we produce images with a static sample but changing noise, allowing the possibility for separation of this noise from the underlying ground-truth: the sample. While for a single image, the noise and ground-truth information are not separable.

In practice, for both ADF imaging and spectrum imaging, it has been found that precision increases in both cases, while also reducing sample damage, as the electron dose-rate is reduced with faster scanning [94, 95]. In the case of ADF imaging, image series 20-30 frames in length are suggested, with a reduction of up to 70% of the scanning artefacts when compared to a single image. Little advantage is seen beyond this number of frames, perhaps as the signal level in each individual image is too low to align the dataset, with this topic covered next.

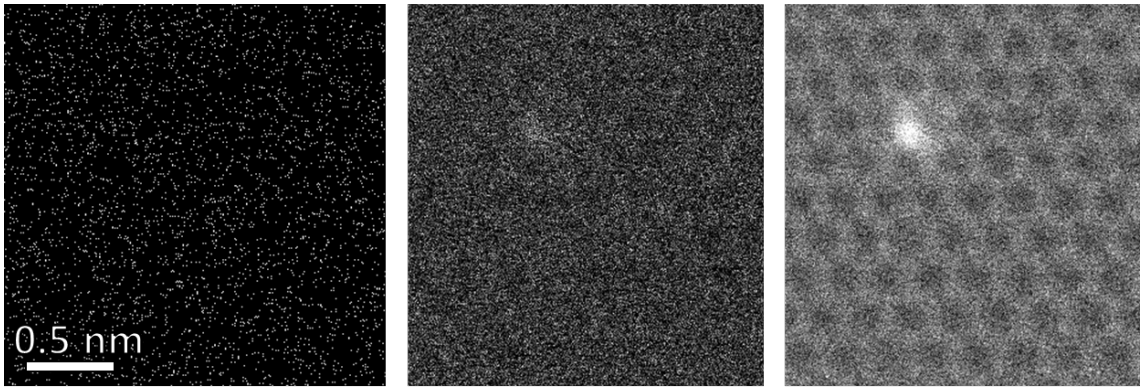

Figure 1.8.: One, four, and 20 image frames of a sample of graphene with a silicon dopant atom. The image frames have been rigidly aligned and averaged using the SmartAlign software. Each frame has a dwell time of 2 μs and a $\sim$5 pA beam current. In a single frame no structure can be discerned. Some structure is slightly apparent in the four stacked frames, as is the dopant atom. The structure of graphene and the single dopant atom are clearly visible after averaging 20 frames.

While it was stated that 20-30 frames may be ideal, this is contingent on being able to align each of these frames in the image series. Aligning is a key aspect of multiframe imaging, as it is very unlikely that the sample will remain stable throughout capture of the dataset. It is not unusual to have multiple pixels worth of sample-drift between consecutive image frames due to thermal expansion, for example. Many algorithms have been developed to identify and correct this drift, such as RevSTEM and SmartAlign, with an example of using the latter shown in **Figure 1.8** [67, 96, 97].

These software packages also include the ability to capture data with rotation of the scanning direction between frames, allowing for easier separation of the noise and ground-truth. While it may seem the necessity of aligning is a downside of multiframe imaging, these same sources of noise of course manifest in a single, long-exposure image also. If we imagine drift in a single direction, say aligned with a horizontal, fast-scanning direction, a slow speed image captured under these

conditions of a single crystal would appear to be skewed in the drift direction, completely distorting the crystallography. Further approaches to low-dose STEM imaging will be explored in this thesis.

1.8. Thesis Overview

Having covered the basic principles, theory, and history of the STEM, I hope it is clear why decades were spent increasing the intensity of the electron beam, and why now, unfortunately, these intense beams are often the limiting factor in imaging samples. Knowing that the direction to explore is developing low-dose imaging techniques, this thesis explores the avenues possible to do so, the problems which arise when doing so, and how they can be overcome.

In **Chapter 2** the topic of signal digitisation is introduced. This is important as it is shown the simplest, most widely available way to reduce electron dose is to decrease the dwell-time and the beam current. It is found that the combination of these approaches introduces a severe streaking artefact into the images produced, caused by the decay time of the scintillator and PMT combination used in most HAADF detectors. Images captured with this artefact have severely reduced resolution, and without a solution these imaging conditions are near unusable. By digitising the signal this streaking artefact is eliminated, along with other noise sources, and the most approachable way to produce low-dose images is again usable.

The quantitative improvements that the above approach makes are explored in **Chapter 3**. Two main approaches are used here, analysing the effect that digitisation has on both detector maps, and Fourier transforms. Detector maps are regularly used to quantify the performance of the detector being used, and by showing before

and after digitisation comparisons we can see the improvements that digitisation makes, or alternatively, the impact that signal streaking has. The Fourier transform, which will be explained fully later, is very regularly used to analyse images as it shows the spatial frequencies which are present in the image, and therefore can be used to show what resolution has been achieved. Through similar before and after comparisons we can see how resolution is degraded in the image, and how this is related to the imaging parameters and detector used.

Another low-dose technique employed in this thesis is reducing the line flyback time. While this time has the important role of allowing the electron beam to reach a steady velocity while scanning each line in the image, it produces no usable information while still damaging the sample, while also limiting the framerate achievable. While reducing the line flyback time will minimise these negative effects, it introduces distortions into the image as the electron beam is not travelling at a fixed speed, and is therefore not where we expect it to be at each pixel. This is due to hysteresis in the magnetic lenses controlling the electron beam's location, and by accounting for this we show how this distortion can be corrected for in, past, present, and future data in **Chapter 4**.

In **Chapter 5** ongoing and future work are described, referencing ongoing experiments and data analysis at the time of writing by myself and other colleagues, as well as near and far future plans.

Chapter 2.

Signal Digitisation by Electron Counting

In the previous chapter, the history of the STEM was detailed, and how impressive technical developments now mean that the instrument is often no longer the limiting factor for imaging many materials, but instead electron-beam induced sample damage. In this chapter, the focus is on a simple method to reduce the electron dose; reducing the beam current and dwell-time. However, as will be shown, this leads to an often severe signal-streaking artefact in the fast scanning direction, making these imaging conditions unusable for producing high-quality images.

To overcome this, new hardware is developed to digitise the signal from the detector, where a '1' corresponds to an electron impact, and the signal is '0' otherwise. This has the advantages of localising electron impacts to a single point in time, eliminating streaking, while also providing a quantitative count of the number of electrons scattered to the detector during each dwell-time. The development of the hardware used to achieve this and the results obtained are presented in this chapter.

2.1. Low Dose-rate Imaging

To explain why reducing the beam current and dwell-time is a very practical way to reduce the electron dose, it is instructive to re-introduce the dose-equation from the previous chapter:

$$Dose = \frac{I \cdot C \cdot \delta_{\mathrm{t}}}{dx^2} \cdot F, \qquad \text{(1.3 revisited)}$$

where I is the electron beam current used, C is Coulomb's number, δ_{t} is the dwell-time, dx^2 is the area of the pixels, and F is the fraction of pixels illuminated if using a method such as compressed sensing. Of the four variables in this equation, F can only be changed with specific hardware not available to all, and dx^2 is generally fixed by a feature size of interest in the sample, leaving only I and δ_{t} which can be varied. Hence, a 'universal' way to reduce the electron-dose regardless of the scanned instrument being used or sample being imaged, is to use a lower beam current and scan at faster speeds, decreasing both the dose and the dose-rate.

Should a certain SNR be required, multiframe imaging can be used to account for the lower dose, and therefore signal level, per image, with this already being a superior approach to STEM imaging. While a simple and accessible method to reduce the dose, it regrettably leads to signal streaking. The origin of this streaking artefact, and how it can be eliminated to allow these imaging conditions to be used, is explored in this chapter.

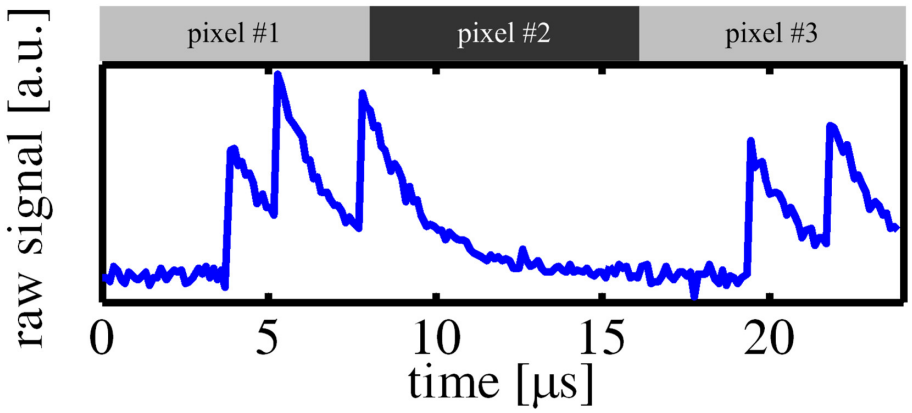

Figure 2.1.: A simulated, 24 μs readout from a detector where single electron impacts are visible. This model corresponds very closely to the example pulses measured in this thesis with an oscilloscope. Reprinted from [101], with permission from Elsevier.

2.1.1. The Single Electron Signal

Although it was previously stated the YAP crystal used in many detectors has a decay time of approximately 30 ns, this is the decay time of solely the crystal. When used in tandem with a PMT and associated readout electronics, the combined decay time can readily rise above 1 μs [68, 98, 99, 100, 1]. When imaging with typical beam currents, say in the nA range, a very large number of electrons hit the detector and the output appears continuous, with no obvious features in the signal due to any one electron's impact.

However, at lower doses, the number of electrons hitting the detector decreases, and at low enough doses the time between events is great enough that each electron produces a distinct peak in the detector's output. The duration of this pulse is related to the aforementioned decay time, ranging from tens of nanoseconds, to over one microsecond, depending on the detector. This effect has been previously studied, and an example of a model of the single electron signal is shown in **Figure**

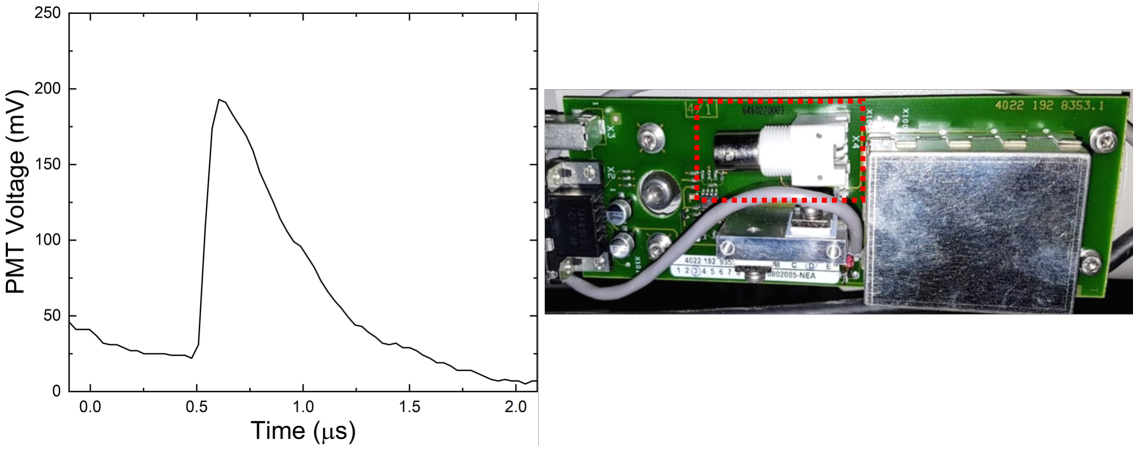

Figure 2.2.: Left: Experimentally captured pulse due to a single electron impact from a Fischione 3000 ADF detector. This data was obtained using an oscilloscope connected to the detector. **Right**: A BNC connection, in the dashed-red box, on the PMT of a detector where the oscilloscope can be connected to.

2.1.

In **Figure 2.2**, a single pulse is shown with a duration of approximately 1.5 μs. While the exact duration varies, the example shown is a typical one, with a measured decay time of approximately 0.4 μs. Although different pulse shapes will be shown later, the shape here can be described as a sharp rising edge followed by an exponential decay, which can be naturally understood through the electron-detector interaction. This exact pulse shape was used to simulate the output of this detector for decreasing electron beam currents to demonstrate how single pulses become visible at low currents, shown in the next figure.

In **Figure 2.3**, the simulated output of an ADF detector is shown as the beam current decreases, from approximately tens of nA, to less than ten pA. In the nA range, so many electrons are hitting the detector that the detector's output, the solid black line, does not show features due to any single electron's impact. Conversely, at low beam currents, the signal is largely separate electron pulses, although due to

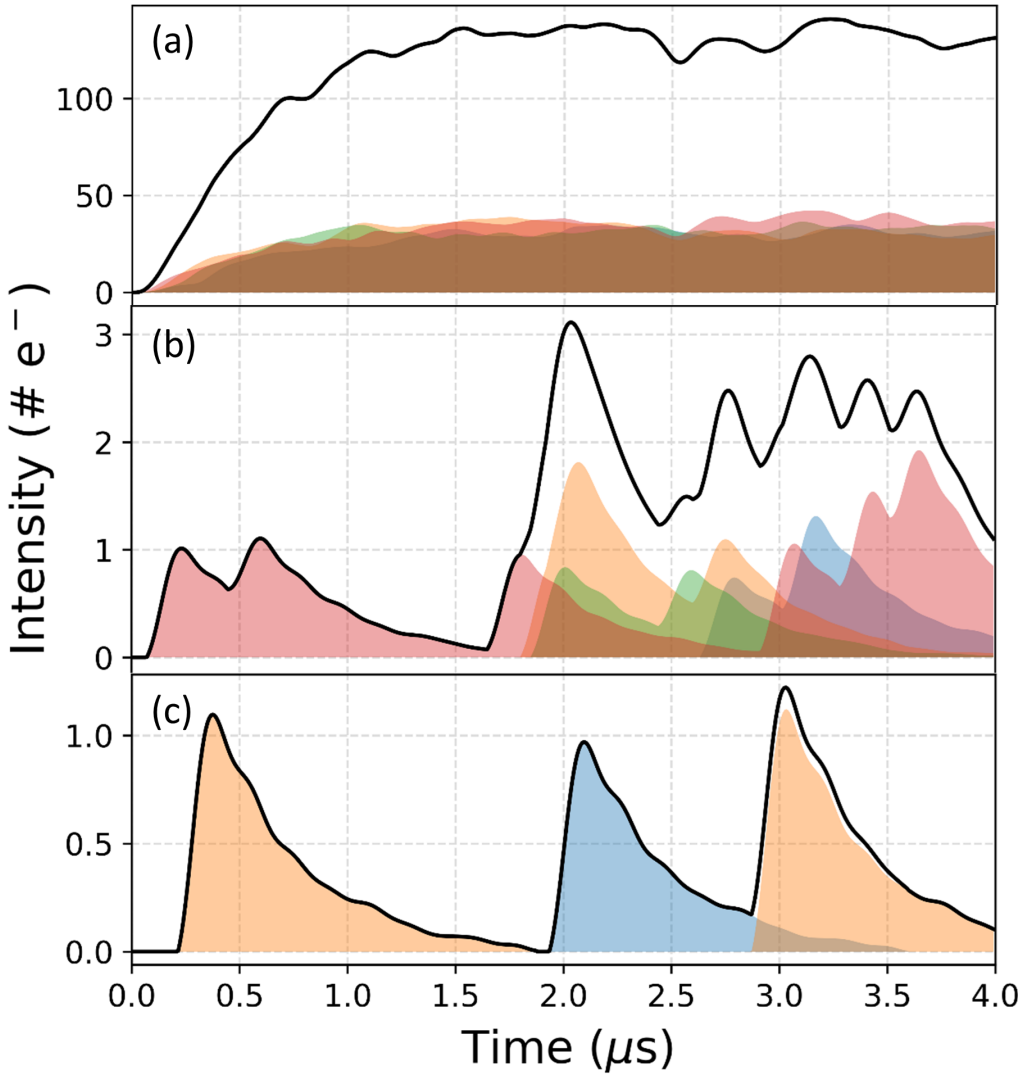

Figure 2.3.: Simulations of the output of a Fischione 3000 ADF detector for decreasing beam currents, using the pulse shape from **Figure 2.2**. The solid black line is the integrated detector output, while individual electron impacts are coloured to aid in interpretation. At high doses, **(a)**, no distinct peaks due to any single electron impact are visible in the output. At lower doses, **(b)**, some individual peaks are visible in the net output, but pile-up of signal means that some are not separated enough to be visible. At very low doses, **(c)**, the signal is dominated by single peaks, generally with little to no overlap between them.

the stochastic nature of electron scattering there is no guarantee that electrons will not overlap. When the signal is as sparse as in the low beam current data stream example, and low dwell times are used, we begin to see signal streaking.

2.2. Signal Streaking and Detector Afterglow

Signal streaking occurs when signal which *should* be localised to one pixel (the pixel during which the electron hits the detector), is instead present in subsequent pixels. While this would not happen if using a 'perfect' detector with no decay time, the finite decay time present on all detectors may cause the streaking of signal. This is demonstrated in **Figure 2.4**, where it can be seen that once the dwell-time is shorter than the decay time, streaking is unavoidable.

While streaking can still happen at longer dwell-times, the relative error is lower as there is more signal per pixel, and it is less likely to occur. The effect of signal streaking is also shown in this image, with signal clearly spreading across multiple subsequent pixels following where the electron impact occurred. The immediate effect of this is the loss of high-resolution features, as any feature only a few pixels in size will be obscured by this streaking effect. Furthermore, as this is a temporal effect, any feature a few pixels in size in an image, regardless of actual physical dimensions, will be affected in the same way.

While focus has been on the decay of the single electron signal, more than one decay time can be associated with a scintillating crystal. For example, although not always visible in images, a much slower decay is also present, becoming apparent when there is a region of vacuum neighbouring the sample. Although the origin of this response is unknown without specific information of the scintillator used, it may

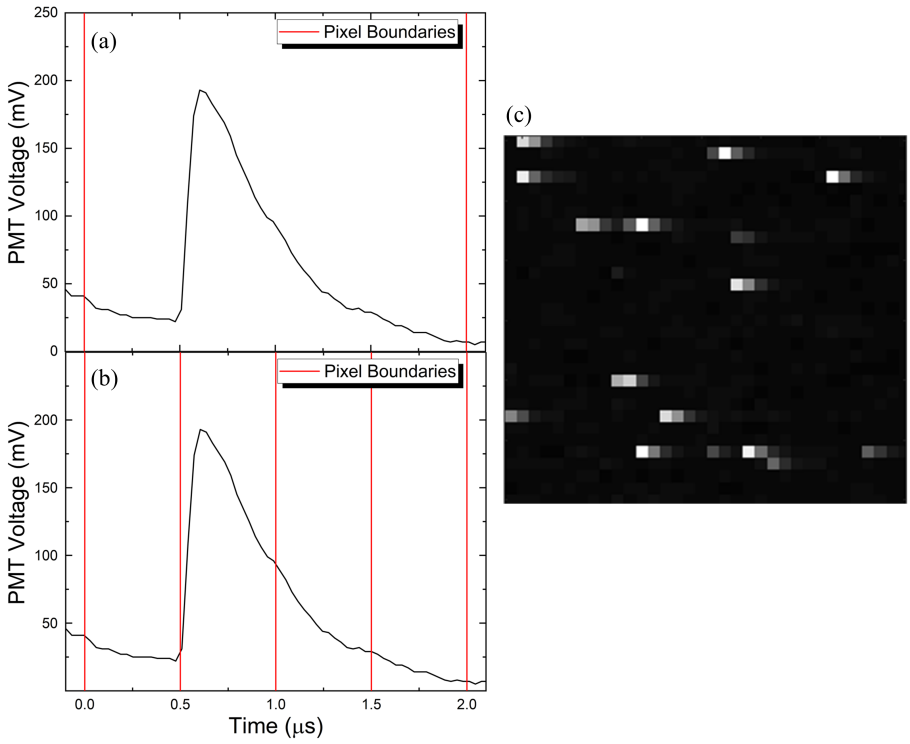

Figure 2.4.: A pulse caused by a single electron, with pixel boundaries in red for two different dwell times. This is 2 μs in **(a)** and 0.5 μs in **(b)**. While signal streaking may occur at any dwell time, it becomes increasingly common, and eventually unavoidable as in **(b)**, at shorter dwell times. **(c)** shows a magnified section of an image captured with a very low beam current and a dwell time of 0.5 μs, demonstrating the effect of signal streaking. Streaking is seen to persist across three to four pixels, aligning with the observed pulse duration shown. Part of this figure is adapted from [102].

be caused by the trapping and subsequent release of electrons and holes at emission centres due to defects [103].

Similarly to signal streaking, while this effect is always present, it is often not visible at higher doses. To demonstrate how the combination of streaking and afterglow can cause image degradation, a sample of silver nanowires was imaged as it contains sharp features at mutually perpendicular directions, meaning that aligning one feature with the slow scan direction will cause the other to be perfectly aligned

with the fast scan direction, as shown in **Figure 2.5**.

Due to signal streaking, it can be seen in this figure that when the nanowire is aligned with the fast scan direction it becomes difficult, if not impossible, to measure the width of the twin defect sites. When the scan direction is rotated, the defect sites become far easier to identify, however, the width of the nanowire is now obscured by both signal streaking and afterglow. What is needed then is a way to eliminate signal streaking and afterglow to allow these operating conditions to be used, and for that we turn to digitisation.

2.3. Signal Digitisation

While signal streaking is caused by the shape of the pulse, fortuitously, this same shape is exploitable to arrive at the solution. Despite the wide range of pulse intensities, even the smallest almost always produce a distinct peak above the background noise. As the pulse may be considered the convolution of an impulse response and a decaying edge, deconvolution seems an appealing route to separate these to remove the decaying edge, and therefore signal streaking. However, as the detector response is not linear with respect to incident electron energy, this precludes deconvolution as on option.

Another approach is to apply an intensity threshold to the datastream from the detector, attributing an electron impact to any time the signal crosses this threshold, creating a digital signal where each '1' is an electron impact. Although an implementation was partially successful, pulse pile-up, which can still occur at very low doses, made setting a single threshold value for both low intensity pulses and large, piled-up pulses impossible, as shown in **Figure 2.6, (a)**.

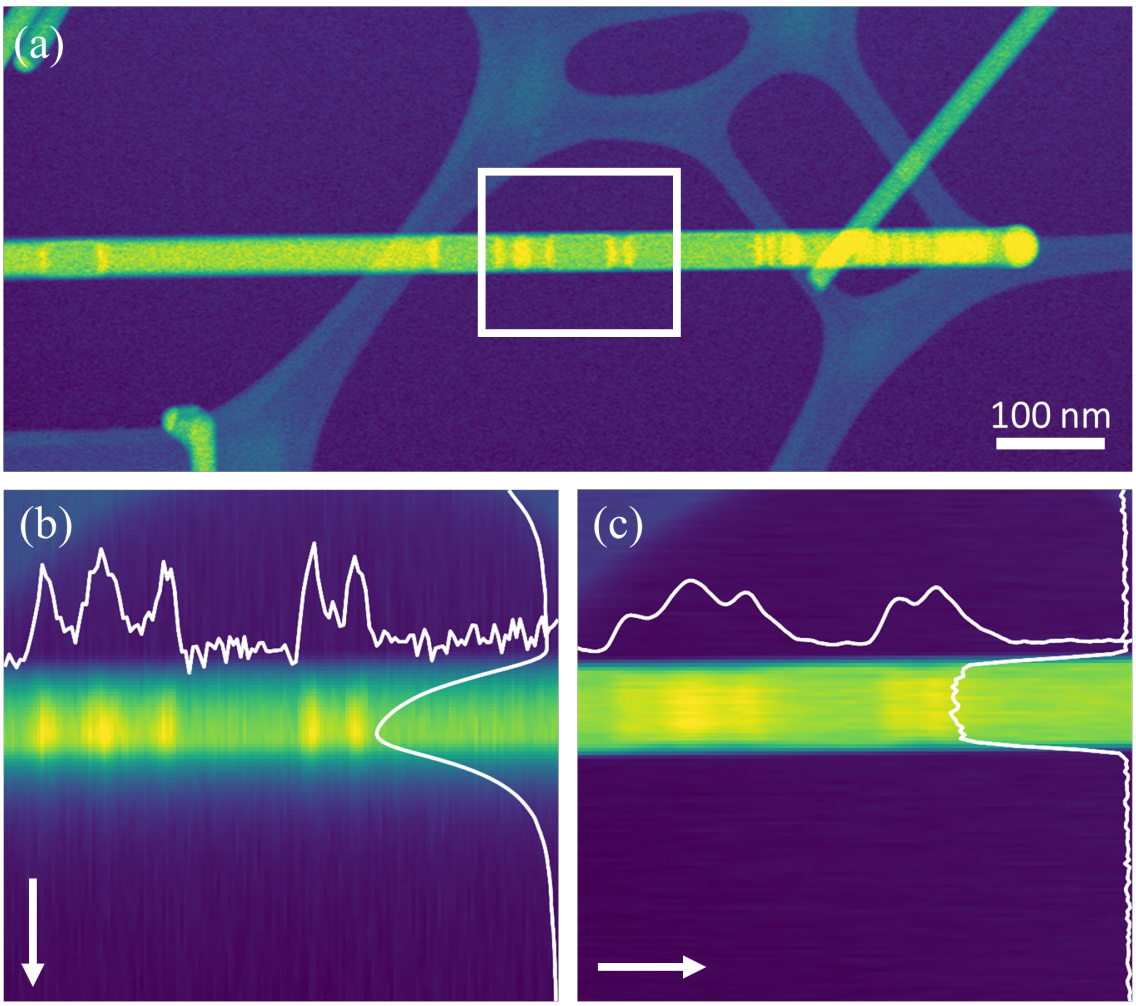

Figure 2.5.: **(a)**: Image of a silver nanowire captured at a dwell time of 1 μs with twin defect sites visible along the nanowire perpendicular to its length. Images **(b)** and **(c)** are from the white boxed region, with the white arrows representing the fast scan direction. **(b)**: Image created by summing 200 image frames, each with a 50 ns dwell-time. Intensity profiles along the length and across the width of the nanowire are overlaid. The widths of the twin defect sites are clear as they lie perpendicular to the fast scan direction, but the width of the nanowire is obscured by the signal streaking and afterglow. **(c)**: Image of the same region with the fast scan direction rotated 90°. In this case the widths of the defect sites are far more difficult to measure, but the width of the nanowire is very well defined.

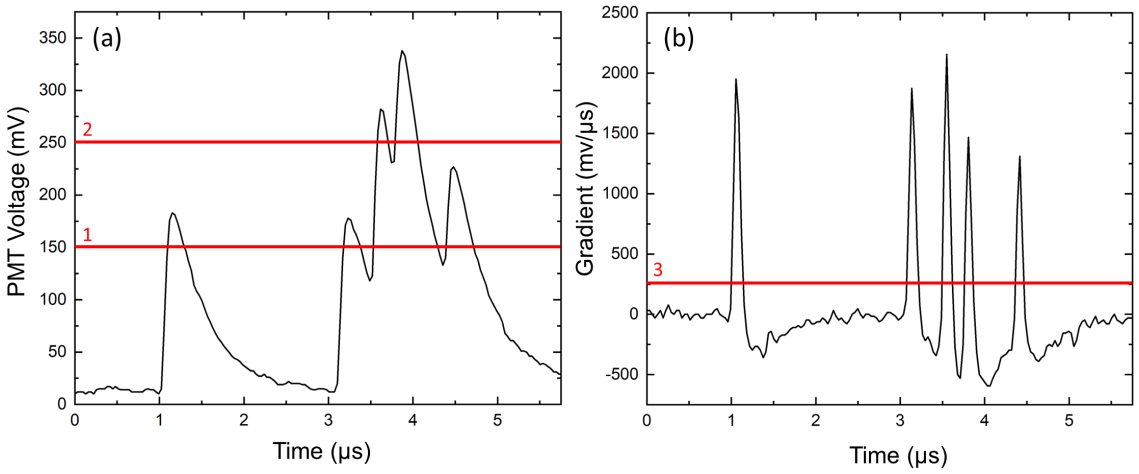

Figure 2.6.: (a): A series of five electron impacts, with one isolated, and the others piled-up. A single intensity threshold applied to this signal cannot capture all five electrons. The threshold labelled '1' is low enough to identify the first, second, third, and fifth electrons, but too low for fourth. While the higher threshold labelled '2' can identify the third and fourth electrons only. **(b)**: Each electron produces distinct, non-overlapping peaks in the gradient of the signal, allowing a single threshold, labelled '3', to be used to identify all electrons. Image adapted from [1].

The approach decided upon was to instead take the gradient of the detector's output and apply an intensity threshold to this instead. The reason for this is that each electron pulse, regardless of intensity, has a sharp rising edge (positive gradient), a peak (zero gradient), and a decaying edge (negative gradient). Hence, the gradient of a pulse will contain a much sharper peak, which also has a greater peak-to-background ratio, and can therefore more easily have a threshold applied, as shown in **Figure 2.6, (b)**.

As the peaks are much sharper, approximately 10x, when compared to the original detector output, this approach is far more resilient to pulse pile-up, which could be improved further with a device with a higher sampling rate. The benefits to this gradient-based approach are numerous; signal streaking is eliminated as each electron impact is localised to a single point in time, and the digital signal pro-

duced contains a count of the number of electrons which hit the detector during each dwell time, useful for comparison with simulations used for quantitative studies. The effects of detector inhomogeneity are also eliminated as all electron impacts are recorded with equal intensity, however this topic is covered in the next chapter. Before moving to specifics of our implementation, a brief overview of other's approaches to electron count imaging is mentioned.

2.3.1. Previous Approaches to Electron Counting

Now that the strengths of electron-count imaging have been introduced, it may come as no surprise that other approaches have been designed. When imaging at low-doses, most pixels will contain very few electrons, say between zero and three. Hence, the image histogram will contain peaks corresponding roughly to these pixel values, though these peaks are not sharp due to detector inhomogeneity causing a spread in the signal intensity due to electrons. Hence, one can determine appropriate threshold values for converting pixel values in the image to the number of electron impacts by looking at the 'valleys' in the histogram as boundaries between pixels containing differing numbers of electrons.

This has been applied to both SEM, where a comparative study shows an increase in SNR, contrast, and resolution, and STEM, where it was used to measure the thickness of w-AlN with ± 1 nm confidence [104, 105, 106]. While this works well, it does not have all the benefits of our approach, as signal streaking is not efficiently eliminated. Should signal streak from a pixel with two electron impacts to one neighbouring pixel containing none as an example, this second pixel may be attributed a value of one electron impact due to this streaking, where it should be

attributed zero.

Agarwal et al. applied an intensity threshold to the secondary electron (SE) detector's output to produce a digital signal after passing the output from an oscilloscope to a MATLAB script [107]. They used their previous study on the statistics of voltage pulses due to electron impacts to choose an appropriate threshold [108]. This functions similarly to the method shown in **Figure 2.6, (a)**, which is capable of eliminating streaking, but is susceptible to pile-up. By simultaneously capturing the timing data of scanning system along with the detector output they could easily reshape their digital datastream into images, making this a very practical approach, which saw SNR improvements of 30%.

One final approach for the STEM mentioned here is that by Mittelberger et al. [100]. Whenever a pixel's value crossed a threshold determined by the single electron level, the signal was integrated until a pixel is reached whose intensity was again below this threshold. This integrated signal is then assigned to the pixel which initially crossed this threshold. A second condition which stopped the integration when the number of pixels which contributes to the integral is greater than the length of a single impact is used to account for two closely spaced hits.

A sample of a gold nanoparticle on an amorphous carbon background was imaged in this study. While this method worked on the carbon background, the large atomic mass of the gold nanoparticle caused too many electrons to be scattered, and in turn, inseparable pile-up in the signal. All approaches described here balanced the precision of the approach with practicality of use and instrument limitations. While the approach here approach started similarly, it has iterated into a very capable digitisation device, with this development detailed in the following section.

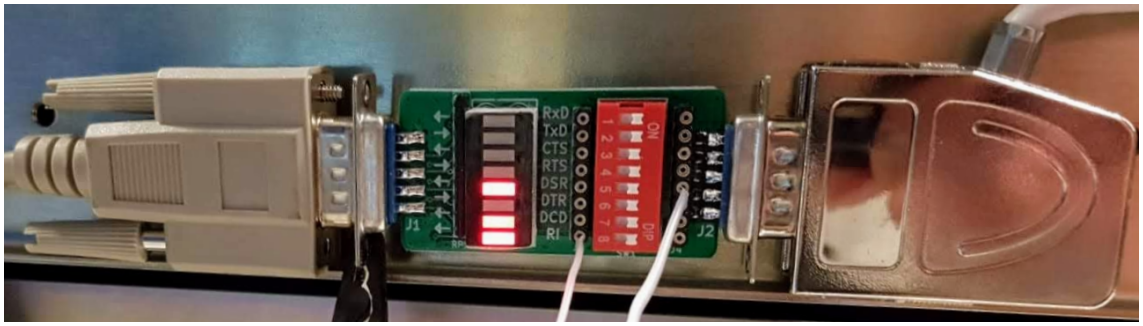

Figure 2.7.: A 9-pin breakout used to access the voltages in each channel of a D-sub 9 connector. This allowed the timing signals of the scan generator to be accessed.

2.3.2. Digitisation via a Streaming Oscilloscope

To implement a gradient-based digitisation approach, both a high sampling-rate (to minimise the likelihood of inseparable pile-up) and a method with which the gradient of the signal could be taken (to apply an intensity threshold) was required. For this, a USB-powered streaming oscilloscope (PicoScope 2206B) which could stream data directly from the HAADF detector to a MATLAB file was used. This has a sampling rate of 32 MHz and a data buffer limited only by the host PC's RAM. Suitable brightness and gain settings were set at the microscope to prevent clipping of the signal, and the voltage range and offset of the PicoScope were also set to maximise the dynamic range. The image size (in pixels), dwell time, and line flyback time are noted to enable reshaping of the datastream into an image later.

In theory it was possible to capture both the relevant timing signals and the data, however when both channels of the streaming oscilloscope were used, the sampling rate was shared between them. The resulting sampling rate of 16 MHz was not suitable for capturing the pulses. A 9-pin breakout was used to access the appropriate voltage reading to calculate the timings, shown in **Figure 2.7**.

Having streamed the data, the gradient is taken in MATLAB and a threshold

applied, either manually or with a built-in function such as *findpeaks*, producing the digital signal. To aid in this, a secondary script was produced which plotted a segment of the initial signal, the gradient with threshold overlaid, and the resulting digital signal. Using this, an appropriate threshold, i.e., one high enough to not count noise but low enough to not miss counts, could be chosen. With further hardware advances this should become automated in future.

To convert this digital signal to an image, first, an appropriate number of datapoints are binned using the known sampling rate of the oscilloscope and the pixel dwell time to form pixels. Using the image size and line flyback time these pixels are then combined into lines, and the lines into images. As the data collection is not synchronised to the scanning system it is likely the datastream will begin during an image frame and not at the beginning, and so extra data is captured on either end of the desired number of frames to be later trimmed to the appropriate size.

Using this approach, an image of a gold nanoparticle on an amorphous carbon background was captured on a Nion UltraSTEM 200. This demonstrated the ability to digitise signal from both low and high-scattering regions of the sample, with this result shown in **Figure 2.8**.

An astute reader may notice that **Figure 2.8** is a single, long image frame as opposed to a multiframe capture, the benefits of which have been repeatedly mentioned in this thesis. The reason for this is an issue with the hardware used here. Due to the oscilloscope having effectively only one usable input (as using the other simultaneously halved the sampling rate), only the detector output could be captured, and not the timing signals.

While not strictly a problem if timings are both known and fixed, as with the dwell time and line flyback time, when not fixed, these timings cannot be hardcoded to

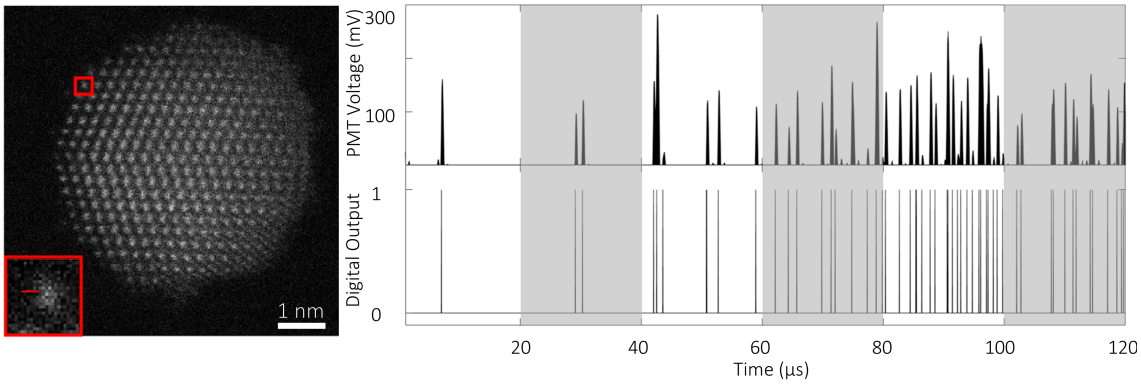

Figure 2.8.: Left: Digital image of a gold nanoparticle on an amorphous carbon background captured with a dwell time of 20 μs. **Right:** The detector output and corresponding digitised signal from the red line profile is shown. The line profiles is six pixels in length, which alternate grey and white. Note how the number of scattered electrons increases as the beam moves onto the gold atom, while the signal is still digitised. Image adapted from [1].

allow the reshaping of the datastream into an image or image stack. Unfortunately, the frame flyback time of the Digiscan II controlling the Nion was not fixed, so while capturing a single image frame was straightforward, multiframe captures became complex as the start of each different image frame in the datastream needed to be manually identified. This was a very time-consuming process, if not impossible when SNRs are low, however a demonstration of summing 20 low dose frames is shown in **Figure 2.9**.

Even though there was little difficulty forming single images, this process was not live and did not provide immediate feedback to the microscope operator. While these initial results were promising and proved the gradient-based digitisation approach was feasible, it was clear that new hardware was required.

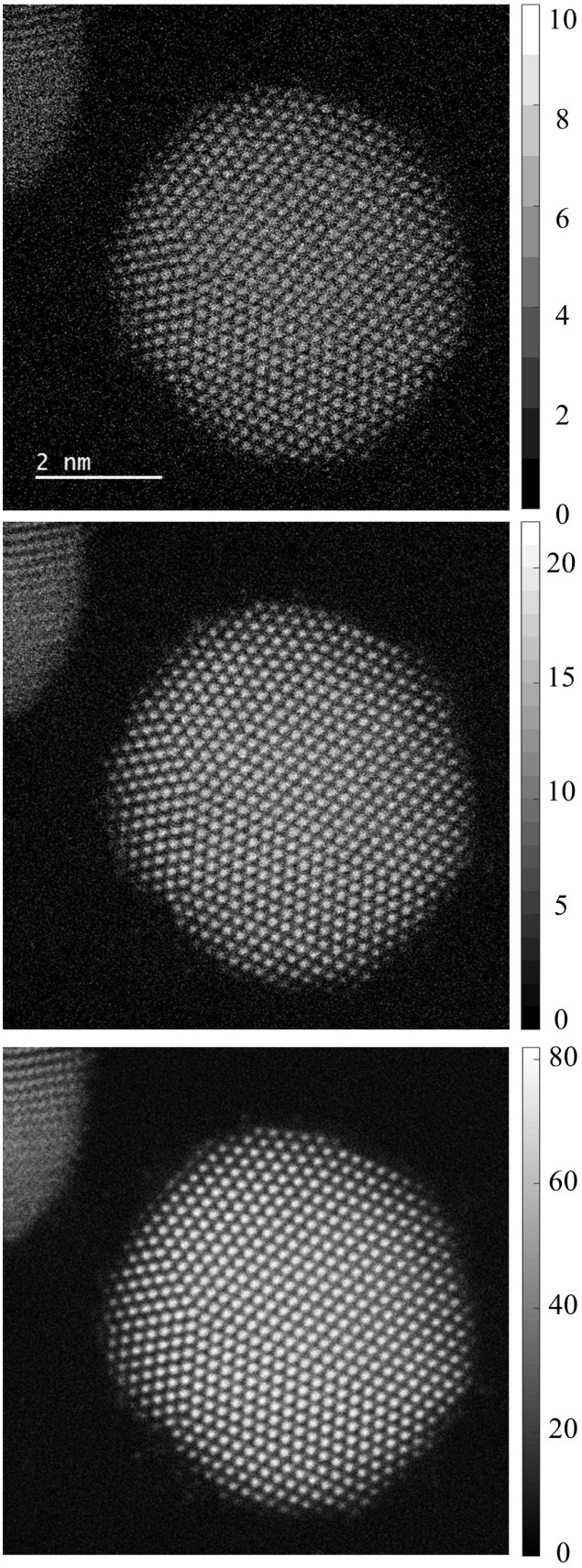

Figure 2.9: One frame, four frames, and 20 image frames of a gold nanoparticle on an amorphous carbon background which have been rigidly aligned and summed. A dwell time of 2 μs and a $\sim$5 pA beam current was used. The colourbars are in units of integer number of electron impacts per pixel. Image adapted from [1].

2.3.3. In-hardware Signal Digitisation

The new hardware approach chosen was to use a field-programmable gate array (FPGA). FPGAs allow the implementation of custom microcircuitry through the use of a hardware description language, such as Verilog. This accessible approach provides abstraction from transistor level logic while still giving access to the high communication speeds with other electronic components. The product initially chosen to do this was the Red Pitaya STEMlab 125-14, with two 125 Msps (8 ns time step) inputs, and a Xylinx Zynq 7010 FPGA, capable of digitising a detector signal in-hardware and outputting this signal directly.

By doing so, this signal can be connected to a detector input on a scan generator, forming an image directly at the microscope's control / acquisition computer. This also avoids the need to capture the timing signals simultaneously with the signal, as the scan generator simply interprets the digital signal as the output from a detector, natively forming an image as with any other signal.

The FPGA also allows for a variety of signal processing options, with a Python interface viewable on the microscope's control computer used to facilitate changing these settings. These include the time difference used for calculating the signal's gradient, the number of samples for which a signal needs to cross the threshold for it to be registered as an electron impact, and the width of the output digital pulses. The Red Pitaya outputs quite a weak signal, while TEMs typically use 50 Ω transmission lines. A buffer amplifier circuit was designed to increase the amplitude of the digital signal, allowing for full use of the dynamic range of the scan generator's input. Images of the hardware used, and also the Python interface is shown in **Figure 2.10**.

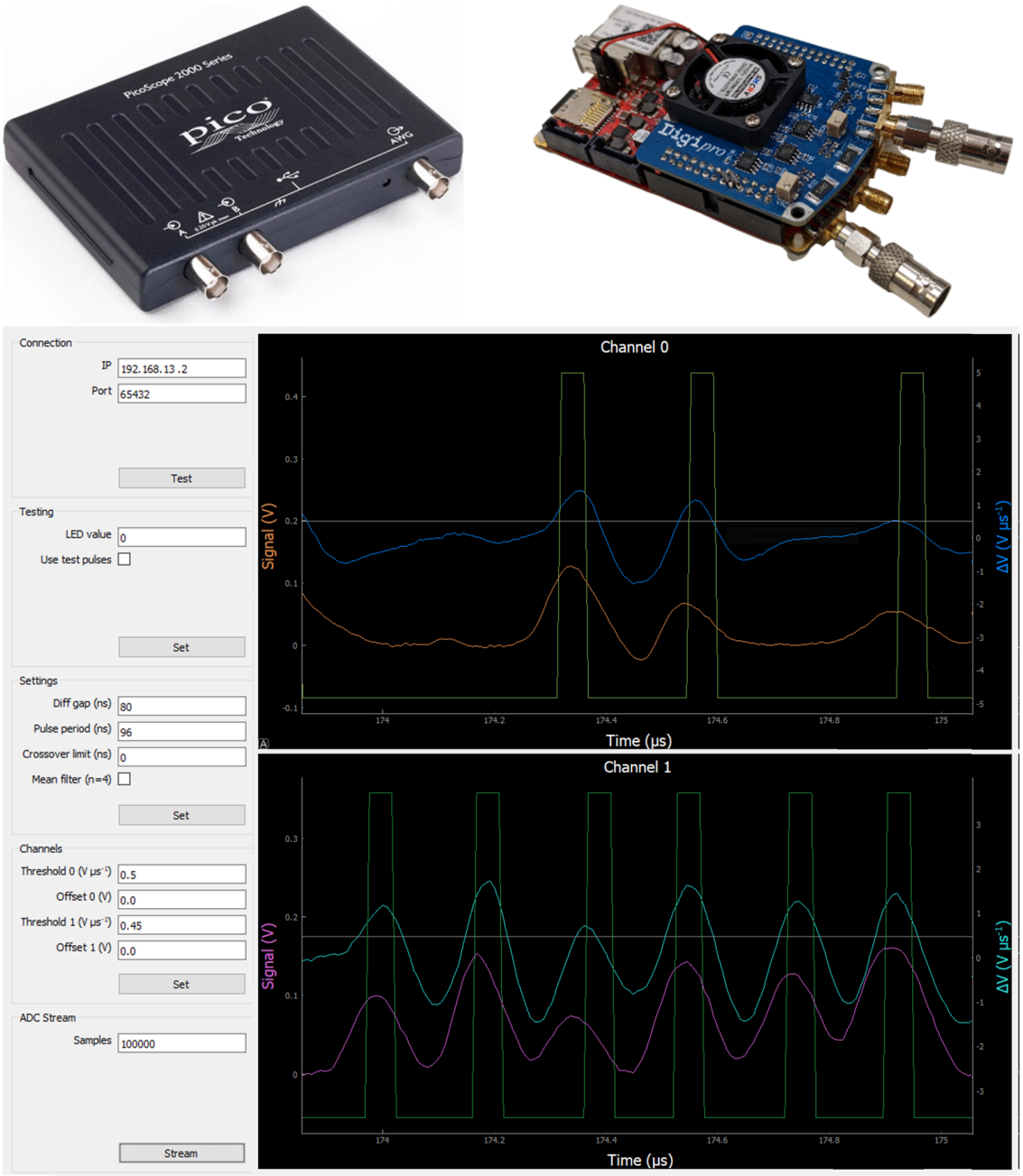

Figure 2.10.: Development of the hardware used for STEM signal digitisation. First, the PicoScope 2206B USB-streaming oscilloscope was used to capture data for later digitisation via postprocessing. The later approach was to use a Red Pitaya paired with an amplification board to enable live digitisation and digital image formation. A screenshot of the interface used to view the raw data stream, its gradient, the digitised signal, and digitisation parameters is also shown.

2.4. Results

2.4.1. Radiation Sensitive Sample

As the motivation behind developing this digitisation technique was to avoid sample damage, here, examples of data from a radiation sensitive sample are presented. This sample is a chemically fixed human monocyte derived macrophage cell which has been exposed to graphene for toxicity testing. An image of this, presented as a montage of digital counted images is shown in **Figure 2.11a**.

This image was captured on an FEI G2 Titan operated at 300 kV using a Fischione Model 3000 ADF detector. When imaging such a sample, low-dose techniques are required lest the sample be destroyed, and as previously described, the most accessible approach to doing so is to scan faster and at a lower-dose. An analog versus digital comparison of a section from the montage is shown in **Figure 2.11b**, which was formed by averaging 200 image frames with a 50 ns dwell time, measuring 512 pixels wide by 256 pixels high. The use of the FPGA counting approach allowed for the large number of image frames required to reach an appropriate SNR to be captured, and avoided the prohibitive requirement of extracting these frames manually.

As the pixel dwell time here is far shorter than the decay time of the electron pulse, as shown in **Figure 2.4**, a streaking artefact is clearly visible in the analog image in the fast scanning direction across the entire image, but is entirely absent in the counted image. While the net streaking effect is seen in the averaged image, an individual image frame is also included in **Figure 2.11c**, to demonstrate the streaking of individual electron signals visible in each single frame.

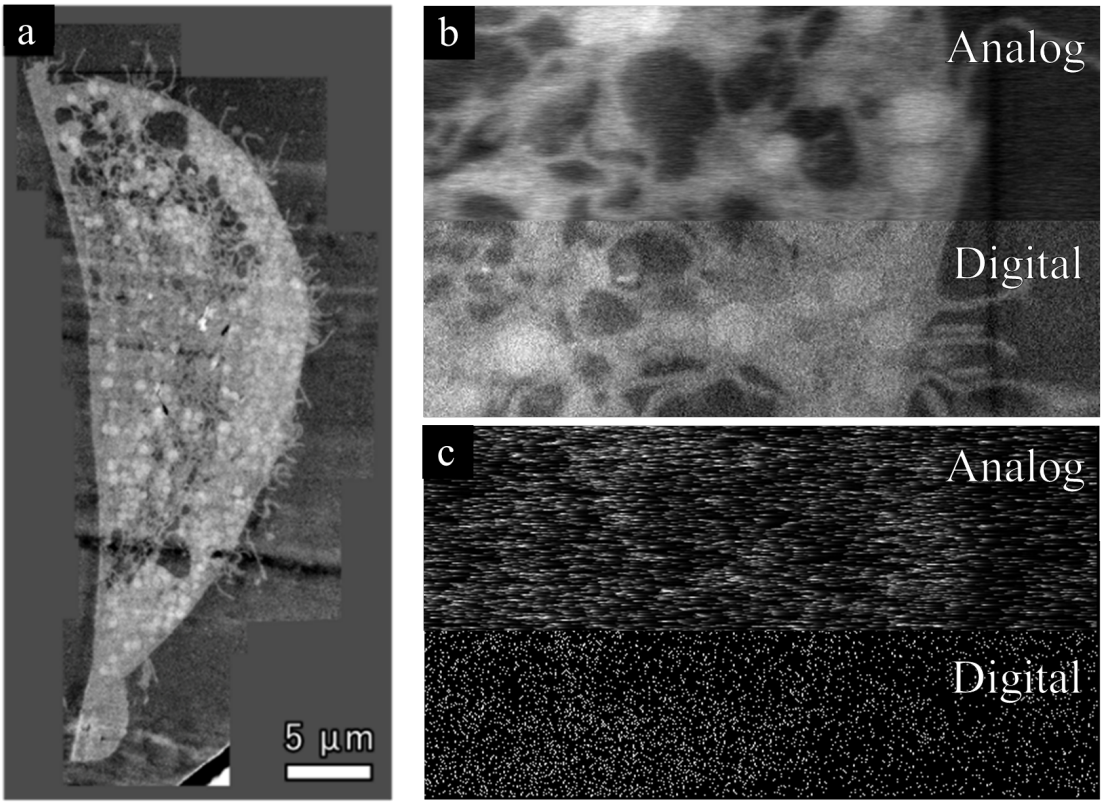

Figure 2.11.: The effects of digitisation on an image of a fixed human monocyte derived macrophage cell. A digital montage image of an entire cell is shown in **(a)**, comprised of different images, each an average of 200 frames captured with a 50 ns dwell time. An analog versus digital comparison of a region of this montage is presented in **(b)**, with severe streaking seen in the analog image, and none seen in the digital image. Below, the comparison of a single frame from the same region is shown, with the streaking of single electron impacts noticeable. Image adapted from [109].

2.4.2. Eliminating Signal Afterglow

To demonstrate the removal of afterglow from an image, a sample must be appropriately chosen to first make this afterglow apparent. A readily available sample which can be used to achieve this is a lamella, as a low magnification image of such a sample contains the bright lamella next to a large vacuum region. Shown in **Figure 2.12** is low magnification image of a lamella of strontium titanate ($SrTiO_3$) captured using a FEI G2 Titan equipped with a Fischione 3000 ADF detector.

In this image a comparison is presented between the analog and digital data, where contrast has been enhanced equally in each to highlight the afterglow. While in the analog image the afterglow is seen to persist across a large amount of the image, it is entirely absent in the digital image. This is because the afterglow effectively adds a small offset to the detector's output, which is not detected as signal using the digitisation method presented here.

While the origin of the afterglow is not exactly known, it can be described parametrically as a function of time, t.

$$Ae^{-t/b} + C, \tag{2.1}$$

where A is the amplitude, C is the offset, and b describes the decay time. Using the data from the region marked with the white arrow, the afterglow was measured to have a decay constant of 4.5 ± 0.4 μs, approximately ten times larger than that of a single electron signal. The magnitude of this decay is also shown to initially have an amplitude an order of magnitude larger than the single electron signal, affecting conventional, analog scanned images greatly. Thankfully through the use of digitisation, both signal streaking and afterglow can be removed from images.

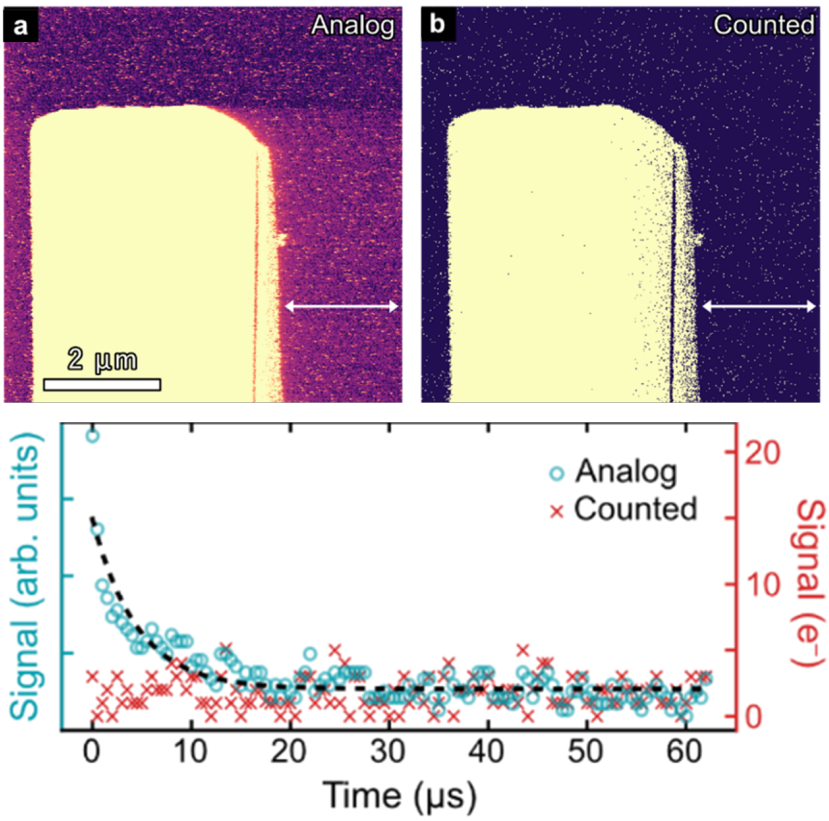

Figure 2.12.: Analog and digital images, **(a)** and **(b)** respectively, of a lamella of $SrTiO_3$ surrounded by vacuum. The images shown are the average of 50 frames each captured with a 500 ns dwell time. The decay of the afterglow is measured from the region marked with the white arrow, shown below the images. An exponential decay in the intensity of the afterglow is seen in the analog image, but is absent in the digital image. Image adapted from [109].

2.4.3. Graphene

Although the motivation for digitisation was to allow low-dose imaging conditions to be used to image fragile samples, it is applicable wherever a low amount of signal is reaching the HAADF detector. This has all the same benefits of removing signal streaking, afterglow, and other noise, producing higher SNR, quantitative images. One such case is imaging monolayers of graphene.

The signal reaching the HAADF detector scales with approximately the square

of the atomic weight of the sample, and so a single layer of carbon, with an atomic number Z = 6, causes extremely few electrons to be scattered to the detector. In this case, images are again dominated by signal streaking, and digitisation can be employed to produce higher quality images.

To demonstrate this, an experiment was designed to image a monolayer of graphene using a JEOL JEM-ARM300F GRAND ARM equipped with custom, low-inductance scanning coils. This allows for high-framerate imaging without hysteresis effects in the coils causing image distortions, as detailed in [110]. This experiment allowed for high-framerate, low-SNR imaging, and also an opportunity to test the digitisation equipment on a JEOL electron microscope with the original equipment manufacturer (OEM) scan generator. All previous digital data shown was captured on a Nion equipped with a DigiScan II, or FEI microscope with a DISS 6 scan generator, each having a digital input where the digitised signal could be streamed to.

The pulse shape produced by the JEOL detector is very similar to that produced by the detector on the Nion and caused no issues to digitise. However, the lack of a digital input caused issues which required new approaches to be overcome. Although a digitial signal leaves the equipment, this is then converted back to an analog signal by the scan generator. Due to an impedance mismatch between the scan generator's input and the BNC connector, the output digital pulses were broadened, and ringing was also present on this now analog signal. This manifested in the images as an artefact similar to signal streaking, although not caused the decay time of the scintillator.

The solution to this was to turn to postprocessing. At the signal level used in these experiments, nearly every pixel contained no signal, while some pixels contained signal due to a single electron impact. By cross referencing oscilloscope traces of

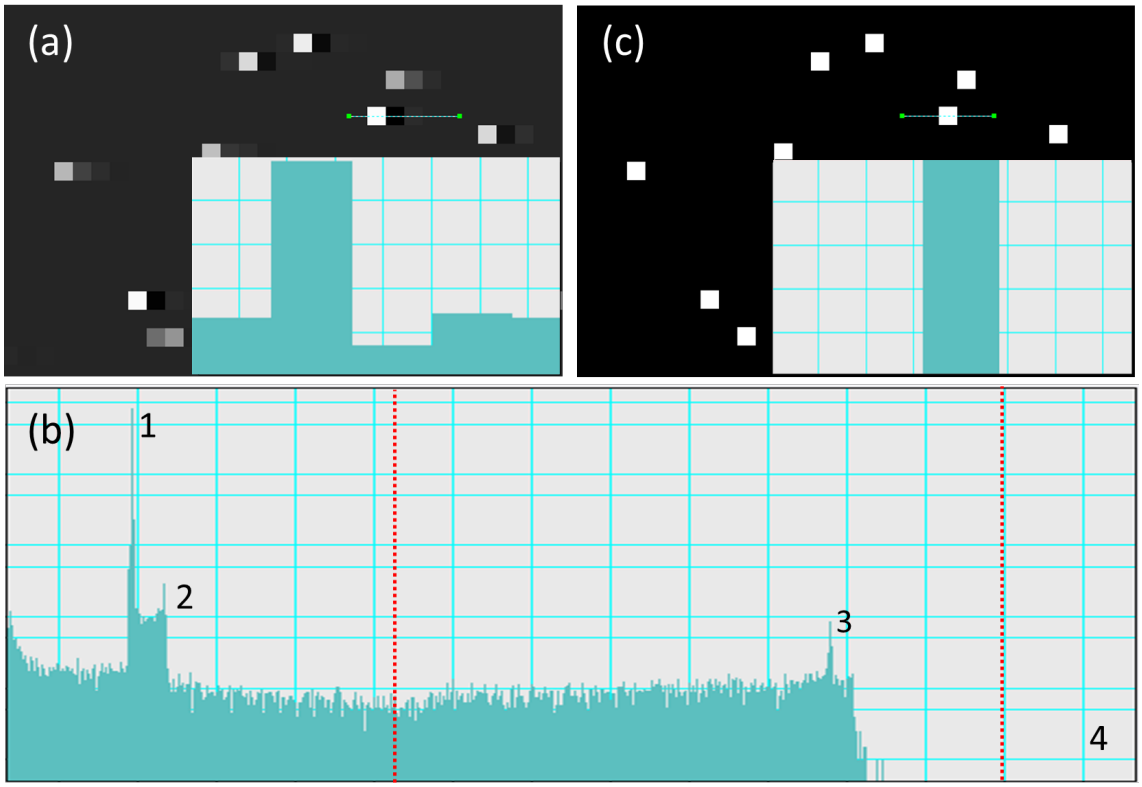

Figure 2.13.: The effect of inputting a digital signal into an analog input with an impedance mismatch. **(a)**: A single image frame showing signal streaking and signal ringing, with this highlighted by the line profile. **(b)**: Log-scale histogram of a single image frame. This is split into three regions by dashed red vertical lines, and with four points of interest labelled with numbers, explained fully in the text. **(c)**: The same single image frame after appropriate thresholds have been determined from the histogram have been used to update the pixel values.

digital pulses leaving the scan generator, line profiles of single electron impacts in the image, and the image histogram, it was possible to fully understand the grey levels in the image and choose thresholds which could be applied to the image, converting pixel values back to their digital values. This process is shown in **Figure 2.13**.

Understanding the histogram in this image requires careful explanation and this underpins the method by which the ringing and signal streaking can be removed. Four points of interest in the histogram, displayed on a log-scale, labelled numeri-

cally, will be explained here.

1. The peak corresponding to the zero level of the image. Any signal less than this peak is caused by a pixel whose value has been reduced below the background level by negative ringing in the signal.

2. This peak corresponds to pixels whose value has been slightly increased above the background level by a small amount of positive ringing from a previous pixel.

3. This is the peak corresponding to a pixel in which there was a single electron impact. Values to the left and right of this peak can similarly be explained by the combination of a pixel having this peak's value, and either negative or positive ringing.

4. Although not possible to see in this image, a small peak here is due to pixels in which there were two electron impacts.

The above conclusions were reached via careful observation of pixel values in the image. Understanding the histogram, it is now possible to determine appropriate thresholds with which the pixel values can be updated, with this process being performed in Python.

These thresholds are visible in **Figure 2.13** as red dashed lines. The first threshold is the value for which any pixel having a lower value is assigned a value of zero electrons, and any above with a value of one electron. Any pixel with a value greater than the second threshold is assigned a value of two electrons. While there is a range of exact values where these thresholds could be placed, so few pixels are affected by

varying the threshold a small amount that the overall effect on the final image is minimal.

One further step required to form images with suitably high SNRs was aligning and averaging the image frames, of which up to 2000 were captured, a feat previously impossible with the streaming oscilloscope. With too little signal available in each individual frame to align the dataset, frames were first binned such that there was enough signal to align them and measure the drift. Having aligned the binned dataset, the drift vectors exported to Python where a script was written to linearly interpolate the drift vectors back to the size of the original dataset. These interpolated drift vectors where then used to correct for the drift in the original dataset more accurately than the drift was corrected in the binned dataset. An example of this process is shown in **Figure 2.14**.

In this figure the monolayer of graphene was imaged on a JEOL JEM-ARM300F GRAND ARM operated at 80 kV. A dwell time of 83 ns, a beam current of 33 pA, and an image size of 512 $\times$ 512 pixels was used, although this is cropped in the figure. This combination of imaging settings achieves a framerate of approximately 31 frames-per-second (f.p.s). To contrast this, an image captured with the same image dimensions but where each line in the image begins at the same point in a 50 Hz cycle (called line-synchronisation) has a framerate of 0.098 f.p.s.. Even in studies where the emphasis is placed on capturing many frames at high speeds with a dwell times of 1 μs, a framerate of 1.93 f.p.s. is achieved [94].

While there is often a trade-off between spatial and temporal resolution, as imaging at faster scanning speeds will lower the SNR, with the data analysis method proposed here both spatial and temporal resolution are high. Of note in **Figure 2.14 (d)**, are the brighter atoms surrounding the monovacancy. This is believed to

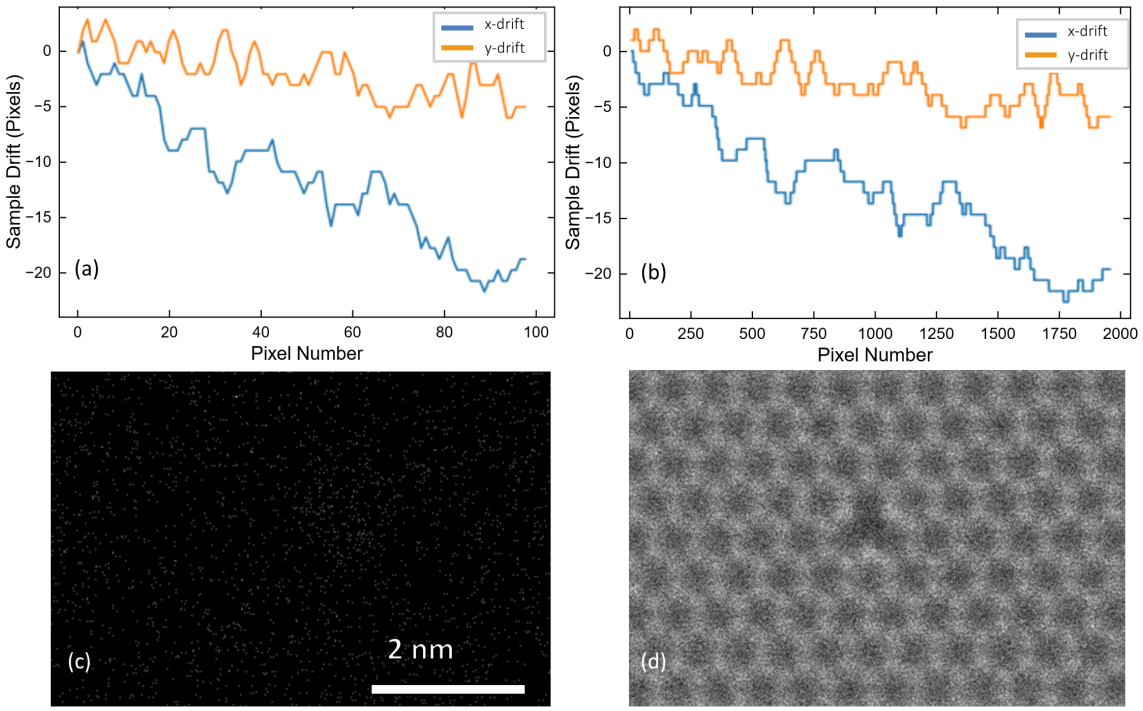

Figure 2.14.: The process of aligning 2000 image frames of a monolayer of graphene with a single vacancy. **(a)**: The drift vectors after aligning the dataset which was binned by 40 times to produce a stacked image with 50 frames. **(b)**: The drift vectors after interpolation onto an x-axis 2000 datapoints in size; the original size of the dataset. **(c)**: A single image frame from the original dataset, where no structure can be seen. **(d)**: The final image of graphene, where each frame has had an alignment applied to it before averaging.

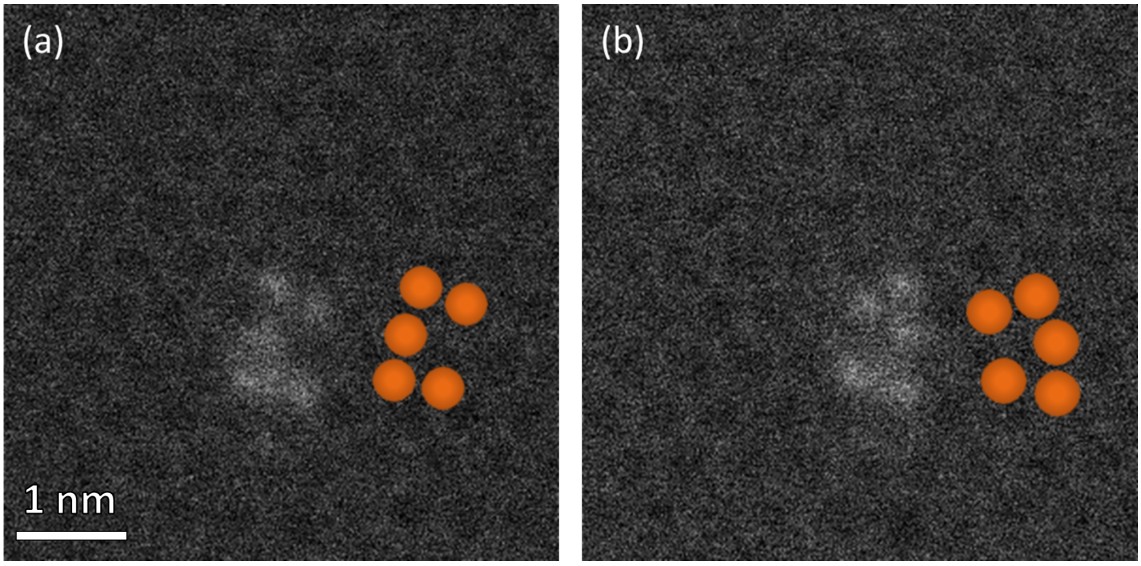

Figure 2.15.: Conformation switching of a cluster of five silicon atoms on a monolayer of graphene observed at over 31 f.p.s. using digital imaging. The atom in the centre of the clusters moves from the left in **(a)**, to the right in **(b)**. A representation of the structure of the cluster of atoms is shown in orange to aid interpretability. Image frames were summed to increase SNR for observation in this image.

be caused by a larger Debye-Waller factor, and demonstrates the precision of this technique, although investigations are ongoing to confirm this.

While a high framerate was achieved in **Figure 2.14**, there were no dynamics to observe. To demonstrate what high temporal resolution can achieve, another dataset from the same sample is shown in **Figure 2.15**.

In this figure the conformation switching of a cluster of five silicon atoms is observed. Although only two stills of the switching are presented, this was observed to be oscillatory. Research is ongoing into explaining the nature of these oscillations and calculating the 3D structure of the cluster. A previous work observed similar behaviour of a cluster of six silicon atoms trapped in a graphene nanopore [111]. However, in this work the duration of a single image frame was ∼6 s, and so they concluded that the conformational transformation occurs reversibly in less than ∼10 s.

This is in contrast to these results where the frame time is ~ 0.03 s, an improvement in temporal resolution of nearly 200 times.

The importance of the results from these experiments with graphene in relation to the digitisation equipment is twofold. Firstly, it has been shown that the equipment is able to produce digital images even when a digital input is not present. Despite the barriers of losing the digital count and ringing on the signal, both could be overcome with appropriate postprocessing of the data. Secondly, as digitisation increases the SNR of high-framerate data by eliminating signal streaking, detector afterglow, and other sources of noise, it is not strictly necessary to choose between spatial and temporal resolution. This is demonstrated in **Figure 2.14** and **Figure 2.15**, which were both captured at framerates of $\sim$31 f.p.s (6 f.p.s faster than the current published record for a conventional scan [110]) and low beam currents, yet show atomic resolution images with appropriate alignment.

Conclusions

In this chapter the topic of signal digitisation and its effects on images were discussed. Particularly, how it eliminates signal streaking from images captured at low-doses and high scanning speeds. As *only* electrons are counted as signal, a longer afterglow decay which is present in conventional analog images is also removed.

When such sources of noise are present in every frame of a dataset containing 2000 images, when aligned, the final image is heavily degraded. It is only by digitisation and elimination of these sources of noise that these high-framerate, low-dose studies become possible.

The ability to remove signal streaking was demonstrated by imaging a biological

tissue, and the elimination of afterglow was shown in an image of lamella. Graphene was also imaged to demonstrate how both high spatial and temporal resolution can be achieved in the same dataset. The latter data was produced on an instrument lacking a digital input, and the methods by which the data could be processed to overcome the subsequent issues caused by this was also discussed, demonstrating the capability of the digitisation hardware to work with any microscope.

This digitisation approach also represents a sustainable, cost-efficient way of increasing the performance of existing detectors. This democratises access to some state of the art techniques and is far more sustainable than purchasing a new detector when an upgrade to an older one may be suitable.

In the next chapter, we move towards quantifying the effects of digitisation. Detector inhomogeneity and how it is dramatically improved via digitisation is discussed, along with code developed to add streaking to simulated images, allowing for its effects to be isolated, on both images and their Fourier transforms.

Chapter 3.

Quantitative Improvements of Digitisation

In the previous chapter the topic of signal digitisation was introduced, namely with reference to removing signal streaking and detector afterglow from images. The motivation for doing so is that these imaging artefacts heavily degrade images when operating at short dwell times and low beam currents. The significance of this being that these operating conditions are a universal approach to low-dose imaging in the STEM. In this chapter, the focus turns to how digitisation decreases detector inhomogeneity, and interestingly, *adding* streaking to simulated images to better understand its effects.

3.1. Quantifying Detector Performance

One issue with image formation in the STEM is that when electrons hit the detector, the resulting output voltage is converted to an arbitrary grey value in the image's

pixels with no physical meaning. For this reason, STEM quantification is a field with much interest as it allows these arbitrary grey values to be converted to a meaningful unit, such as fractional beam intensity [112, 113, 114]. When used with HAADF STEM, which is known to have mass-thickness contrast, this allows either mass or thickness studies of a sample where one of these variables is known.

Quantifying a STEM image in this way requires comparison with a simulation. However, simulations often model the detector as perfectly round and symmetric, and with an equal response to all electrons. What is required is to incorporate the actual detector used into the simulations to allow for a fair comparison. This is done via detector mapping, which is described in the following section.

3.1.1. Detector Mapping

A detector map, often referred to as a detector scan, is a method via which the detector itself is imaged using the full intensity of the electron beam, or a fixed, known fraction of the beam [114]. The way to do so varies with instrument, but the general approach is to first move a vacuum region in the sample to ensure that the full beam reaches the detector uninterrupted, and then focus the electron beam at the detector plane by switching to diffractive or confocal mode while the detector is inserted.

When imaging an annular detector, the central hole allows for a measure of the vacuum level (or the D.C offset), and the gain of the amplifying electronics can be measured [114]. By first subtracting the D.C offset from an image and then dividing the image by the gain, its pixels are converted to having units of fraction of incident beam intensity. The detector map must be captured at the same detector settings

(brightness and gain), although imaging settings can vary e.g., beam current or dwell time, if done so by a known amount to be later accounted for.

An issue with this however was previously stated, which is that detectors are often modelled as being 'perfect', with no variations in shape or response [115]. This too can be accounted for by further analysis of detector maps. For example, following the methodology from MacArthur et. al. [114], the flatness, roundness, smoothness, and ellipticity of detector can also be measured. As these definitions are used in this chapter, they are reproduced here for ease of reading.

- Flatness: Detector sensitivity with respect to scattering angle (radially) after averaging azimuthally.
- Roundness: A measure of the consistency of the detector sensitivity around the detector (azimuthally) after averaging radially.
- Smoothness: The full-width-quarter-maximum of the active region of the normalised histogram.
- Ellipticity: The percentage of the major of the minor diameters of the inner-angle opening.

An example of a detector map is shown in **Figure 3.1**.

As we can see in this image, the detector shown is far from perfect. A visual observation shows darker regions corresponding to a drop in the detector's response, and the serrations on the left from the scintillator gripping clips are clear deviations from a perfect circle. Quantitatively, it was calculated that the response of this detector varies from the ideal case from as low as 1.88 % when considering its ellipticity, to as high as nearly 30 % for its smoothness. Understanding the variations

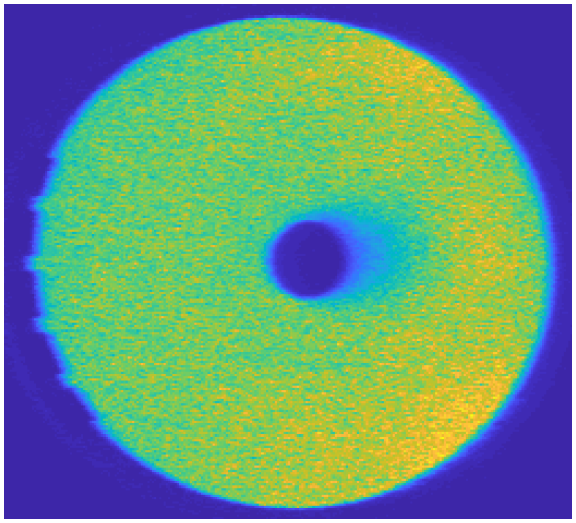

Figure 3.1.: Example of a typical detector map. A dark region to the right of the central hole is visible, as are two brighter regions nearer the edges. Serrations on the left due to scintillator gripping clips are also seen. Adapted from [1].

of a detector from the 'perfect' model used in simulations in this way increases the understanding of errors which may arise in image quantification.

A variation of particular interest in this thesis due to its relationship to signal digitisation is detector inhomogeneity, as explored in the following section.

3.1.2. Detector Inhomogeneity

As electrons which are scattered to the HAADF detector have been elastically scattered, each should produce an identical output in the detector's response. However, this is not the case, as evidenced from the dark regions in the detector map in **Figure 3.1**. This issue may be inherent due to the design of the detector. For example, for the detector shown in **Figure 3.1**, it is known that the PMT and readout electronics are located on the left side of the image (the reader may also refer to **Figure 1.6** for a diagram). Due to this, photons which are produced when electrons hit

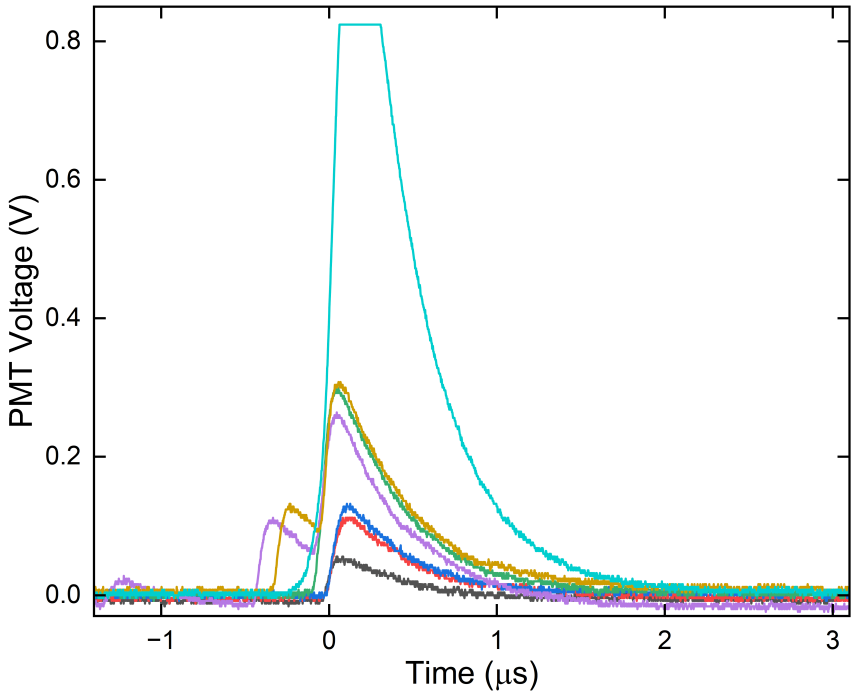

Figure 3.2.: Oscilloscope traces of single electron impacts, all captured at the same imaging settings. While some have intensities as low as 100 mV, others are nearly as large as 1 V. This large variation in intensities is due to detector inhomogeneity.

the detector to the right of the central hole may not traverse around the hole and reach the PMT. If only a fraction of the photons produced contribute to the output signal, the output will of course be smaller, contributing to detector inhomogeneity.

Another example of a contributing factor is impurities in the scintillating crystal which dramatically lower luminescence efficiency [68]. Some steps have been taken to counteract this, such as adding a layer of P47 scintillator to a detector to increase detection efficiency [69]. To demonstrate the effects of detector inhomogeneity on the detector's output, a series of single electron pulses were captured with an oscilloscope for fixed imaging settings, as shown in **Figure 3.2**.

In this figure, for fixed detector brightness, gain, and electron beam energy, a very large variation in pulse height is seen. Their intensities range from less than

100 mV, to greater than 1V, although this largest pulse is clipping on the detector output and is in fact even larger. This wide range in intensities is one of the many ways in which detectors differ from the ideal, however it is also one which can be eliminated via signal digitisation.

3.2. The Effects of Signal Digitisation on Detector Performance

When signal digitisation was initially introduced, the focus was on how it eliminated signal streaking and detector afterglow and provided a quantitative count of the number of electrons which hit the detector. An additional benefit however, is that it also massively reduces the effects of detector inhomogeneity, as all electrons in the digital signal are recorded with equal intensity (a digital '1'). To demonstrate the effects of signal digitisation on detector performance, detector maps from eight different detectors from five different companies were captured. As the digitisation equipment allows for simultaneous capture of the digital and original analog data, their comparison is shown and metrics evaluated in **Figure 3.3**.

If we first consider the analog performance of the above detectors, there are many features to note. In nearly all detectors we see an asymmetric response, likely to be caused by the position of the readout electronics as previously discussed. However, even in detectors with an obvious asymmetry in the response, other dark regions are seen unrelated to this asymmetry, such as in detector B, caused by other defects. When comparing across the four metrics, we see that no single detector is the best in every category. Detector I is on average the best, which may be explained by the

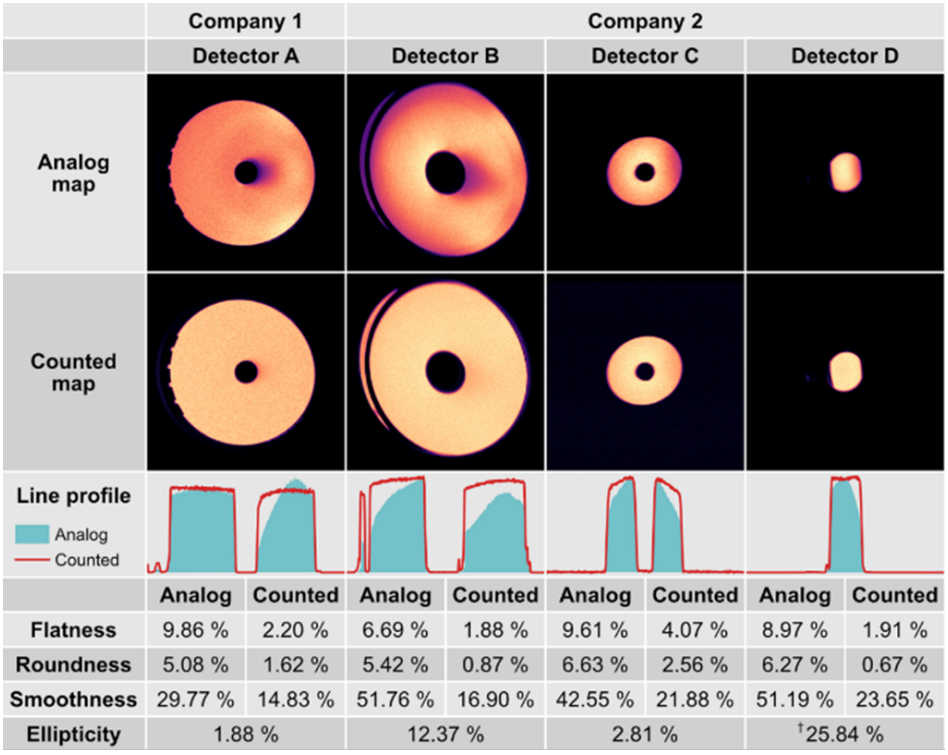

	Analog	Counted	Analog	Counted	Analog	Counted	Analog	Counted
Flatness	9.86 %	2.20 %	6.69 %	1.88 %	9.61 %	4.07 %	8.97 %	1.91 %
Roundness	5.08 %	1.62 %	5.42 %	0.87 %	6.63 %	2.56 %	6.27 %	0.67 %
Smoothness	29.77 %	14.83 %	51.76 %	16.90 %	42.55 %	21.88 %	51.19 %	23.65 %
Ellipticity	1.88 %		12.37 %		2.81 %		†25.84 %	

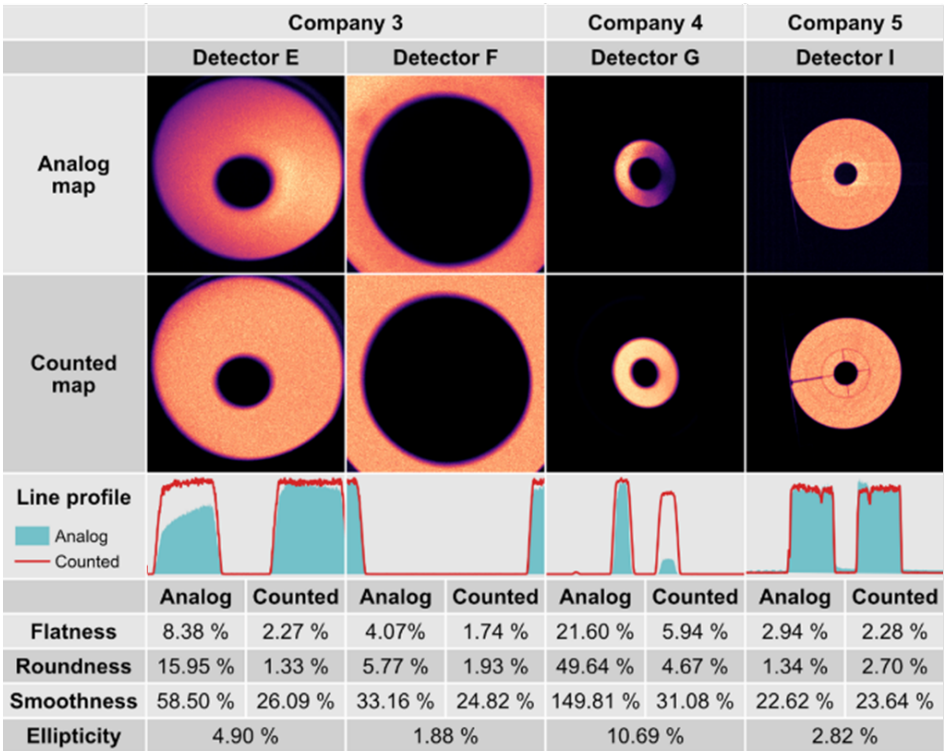

	Analog	Counted	Analog	Counted	Analog	Counted	Analog	Counted
Flatness	8.38 %	2.27 %	4.07%	1.74 %	21.60 %	5.94 %	2.94 %	2.28 %
Roundness	15.95 %	1.33 %	5.77 %	1.93 %	49.64 %	4.67 %	1.34 %	2.70 %
Smoothness	58.50 %	26.09 %	33.16 %	24.82 %	149.81 %	31.08 %	22.62 %	23.64 %
Ellipticity	4.90 %		1.88 %		10.69 %		2.82 %	

Figure 3.3.: Detector maps of eight electron detectors from five difference manufacturers. Flatness, roundness, smoothness, and ellipticity values are given as a measure of the deviation from a perfect detector for the simultaneously captured analog and digital data. Image adapted with permission from [109].

fact it is a solid-state detector, and not scintillator-PMT based.

If we for now limit the discussion to the more widely used scintillator-PMT based detectors (detectors A - G), while we see that detector A is both the most smooth and round and tied for least elliptical, it is the second least flat detector. For someone performing compositional studies of a material then this detector is not ideal due to its large inhomogeneity, despite its otherwise strong metrics. For quantitative studies where a precisely defined the inner-angle is important, a detector with a low ellipticity measurement is recommended. The ellipticity measurement of detector D, marked with a †, uses the outer radius as opposed to inner radius.

Detector I has lower metrics in all categories except ellipticity, although it is not far behind detectors A and F. In this solid-state detector, electrons are converted directly to charge as opposed to an intermediate stage of photon conversion. While this avoids many issues, there are readout channels which result in electron detection dead zones, which may result in some minor loss of detection efficiency. This detector is also a segmented detector, having two outer rings and four inner segments constituting one ring. It can be seen that the inner rings are brighter than the outer rings in the analog scan, however a gain reference can eliminate this if required.

Moving onto discussing the results of digitisation, we can see that all metrics for all detectors decrease, bar a single exception. For detector G we see the largest improvements, with the roundness and smoothness deviations decreasing by nearly 45 % and 120 % respectively. Across all detectors, we see the average deviation decrease from 9.01 % to 2.79 % for flatness, from 12.01 % to 2.04 % for roundness, and from 54.92 % to 22.86 % for smoothness. These results do not invalidate the previous discussion of analog performance, as such a study allows those without access to digitisation methods to better know the strengths and weaknesses of either detec-

tors they currently have equipped, or to be better informed when purchasing a new detector. In **Figure 3.3** company names are not shown, however it is recommended that users perform this analysis on their own system.

Understanding that all electrons are recorded equally in the digital signal, it is no surprise that the digital performance of the detectors is better as the flatness, roundness, and smoothness all depend on the single electron response. This improvement is further evidenced by the significantly flatter digital line profiles when compared to the analog ones. As all electrons are recorded with equal intensity, and assuming an isotropic distribution of scattered electrons, for darker regions to still exist in the digital detector maps implies that some electrons are not being counted. Some electrons in these regions produce so few photons capable of reaching the PMT that the pulse in the output voltage is too small to cross the threshold to be counted as an electron. As the threshold is set just above the noise level, this means that the signal too is below the noise level and would not contribute meaningfully to an analog image either.

Only one metric increases in its deviation from the ideal case when digitisation is used, and this is the smoothness of detector I, which increases slightly from 22.62 % to 23.64 %. For this detector the readout channels between segments become more pronounced when digitised, resulting in less uniformity. This is likely due to the effective filtering of low energy secondary electrons which are generated when the primary electron beam is incident on material between the segments [109].

Overall, it has been shown that digitisation brings detectors closer to their counterparts used in simulations, and so too are images brought closer to simulation. However, one important factor has not been covered in this discussion of detectors, and that is their speed.

3.3. Detector Speed

The previous discussion on quantifying detector performance has emphasised the importance of the flatness of the detector, specifically in relation in structural studies. However, as the STEM is a scanning instrument it is subject to time-varying sources of noise, and naturally we should be concerned about the speed of our detectors. In the following sections, the discussion on detector performance is extended to encompass detector speeds, beginning by looking at the single electron signal.

3.3.1. The Single Electron Response

Although this topic was partially introduced in **Section 2.1.1**, some details are reproduced here for ease of reading. In a scintillator-PMT based detector, while the scintillator may have a response time of only 25 ns, when combined with a PMT and readout electronics, decay times of greater than 1 μs are regularly seen [98]. While this is generally true, it will be seen that the electron response can vary quite widely depending on the detector used. A way to understand the response of these detectors, and also their speeds, is to capture their response to a single electron.

An oscilloscope can be used to capture the signal corresponding to a single electron impact, but this requires a low enough number of electrons hitting the detector. This is shown in **Figure 2.3** where, at higher electron beam currents, single electron impacts are not visible in the detector output. Depending on the microscope there are various ways to achieve this condition. For a STEM equipped with a cold field-emission-gun (FEG), the extraction voltage can simply be lowered to reduce the dose. If a monochromator is equipped, the energy range of electrons which can pass can be reduced. In the specific case of ADF detectors, moving the electron beam to

a lower scattering region of the sample (either thin or low mass) will also reduce the number of electrons hitting the detector. Finally, reducing the camera length such that most electrons pass through the central hole of the detector is simple option. A final step may be to adjust the brightness and gain of the detector to maximise the bit depth.

Following any approach, or combination of approaches, above, the number of the electrons reaching the detector should be lowered sufficiently. Where the data are accessed also depends on the configuration of the microscope. It may be possible to stream directly from the detector, or at the input of a scan controller if one is connected to the microscope. Using a variety of the above methods, multiple oscilloscope traces corresponding to single electron impacts were captured, with the results shown in **Figure 3.4**.

A collection of experimentally captured pulses due to single electrons are presented in this image. Of the six detectors shown, the bottom five use a scintillator-PMT combination, while the topmost is a solid-state, silicon detector. The duration of these pulses range from approximately 200 ns, to 1.5 μs. Of note in this figure is not only the difference in duration of the pulses, but also shape. The shapes of these pulses can be broadly separated into two categories; symmetric, or a combination of a sharp rising edge follow by an exponential decay. While the latter may be more naturally understood as arising through the electron-detector interaction, the former is perhaps due to the use of shaping amplifiers. Such amplifiers are often used where preserving the area under a pulse is important, such as in spectrometers, where this area can be related to energy [116].

When considering the symmetric pulse shape, both the rise and decay times of the pulse are relevant parameters when evaluating both the likelihood, and severity, of

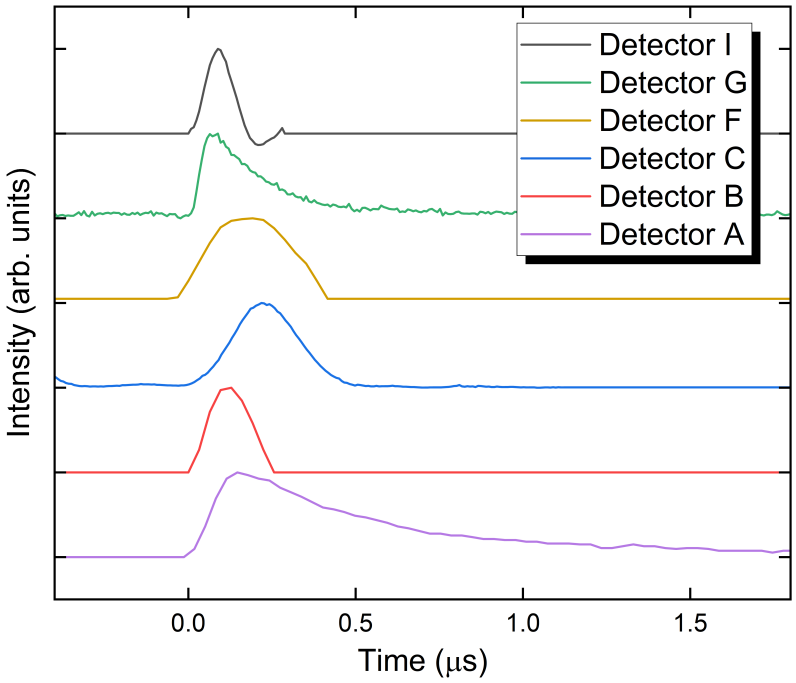

Figure 3.4.: Experimentally captured single electron impacts from six STEM ADF detectors. While the intensity of a pulse varies with the detector gain and inhomogeneity, their intensities here have been normalised for comparative purposes. Due to how some pulses were extracted from their data streams they may appear to have artificially flat background. Image adapted from [102].

signal streaking. They are also relevant parameters when considering when coincidence loss due to pulse overlap will occur. For the shape which shows an exponential decay, the decay time is significantly larger than the rise time and contributes far more significantly to signal streaking. The rise time is significant for another reason, and this is digitisation. As the digitisation approach described in this thesis relies on applying a threshold to the gradient of the detector output, a shorter rise time results in a sharper peak in the gradient, making thresholding easier. For easier visualisation of the rise and decay times, these are plotted in **Figure 3.5**.

In this figure the rise and decay times of a range of pulses are shown. All pulses bar one (F^*), are shown in **Figure 3.4**. F^* corresponds to the same detector as

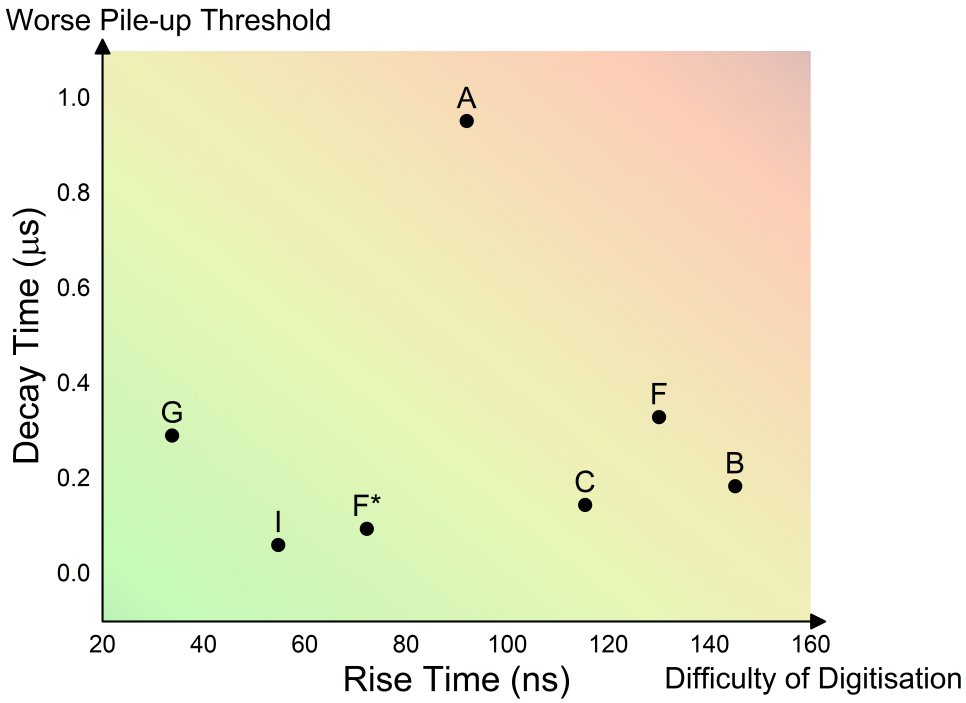

Figure 3.5.: Typical values for the 10 - 90 % rise times and decay times of the pulses shown in **Figure 3.4**. The nearer a data point is to the y-axis, the easier it will be to digitise, while the further a data point is from the origin, the more severe signal streaking will be. Image adapted from [102].

F, but captured at the detector output instead of the scan generator input. This difference in size may be a result of poor impedance matching, the main reason for inclusion here is to ensure precise reporting of detector responses.

One important point to note in this figure is the placement of detector A. If one were to judge the performance of detector A based solely on the metrics in **Figure 3.3** it appears to be one of the overall best detectors. However, when speed is taken into account we see that it has a significantly longer decay time than any other detector, leading to severe streaking. Should one be interested in high-speed imaging, this detector is in fact the least suitable, and *not* one of the best performing.

The previous sections have demonstrated the need to consider detector perfor-

mance beyond the existing metrics of flatness, roundness, smoothness, and ellipticity, and to also consider the speed of the detector used. To further this point, the next section focuses on adding streaking to simulated images so that its effects can be isolated, and understood in greater detail.

3.4. Simulating Signal Streaking

The further quantify the effects of signal streaking, its impact needs be isolated from other imaging artefacts which arise in experimental conditions. To do so we must turn to simulation. From the previous sections we have gained a substantial amount of information on detector's responses to single electrons, so the task is to incorporate this into simulations.

3.4.1. Computational Methods

The software used in this thesis to produce a simulation which streaking is added to is Prismatic [117]. Prismatic is a capable STEM simulation software, which can use either the conventional multislice algorithm, or its own plane-wave reciprocal-space interpolated scattering-matrix (PRISM) algorithm, which offers shorter simulation times. However, the main reason for choosing this software package is that the images it produces have pixel values corresponding to the fraction of the beam scattered to the detector during the pixels' dwell time.

Using one of these images as the input to our own script, the first step is converting the fractional pixel values to a number of electrons scattered to the detector for a given beam current. Now knowing the number of electron impacts per pixel, timestamps are generated for each using a Poisson distribution [67]. The chosen

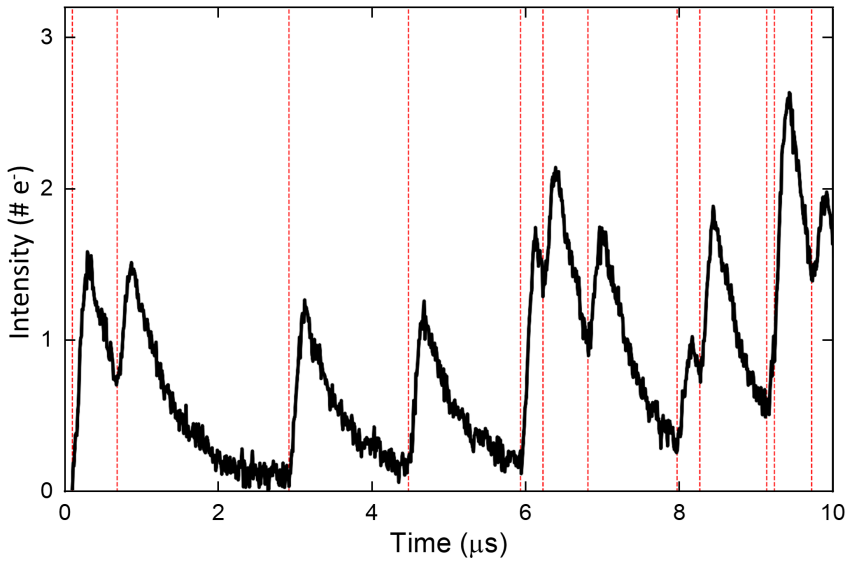

Figure 3.6.: Simulated output of a detector before it has been reshaped into an image. Dashed-red lines are the generated timestamps, with a pulse is assigned to each. The pulses have Gaussian distributed intensities, and Gaussian noise has been added to the signal.

detector's response to a single electron impact is then assigned to each timestamp, with the responses corresponding to those shown in **Figure 3.4**. Some pulses in this figure have artificially flat backgrounds due to how they were extracted from their data streams. This was found to cause issues due to abrupt changes in their intensities due to this flat background, and so are smoothed with a small Gaussian blur where necessary to eliminate this.

To account for detector inhomogeneity, the pulses are assigned with Gaussian distributed intensities. At this point a data stream has been simulated (as shown in **Figure 3.6**), but not an image. Due to past experience converting data streams to images with the first iteration of the digitisation equipment, this is handled in the same way. An appropriate number of data points are integrated to form pixels, and these pixels are reshaped into lines and then images. The code also adds line

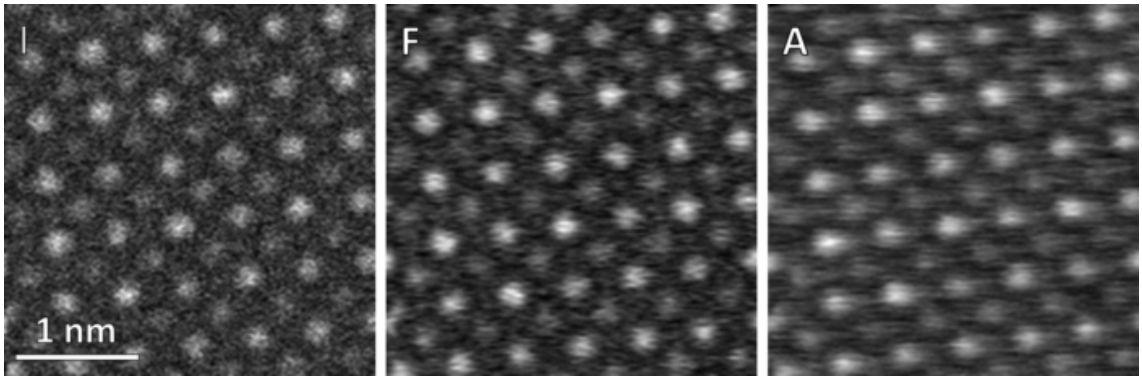

Figure 3.7.: Signal streaking as it would appear for an image of strontium titanate (STO) at consistent imaging settings for three different detectors using a dwell time of 100 ns and a 20 pA beam current. The detectors are labelled with their corresponding letters in the top left corner of each image. As the pulse duration increases, from approximately 100 ns to over 1 μs, the streaking becomes significantly more severe. The images are 200 $\times$ 200 pixels in size.

flyback time as it was found that the final pixel of one line would streak into the first pixel of the next if this was not added. With this script, streaking was added to simulations for a range of imaging settings, and for three different detectors.

3.4.2. Visual Streaking Results

High-Magnification Image

Detectors A, F, and I were chosen as this allows for comparison between two scintillator-PMT detectors with different pulse shapes and durations, and one solid-state detector. The first comparison presented is for fixed imaging conditions of a dwell time of 100 ns, and a beam current of 20 pA. The simulation to which streaking is added is one of STO, with the results shown in **Figure 3.7**.

As is evident in these images, as detector speed decreases, the severity of streaking increases. The three pulses chosen for these images have overall durations of

approximately 100 ns (I), 500 ns (F), and 1 μs (A). For the case of detector I, the pulse duration is approximately equal to the dwell time, and so while streaking is occurring, it is not severe and not obvious in this image, although it will be shown later that it is still having an effect. For the other two detectors which have pulse durations far longer than the dwell time, streaking is very apparent. With faster detector speeds, or even when considering digitised imaged which effectively have a zero-response time, images can often *look* noisier. This effect is attributed to the presence of signal streaking acting similarly to a Gaussian blur on an image, smoothing it.

One other potential effect of signal streaking is that an operator unaware of its effects may try to eliminate it by, for example, changing the astigmatism. While this may appear to somewhat remedy the effect, this is improper microscope operation, limiting the resolution of the image. As signal streaking is a temporal effect it does not only affect high-magnification images as in **Figure 3.7**. To demonstrate this, the above process is repeated for a low magnification images.

Low-Magnification Image

An example suitable samples to demonstrate signal streaking at low magnifications are biological tissues, as they contain features in the micrometre scale. However, simulating such an image can be complicated, and as only a qualitative, visual comparison is being produced here, as shortcut is taken. A TEM image of an appropriate sample is captured, cropped and has its pixel values updated to be fractions between zero and one. This is now suitable as an input to the signal streaking script, and the same process to add signal streaking is followed, producing **Figure 3.8**.

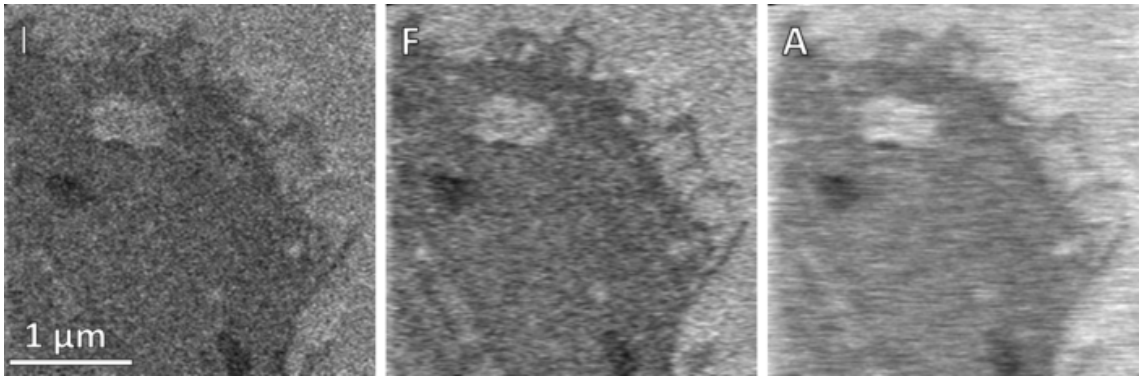

Figure 3.8.: Simulated signal streaking added to an image of a human monocyte derived macrophage cell at it would appear on three different STEM detectors. As detector speed decreases, the severity of signal streaking increases. The images are 200×200 pixels in size.

In this figure, the same results for the high-resolution image are again seen. As the duration of the simulated pulse increases, the appearance of streaking in the image becomes more significant, making it far more difficult to interpret. Having demonstrated visual comparisons between the effects of having different speed detectors, we now turn to observing the effects of streaking through use of the Fourier transform.

3.5. Signal Streaking and the Fourier Transform

While visual analysis and making direct measurements from an image are often suitable, there is a very important approach to image analysis which has yet to be mentioned: the Fourier transform (FT). In this section, the significance of the FT and how it can be used to describe signal streaking is explored.

3.5.1. The Fourier Transform

The FT is a powerful tool which, in essence, transforms an image containing information in the spatial domain to one containing the same information in the reciprocal domain. In this domain we learn of the spatial frequencies which are present in the image, and their amplitudes. This is of particular use when analysing atomic resolution images, as their inherently periodic structures give rise to obvious peaks in amplitudes in the FT. The specific algorithm used to calculate the FT is the Fast Fourier transform (FFT). Although initially described in an unpublished work by Gauss in 1805, it was rediscovered and made popular by Cooley and Tukey in 1965 [118, 119].

A simple example of how the FFT may be used is checking if a certain resolution in the image has been achieved by looking for the presence of a particular spot in the FFT. Spots closer to the centre of the FFT are caused by lower frequency information in the image, such as a pattern which sinusoidally varies a small number of times across the image. Spots further from the centre represent information which has a higher spatial frequency, varying a greater number of times across the image. The FFT of an image also corresponds to the diffraction pattern of said image, which can be quickly viewed at the microscope for such resolution checks, or other reasons such as tilting the crystal to a certain zone axis.

Although spots are often what are looked at in the FFT, there is more we can learn by looking at the background, especially with relation to signal streaking. As signal streaking typically occurs in across a small number of pixels, it degrades information of this size in the image, that is, higher spatial frequency information. Signal streaking therefore produces an envelope function in the FFT which decreases

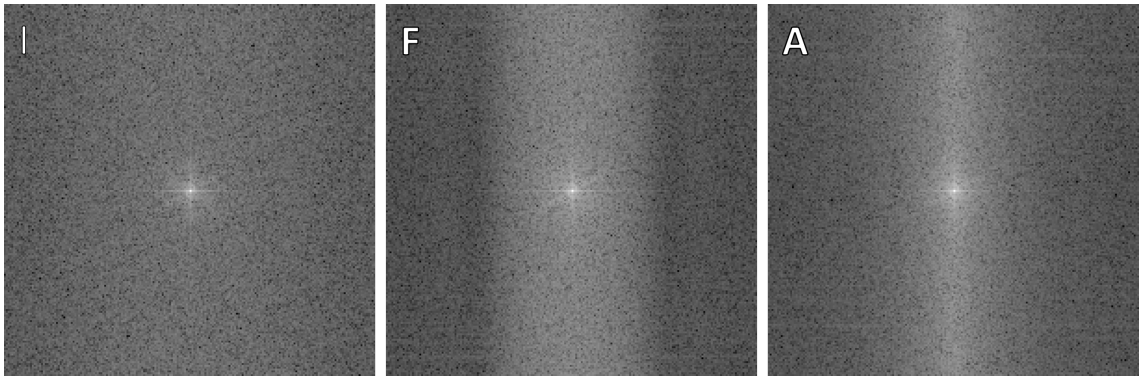

Figure 3.9.: Fourier transforms of the three images in **Figure 3.8**, which are formed from the same original image, but with signal streaking added as it would appear for three difference detectors. The detector speed decreases when moving from left to right, and this corresponds to a visible drop in the background intensity of the Fourier transforms.

towards the edges, and this is what is studied in the following section.

3.5.2. Behaviour of the Fourier Transform

To begin, the behaviour of the FT in the presence of streaking across three different detectors is investigated. To show do, the FFTs of the three images with streaking added in **Figure 3.8** are calculated, with the results shown in **Figure 3.9**.

In this figure we see the an obvious drop in intensity as the response speed of the detector decreases. This can be understood as previously described. With slower detector response, signal streaking becomes more severe and spreads to more pixels. When one or two neighbouring pixels are affected, high spatial resolution information in the image is lost, and intensity in the fast scanning direction far from the centre of the FFT decreases. With even more severe streaking, lower resolution information also begins to become affected, and intensity closer to the centre begins to decrease also.

Both of these trends are visually apparent in the figure. As the streaking here is simulated and the underlying image is the exact same in each case, it can be assumed that this envelope arises only from signal streaking. It has also been shown here that although the original image does not contain any particularly small features, information is still being lost due to the signal streaking.

For further evidence that signal streaking causes this drop in intensity, a series of experimental images with increasingly shorter dwell times is captured, with the results shown in **Figure 3.10**.

In **Figure 3.10**, four experimental images of STO are shown for decreasing dwell time with their corresponding FFTs. Although decreasing the dwell time decreases the electron dose, the number of image frames captured at faster speeds is increased such that each final image has the same signal level. Consequently, the only difference between the images is the dwell time they were captured at. Each FFT in this figure is overlaid with an intensity profile has formed from the bottom region of each FFT which was then fitted with a Gaussian.

The detector used to capture these images has a response time of approximately 200 ns. Hence, when imaging at 1 μs, no drop in intensity is seen as there is likely very little signal streaking. Upon decreasing the dwell time to 200 ns, even though streaking is not apparent in the image, it can be seen in the FFT that information is being lost. At 100 ns although there is some difference in the image, appearing almost as a change in focus, the more obvious change is in the FFT where the drop in intensity becomes more severe. Finally, at a dwell time of 50 ns, where signal streaking is now unavoidable and affecting multiple subsequent pixels, the effects in both the image and FFT are obvious. The image is heavily blurred, and the drop in intensity in the FFT is so great and near to the centre, that it has even resulted

in some diffraction spots being no longer visible.

The drop in intensity observed in these FFTs is similar to the behaviour seen in in **Figure 3.9**, however in this case the detector speed is fixed. Therefore, the signal streaking is becoming more severe due to decreasing dwell time, and not increasing detector response time. This shows that when signal streaking becomes more severe, regardless of the cause, this intensity profile occurs in the FFT.

In both these scenarios the images were experimental, with either experimental signal streaking or simulated signal streaking. To ensure that this behaviour is due to signal streaking, a purely simulation based example is made, shown in **Figure 3.11**.

In this figure, the STO images are simulated to match the imaging conditions of **Figure 3.10**. Very similar behaviour is observed in both the images and the FFTs. As the dwell time increases, signal streaking becomes less apparent in the images, and the intensity falloff in the FFT decreases. At a 50 ns dwell time some spots in the FFT are no longer seen due to signal streaking, and the image is visually blurred. The intensity profiles are not an exact match, but are very similar, perhaps due to some sources of noise which are present in the experimental images being absent in the simulations.

From this series of examples and experiments it can be concluded that whether scanning at faster speeds or with a slower detector, a drop in background intensity of the FFT in the fast scanning direction is seen. This is caused solely by signal streaking, and information is being lost even if not necessarily visible in the image.

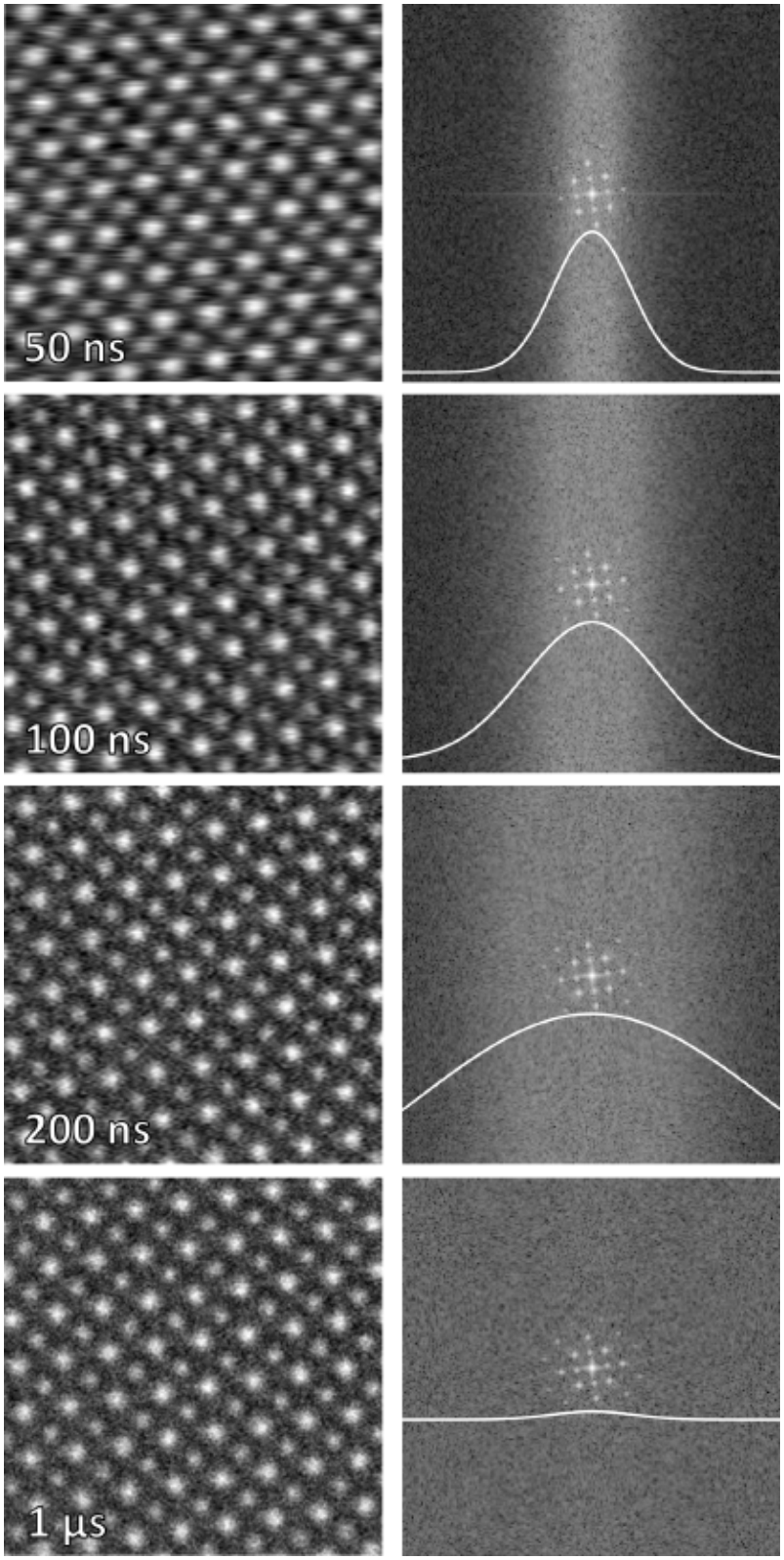

Figure 3.10: Experimental images of STO captured on a Nion UltraSTEM 200 with increasing dwell times. Each image is 200 × 200 pixels in size, and has a FOV of 4 nm. Beside each image is its FFT, overlaid with an intensity profile formed by fitting a Gaussian to the sum of bottom region of each FFT. As the dwell time increases, streaking becomes less severe, and the drop in the background intensity of the FFT at higher spatial frequencies decreases.

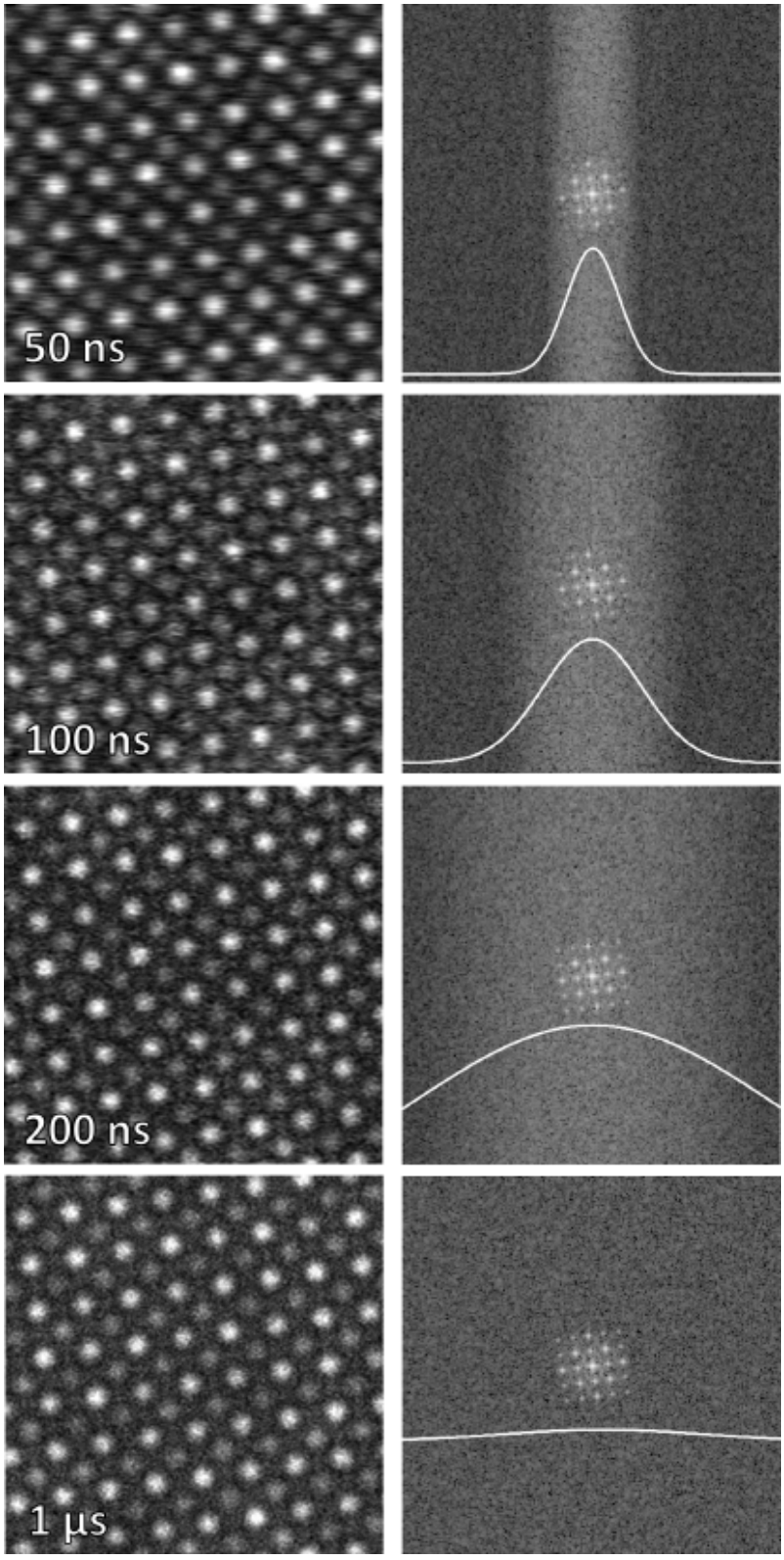

Figure 3.11: Simulated signal streaking added to an image of STO, matching the conditions of **Figure 3.10**. The same behaviour is seen: as the dwell time increases, the intensity envelope seen in the FFT drops off more slowly.

3.6. The Temporal Transfer Function

In the previous section, the ability to add signal streaking to images was used to isolate the effects of signal streaking and confirm how it degrades images and their Fourier transforms. One further possibility to explore using this ability is to determine a relationship between the intensity profile in the FFT of an image with signal streaking and the response of the detector.

If considering signal streaking as acting as the point-spread function (PSF) of the STEM, then it follows from this that the Fourier transform of the PSF is the optical transfer function (OTF) [120]. For detector A, with a sharp rising edge and an exponential decay, the equations describing these parameters are as follows.

$$PSF(t) = \begin{cases} 0, & \text{if x} < 0 \\ I_0\, e^{-t/(\nu\cdot\tau)}, & \text{otherwise} \end{cases} \tag{3.1}$$

$$OTF(f) \propto \frac{1}{1 + 2\pi i\tau\nu f}. \tag{3.2}$$

Where ν is the sampling rate (equivalent to the dwell time for a STEM image), and τ is the decay time of the pulse. The OTF can be further separated into its real and imaginary components, the modulation transfer function (MTF) and phase transfer function (PTF) respectively, with these stated below:

$$MTF(f) \propto \frac{1}{\sqrt{1 + (2\pi\nu\tau f)^2}} \tag{3.3}$$

$$PTF(f) \propto arctan(-2\pi\nu\tau f). \tag{3.4}$$

The MTF is often measured and used to evaluate the performance of an imaging

system. This is done by taking the Fourier transform of an image of, for example, a knife-edge feature. However, in the case of detector A where the PSF is asymmetric, one must also consider the PTF, as considering only the MTF will not capture all necessary information.

One important point about these equations is that they depend directly on τ, a feature of the detector used. Hence, it may be possible to measure the decay time of the detector from the Fourier transform of an image using the intensify profiles previously shown. As it is also possible to measure the director response directly, as in **Figure 3.4**, these results could be verified. It should be noted that more than a single decay time is associated with a detector, such as the previously discussed longer afterglow, where more equations will be required when incorporating afterglow.

Similar treatment can be performed for detectors with a symmetric response. In this case, assuming a Gaussian pulse shape, the Fourier transform of a Gaussian is another Gaussian, where the width of one varies inversely with the width of the other. This corresponds to behaviour expected to be seen; as the width of a pulse increases (and streaking becomes more severe), the width of the intensity envelope in the Fourier transform decreases.

Work into this is ongoing, with the goal being to define the Temporal Transfer function, a metric with which to evaluate STEM detector performance, analogous to the MTF for TEM cameras.

3.7. Conclusions

In this chapter, the effects of signal streaking on detector maps was discussed. Detector mapping is an important technique which evaluates detector performance, whether to gain a better understanding, or to incorporate the performance into simulations. Parameters such as flatness, roundness, smoothness, and ellipticity are often evaluated, with the first three of these directly dependant on the single electron response.

As digitisation changes the single electron response to a perfectly localised, single-intensity digital '1', it dramatically improves these three parameters. Upon digitisation, the average flatness, roundness, and smoothness deviations of eight studied detectors from an ideal detector decreased by 6.78 %, 9.97 %, and 32.06 % respectively. This brings these detectors far closer to those used in simulations, and also increases image quality.

A further aspect of detector performance not covered under this discussion is that of detector speed. Using an oscilloscope, traces corresponding to single electron impacts were captured from eight different detectors. These pulses ranged $\sim$200 ns to over 1.5 μs in duration, and had either symmetric shapes, or an exponential rising edge followed by a decaying edge. The relevance of this is highlighted as one detector which displayed impressive performance for the previous metrics seemed like the best overall choice of detector, yet had the slowest response, making it in fact the least suitable for high-speed imaging.

To isolate the effects of signal streaking on images, code was written to allow signal streaking to be added to simulated images as it would appear for a range of detectors. First, streaking was added to one image of STO as it would appear

for three detectors, encompassing the full range of response times measured. As the speed of the detector decreased, streaking became noticeably more severe in the image. This was repeated for an image of a biological tissue, showing that even an image without particularly small features is affected by signal streaking.

Next, the effects of signal streaking on the Fourier transform was analysed. It was shown for the streaked images of the biological tissue, a loss of information in the fast scan direction of the Fourier transform was visible, increasing in severity as detector speed decreased. Then, a series of experimental images of STO was captured, with dwell times decreasing from 1 μs to 50 ns for a fixed detector response. As the dwell time decreased, signal streaking increased, and this same behaviour was observed in the Fourier transform, resulting in the loss of diffraction spots at a dwell time of 50 ns. Finally, to confirm the origin of this drop in intensity in the Fourier transform is caused by signal streaking, a simulated of image of STO, matching the previous imaging parameters, had signal streaking added to it for the same dwell times. The same behaviours are seen in both the images and Fourier transforms, confirming signal streaking as the origin of this effect.

The route to a future goal of this research, defining the Temporal transfer function for STEM detectors, was discussed, which may be a new metric with which to evaluate detector performance. While the previous chapters have been focused on the efficient detection of electrons, the following chapter instead looks at the efficiency of the scans we are using.

Chapter 4.

Increasing Scanning Efficiency via Flyback Hysteresis Correction

The previous chapters explained how using low beam-currents, fast scanning speeds, and multi-frame imaging is the most available approach to low-dose STEM imaging, which is becoming a requirement for a wide range of materials. While these imaging conditions lead to signal-streaking and worsens the effects of detector afterglow, digitisation was introduced as a solution to these through efficient electron detection.

However, one aspect not explored is that this same combination of imaging settings often leads to very low-efficiency scans, regrettably working counter to the initial motivation of low-dose imaging. This happens as when the scanning speed increases, the fixed line-flyback time becomes a larger fraction of the time spent imaging a sample, damaging it while returning no useful information. While the flyback time can be decreased, hysteresis in the magnetic lenses leads to unacceptably distorted images, and so a solution is needed. The method by which this distortion is corrected for and the effect this has on imaging efficiency is discussed in this chapter.

4.1. Scanning Efficiency

When the electron dose was previously introduced, only dose delivered during the dwell time of a single pixel was considered, with the equation reintroduced here.

$$Dose = \frac{I \cdot C \cdot \delta_{\mathrm{t}}}{dx^2} \cdot F \qquad \text{(1.3 revisited)}$$

Where I is the electron beam current used, C is Coulomb's number, δ_t is the dwell-time, dx^2 is the area of the pixels, and F is the fraction of pixels illuminated if using a method such as compressed sensing. However, we need to consider the electron dose delivered during the line flyback time (T_{LFB}) and the frame flyback time (T_{FFB}) to fully understand the electron-dose delivered. This is increasingly relevant as shorter dwell-times are used, as a larger fraction of each scan line is now spent during the line flyback time, with this graphically represented in **Figure 4.1**.

Furthermore, when the SNR of each frame is lower, multiframe imaging becomes necessary. While one might assume that 20 image frames at a low dwell-time results in the same electron-dose exposure as a single frame with twenty times longer dwell-time, due to T_{LFB} and T_{FFB} this is not the case. Clearly, an updated equation is required to reflect this, with one incorporating these terms included below.

$$Dose = I \cdot C \cdot (\delta_{\mathrm{t}} \cdot n_{\mathrm{p}} + (T_{\mathrm{LFB}} \cdot n_{\mathrm{L}}) + T_{\mathrm{FFB}}) \cdot \frac{1}{dx^2 \cdot n_{\mathrm{p}}} \cdot F \qquad (4.1)$$

Where n_{p} and n_{L} are the number of pixels and lines in an image respectively. **Equation 4.1** can be understood as containing three terms. The first converts the beam current in Amps to electrons per second, the second term represents the

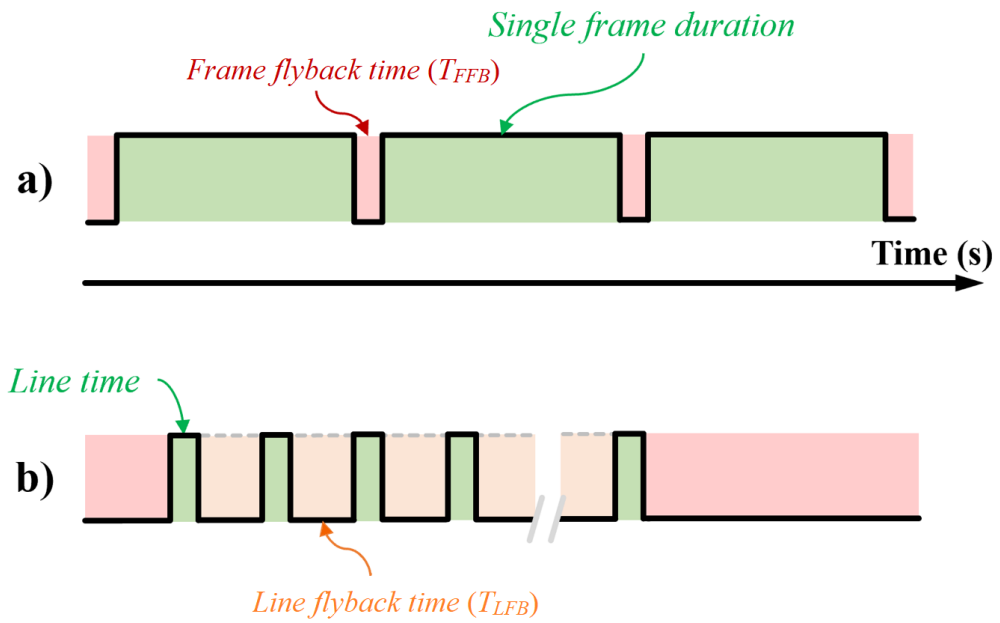

Figure 4.1.: Schematic of the constituent times which comprise a full STEM image. **a)** shows an illustration of a series of three successive image frames. **b)** shows an expanded illustration of the individual scan-lines within a single frame. Useful sample exposure is illustrated in green, line flyback time is in orange, and frame flyback time is in red. Image from [121].

duration of a full frame, including both T_{LFB} and T_{FFB}, and the third term calculates the area scanned. The path that the electron beam travels during the flyback times varies depending on the microscope, and can be outside of the region shown to the user. In this case, the area scanned is slightly larger than that calculated in **Equation 4.1**, however this is a minor difference, and for damage processes caused by secondary electrons this electron-beam exposure is still relevant. As the first version of the digitisation equipment continuously streamed data, this allowed for the opportunity to view the path that the electron beam takes during the line flyback time, with this shown in **Figure 4.2**.

In **Figure 4.2**, the path the beam takes during the line flyback time is shown on

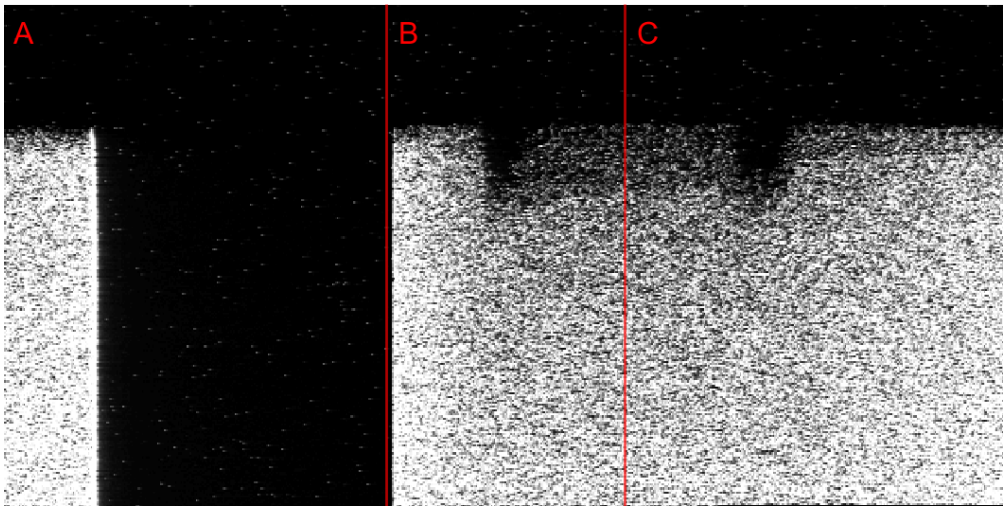

Figure 4.2.: Low magnification image of a lamella divided into three sections. Whereas data captured during the line flyback time is normally cropped from the user's view, it is included here. **A**: The image normally shown to the user. **B**: Data captured while the beam is travelling from the right side of the image to the left. The electron beam overshoots the left of the original image, evidenced by the presence of a feature which is not seem in region **A**. **C**: Data from this region is captured while the beam is again travelling to the right after overshooting. Image from [1].

a FEI Titan G2 80-300 kV controlled with the OEM scan generator. During the line flyback time in this image, a feature which is not present in the original image is viewable, implying the beam overshoots the first pixel of the next line during the flyback time. Although it is difficult to directly interpret this image as the beam is not travelling at a constant velocity and so distortions are present, it is still evidence that the beam travels across the sample again, and damages a region outside the usual image shown to the user.

Having derived both an equation for calculating the electron dose which returns useful information (**Equation 1.3**), corresponding to the region labelled **A** in **Figure 4.2**, and the total electron exposure (**Equation 4.1**), corresponding to the entirety of **Figure 4.2**, dividing the first by the latter derives an expression for the scanning efficiency, η.

$$\eta = \frac{\delta_{\mathrm{t}} \cdot n_{\mathrm{p}}}{(\delta_{\mathrm{t}} \cdot n_{\mathrm{p}}) + (T_{\mathrm{LFB}} \cdot n_{\mathrm{L}}) + T_{\mathrm{FFB}}} \tag{4.2}$$

η can be intuitively understood as the ratio of the useful, information collecting time, to the total time spent capturing an image, and always has a value less than one. As an example calculation, for a square image of 512 pixels captured using a dwell-time of 2 μs, a line flyback time of 400 μs, and frame flyback time of 0.25 s, the efficiency is approximately 50 %. This means one in every two electrons damages the sample in return for no useful information, and also highlights the inaccuracy of **Equation 1.3**.

To increase this scanning efficiency one could: increase δ_{t} and n_{p}, or decrease n_{L}, T_{LFB}, and T_{FFB}. However, from **Equation 4.1** we can see that the first three of these options would in fact raise the electron-dose, counter to the aim of low-dose

imaging. This leaves reducing the flyback times as the route available to increase the scanning efficiency while also decreasing the dose. One other approach which is now available is to blank the electron beam during the line flyback time, using a solution such as the EDS True Area Scan by IDES inc. [122]. By doing so, any unnecessary electron exposure, and therefore damage, is eliminated, but without the same framerate improvements.

4.2. Reducing Flyback Times

To first show the importance of reducing the flyback times, **Equation 4.2** is evaluated for dwell-times ranging from 50 ns to 38 μs for an image of 512 x 512 pixels. These speeds range from the fastest dwell-time possible with modern scan generators such as a DigiScan 3 or point electronic DISS 6, to the speeds achieved when line-syncing to 50 Hz main frequency. The largest line flyback time evaluated is 1000 μs, above which it will rarely be set, with more typical numbers seen being in the hundreds of microseconds. Finally, the frame flyback time is taken to be 0.25 s, timed empirically on a Nion UltraSTEM 200 controlled by a DigiScan II, with the results shown in **Figure 4.3**.

It can be seen in **Figure 4.3** that scanning efficiency is very high regardless of the line flyback time at longer dwell times. If not multiframe imaging and instead capturing a single, long-exposure image, these are often the conditions used. As this is still a reasonably commonplace approach, it is perhaps unsurprising that the extra dose delivered during the flyback time has not received a lot of attention to date.

Another reason for this is the use of line-synced captures, at either 60 Hz or 50

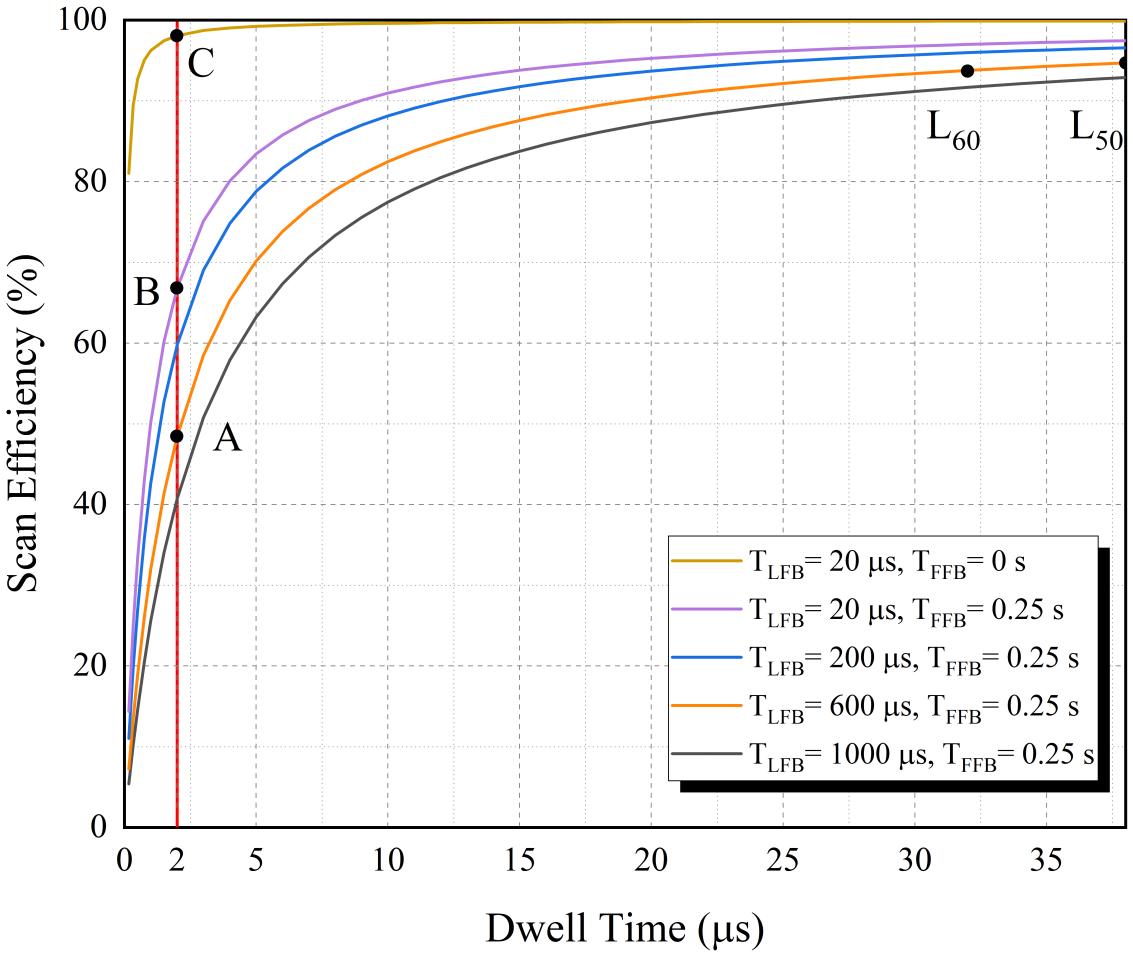

Figure 4.3.: Plots of the scanning efficiency, η, as a function of dwell-time for varying line flyback times and a frame flyback time of 0.25 s. The uppermost line evaluates η for a frame flyback time of 0 s. The points L_{60} and L_{50} are the efficiency of line-synced scans at 60 and 50 Hz respectively for a line flyback time of 600 μs. As the dwell time decreases, so too does the η. Image from [121].

Hz, as marked by the points L_{60} and L_{50} in the figure respectively. Line syncing is when the start of each line in the image is synchronised with the phase of the AC power supply, always starting at the same point of a cycle, in order to minimise disturbances at this main's frequency. When using a DigiScan this is achieved by increasing the dwell-time to meet this condition, explaining the positions of these points on the graph.

However, when using shorter dwell times, large jumps in efficiency are seen when the line flyback time is lowered. For example, when using a 2 μs dwell time, the efficiency increases from below 50 % to nearly 70 % when the line flyback time is decreased from 600 μs to 20 μs, with these values labelled as points **A** and **B** respectively. While not an insignificant increase, reaching even higher efficiency values requires eliminating the frame flyback time. This is shown by point **C** with an efficiency greater than 95 %, which has the same imaging settings as point **B** except that the frame flyback time has been eliminated. Regrettably, the frame flyback time can often not be reduced as this time is often reserved for saving data, leaving the line flyback time as the variable to change. While reducing the line flyback is generally readily available, doing so leads to a compression artefact, explained in the following section.

4.3. Scan Coil Hysteresis

The scan-coils which control the electron beam are electromagnets of finite inductance, and therefore there is a non-zero response time between current changes in the coils and changes in the driving voltage [90]. This leads to a lag between the intended position of the electron beam and its actual position, until the beam reaches

a constant velocity, analogous to inertia in a physical system [85].

As shown in **Figure 4.2**, the path the beam takes during the flyback time involves overshooting the first pixel of the next line before reversing position and returning to the first pixel. If the flyback time is long, then the electron beam has enough time to reach a constant velocity before it reaches the first pixel. However, at short flyback times the beam is still lagging behind its intended position when the scan-line begins due to hysteresis, resulting in a larger than intended area of the sample being imaged. Fitting this extra area into the correct number of pixels means that the image appears compressed, specifically at the start of each line, corresponding to the left side of an image. While the exact path of the beam varies by instrument and scan controller, such a compression artefact has been observed on many microscopes, both in literature, and with two examples shown in **Figure 4.4**.

It has been previously observed that the rise-time of the scan-coils follow an exponential shape, as expected from a system with inductance effects [73, 90]. Where the flyback time is eliminated the rise-time can be measured either directly or indirectly, with 90 % rise-time values between 10 and 100 μs having been measured [90, 88]. Where longer dwell times are used this compression artefact may affect only a small number of pixels at the start of each image line. However, at shorter dwell times, which are the times of interest here, this artefact is readily seen and can affect more than half of the image [73, 99]. However, as an overly large area is sampled, the original field-of-view can be recreated via post-processing if the magnitude of this compression artefact can be measured. The process by which this is done is the topic of the following section.

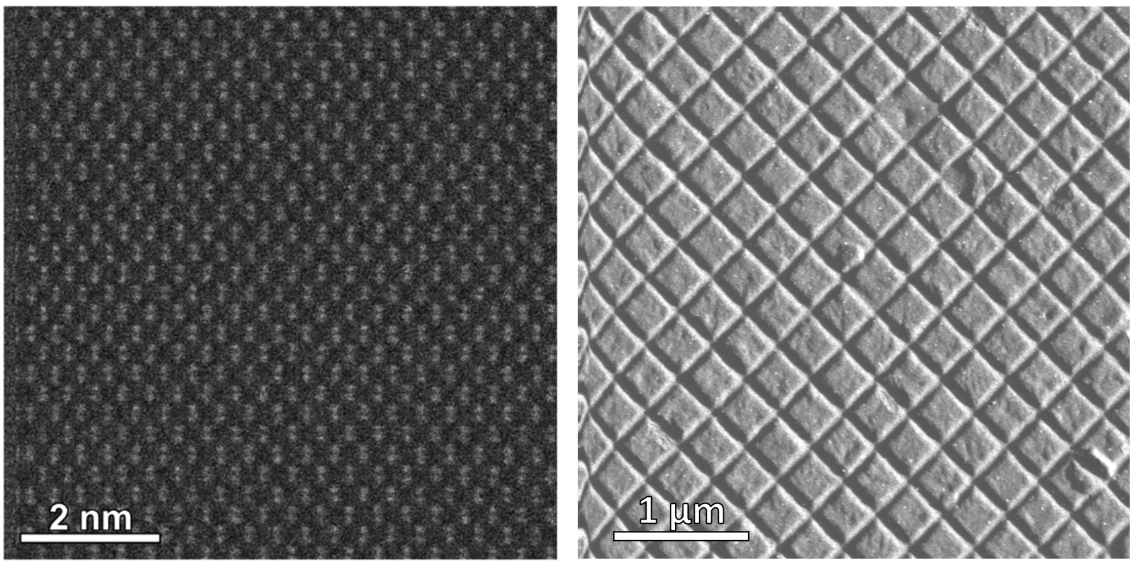

Figure 4.4.: Left: Image of a single crystal of silicon oriented in the <110> direction captured on a Nion UltraSTEM 200 with a dwell time of 2 μs and line flyback time of 20 μs. **Right**: Image of a standard cross grating test specimen captured on a ThermoFisher Titan G2 80-300 kV STEM at the same imaging settings. Despite the differences in these instruments, a similar compression artefact is seen in each caused by flyback hysteresis. Images adapted from [121].

4.4. Fitting the Compression Artefact

Using the knowledge that the flyback hysteresis causes a compression artefact which follows an exponential form, an equation for this distortion can be written as the function of two unknown parameters, A and b.

$$x_{\text{corrected}} = x - Ae^{-\text{t} \,/\, \text{b}} \tag{4.3}$$

In the above equation x are the measured x-positions, and by calculating the exponential compression and subtracting it from the x, the true positions, $x_{\text{corrected}}$, can be restored via bilinear interpolation. By working in units of time in the exponential allows the line flyback time, T_{LFB}, to be explicitly incorporated:

$$t = x \cdot \delta_{\text{t}} + T_{\text{LFB}} \tag{4.4}$$

With calculating these two desired parameters as the goal, what is needed is an approach to measure the distortion. There are many approaches used to measure image distortions when using a single-crystal reference sample such as geometric-phase analysis (GPA). Using this method, the e_{xx} term from a single-crystal inherently captures the flyback distortion [123, 124]. However, due to Fourier truncation some edge effects are present around the image in the measured distortion fields, unfortunately the region of highest interest. Furthermore, the manually selected Fourier masks, of which minimum two are required, results in a minimum of 6 adjustable parameters (the radius, x-y position, and edge-smoothing), and other systematic artefacts can be introduced [125]. Another possible, but practicably difficult and time-consuming approach, is to manually measure the position of atomic columns

or other fiducial features [73, 90].

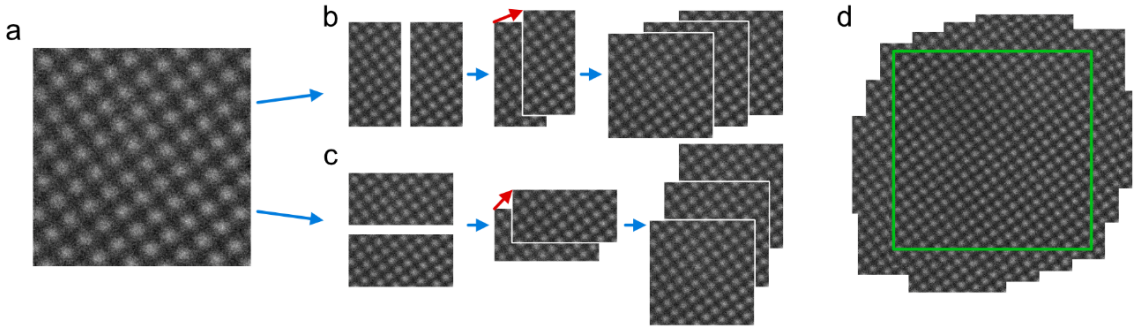

Figure 4.5.: **(a)** shows the starting undistorted image from which a reference is generated. The image is then divided horizontally, **(b)**, and vertically, **(c)**, and cross correlations are used to produce the two tiling vectors shown in red. These tiling vectors are then used to tile the image to generate an overly large area from which a suitable reference, the green box, is used as reference, **(d)**. Images adapted from [121].

An ideal approach would be one which does not intrinsically introduce any image-edge artefacts or require the manual section of certain parameters to avoid the introduction of other artefacts. The solution to these problems is to work in real-space instead of reciprocal-space, and use a readily available single-crystal reference material such as Si or $SrTiO_3$, with the fixed atomic spacing of such a material being used to optimise the parameters A and b. This can be done via non-linear least squared fitting against a distortion free reference image, also referred to as a quasi-static reference image[126, 127].

There are two ways with which such a reference image can be generated, either an image is captured with a very long line flyback time such that there is no compression artefact, or one can be generated from the right half of an image, as distortion due to flyback hysteresis is negligible in this region. The process by which this reference is generated is explained fully in **Appendix A**, but **Figure 4.5** is shown here as a general overview.

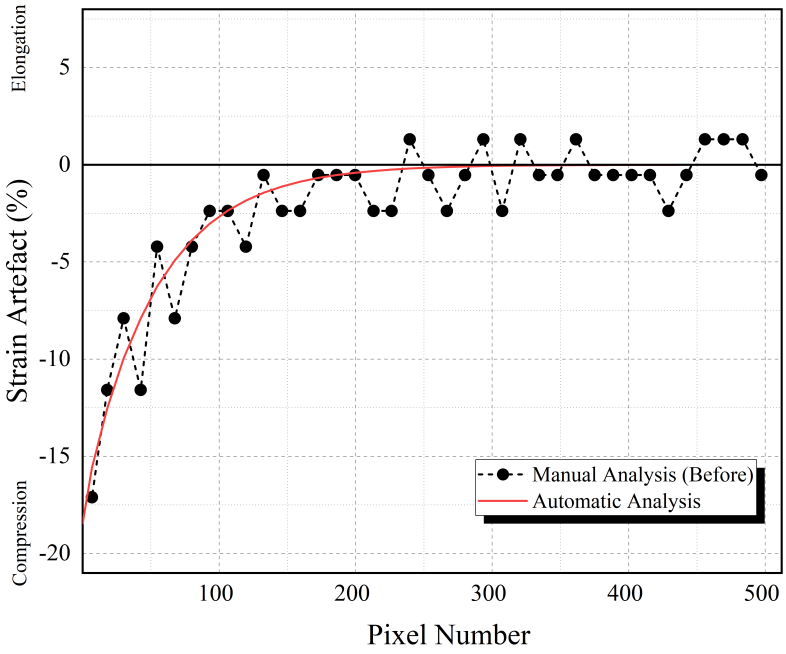

Figure 4.6.: Flyback hysteresis diagnosis for a 512 × 512 pixel wide image with a 20 μs line flyback time and a 0.5 μs dwell time. The solid red line represents the output of the automated analysis, while the black round points are measurements from the manual analysis. Image adapted from [121].

A comparison of the manual and automatic diagnoses is shown in **Figure 4.6** for an image captured with a 20 μs line flyback time and a dwell time of 0.5 μs. While both methods give nominally identical results, the requirement of human intervention and the inclusion of a small random scatter due to the finite pixelation of the peak position identification limits the precision of the manual approach. The automated approach uses a smoothly varying mesh instead of pixels, does not rely on a particular scan orientation, utilises the entire field-of-view, and requires significantly less time investment. Due to these reasons, the automated approach is chosen going forward.

The appearance of the compression artefact varies with both dwell time and line flyback time, and so this fitting process can be repeated for varying combinations

of these parameters, with the values for A and b tabulated for each. It has been observed that these parameters remain fixed for the same imaging settings at the same operating voltages, even across a timespan of weeks [121]. Knowing this, a diagnosis of the compression artefact at some combination of imaging settings can be used to correct any future, or even past images, captured at these same settings.

More useful than this however is to generalise the values for A and b, using them to generate a semi-empirical equation which can describe the behaviour of the compression artefact. This equation, expected to vary by instrument, can then be used to find values for A and b for any imaging settings to eliminate the hysteresis artefact, regardless of whether a diagnosis has been performed at these exact settings previously. In this way, flyback hysteresis correction can be treated as other instrument calibrations such as magnification, performed on a per-instrument basis during installation.

4.5. Correcting the Compression Artefact

4.5.1. Correction of a Single-orientation Series

Having explained the process by which the compression artefact is diagnosed and corrected, the first results presented here are qualitative visual comparisons of excerpts from images of STO with increasingly shorter line flyback times, both before and after correction.

While the reference used for diagnosing the flyback is formed from the right half of the image to be corrected, the 1 ms line flyback time image is used as a visual reference image for comparison with the compressed images in **Figure 4.7**. The

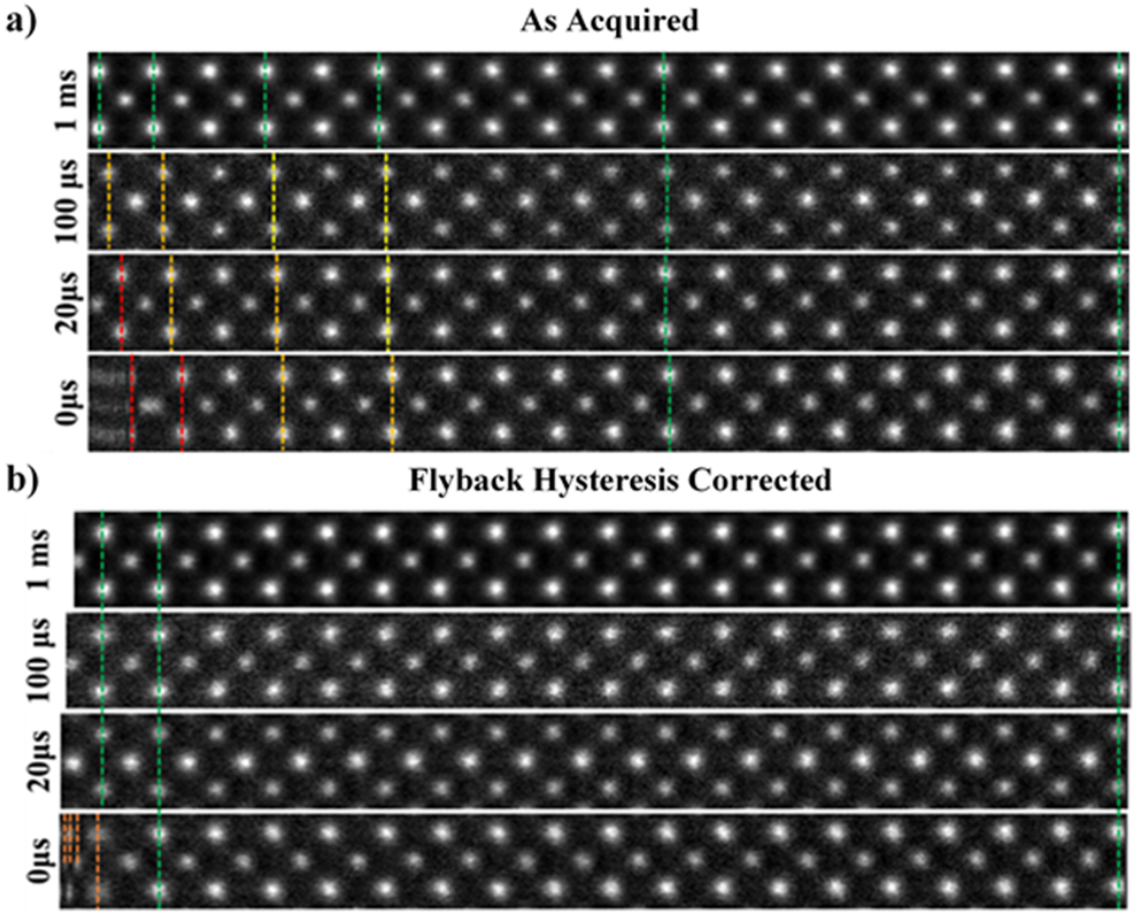

Figure 4.7.: **(a)** Montage of excerpts from images of STO captured at increasingly shorter line flyback times, as indicated on the left of the excerpts. The compression artefact becomes increasingly severe with decreasing line flyback time. **(b)** shows the same images post-correction. The compression artefact is removed for all images except for that captured with a line flyback time of 0 μs, where some artefact remains. Image from [121].

unit-cells across this long line flyback time image are uniform in width across the entire FOV. For the images captured with shorter flyback times the unit cells are uniform in width on the right half of the images as indicated by their alignment with the visual reference. However, with decreasing line flyback time the left half of the image becomes increasingly compressed. Using the method introduced here, the compression artefact in **Figure 4.7 a)** is corrected prior to any alignment, with the result shown in **Figure 4.7 b)**.

Post-correction, it can be seen that for line flyback times of 100 μs and 20 μs the unit cells are in perfect alignment with the quasi-static reference. The image captured with a line flyback of 0 μs still displays an artefact, but is still greatly improved compared to pre-correction. This artefact remains as the beam cannot achieve a 0 μs line flyback time as a finite amount of time is required. Data captured while the beam is flying back is what is being displayed in this corrupted part of the image. It can also be seen that the image width increases post-correction. This is as expected as compressed data is being "stretched" back to its original size. This method was then used to diagnose the compression for a wide range of dwell-times and line flyback times in order to diagnose the behaviour of the compression artefact.

4.5.2. Diagnosing the Hysteresis Compression Artefact

The values for A and b from **Equation 4.3** were calculated for a range of dwell time and line flyback times, with the results shown in **Figure 4.8**. Clear trends are seen in this image, and notably, use of **Equation 4.4** has removed any dependence on the line flyback time, allowing these parameters to be understood as a function of dwell time only.

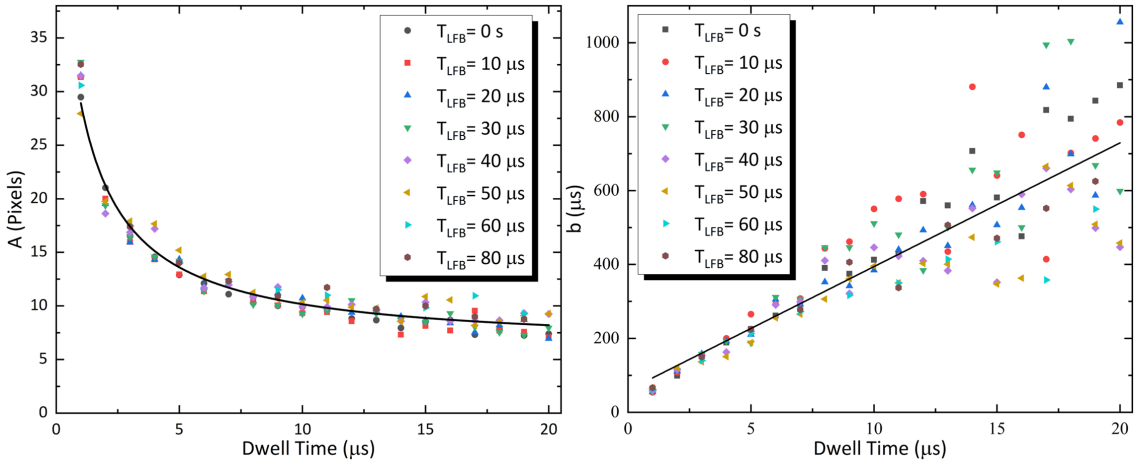

Figure 4.8.: Graphs of the calculated values for A and b from **Equation 4.3** which parametrise the compression artefact due to flyback hysteresis as a function of dwell time for varying line flyback time. Image from [121].

The parameter A shows an inverse decay relation with dwell time, while b increases linearly with dwell time. This can be naturally understood; with a longer dwell time the magnitude of the compression appears smaller, corresponding to a lower A value, and also decays faster across the image, corresponding to a larger b value. A reasonably simple set of equations (one inverse and one linear) can be used to determine all required parameters needed in **Equation 4.3**, and therefore correct the compression artefact for all line flyback and dwell time combinations. As these equations are made to not vary with the line flyback time, only a small number of images with the dwell time varying are required to diagnose the hysteresis behaviour.

While these equations are simple, generalising them to physical parameters of the scanning system is not easy as their physical origin is obscured by the manufacturer's choice of scan generator and microscope control hardware. For example, the DigiScan II diagnosed in this work produces a pure sawtooth waveform, even during the line flyback time, which modifies the coil current with a dependence on

scanning speed. To maintain generality there is no attempt to reduce the number of fit parameters further, however it is also clear that this is not required from the results shown. To verify this, an example of strain analysis before and after is shown in **Figure 4.9**.

GPA analysis was used to measure the decrease in strain after correcting the compression artefact. Silicon was used at it is known to have negligible strain, and so any measured strain is due to this compression, which is visually clear in **Figure 4.9 a**. The average strain in the left half of the image before correction was measured to be -2.420 ± 0.004 %, reducing to -0.309 ± 0.001 % after correction. Although the artefact mostly affects the left half of the image, a reduction is still observed in the right half, from 0.136 ± 0.001 % to 0.066 ± 0.001 %.

While the effectiveness of hysteresis correction has been shown for the cases presented here, some parameters have not been discussed, with one such example being magnification. Due to the limited magnification range which can be used on the microscope used for these results, a full characterisation of its effects could not be carried out. As magnification is linearly related to the current in the scan coils, it is likely that the effect of the compression within the image will also scale linearly. Therefore, fractionally, the artefact may have the same form within an image at different magnifications. However, when varying magnification across a wide range the current in the scan coils can change by an order of magnitude, and this assumption may not hold.

For those replicating this work, a case-by-case investigation on each instrument being diagnosed is recommended. Similarly, the effect of operating voltage of the electron microscope is not investigated here. As most microscopes typically operate at a small set of fixed voltages, characterising these separately is recommended. One

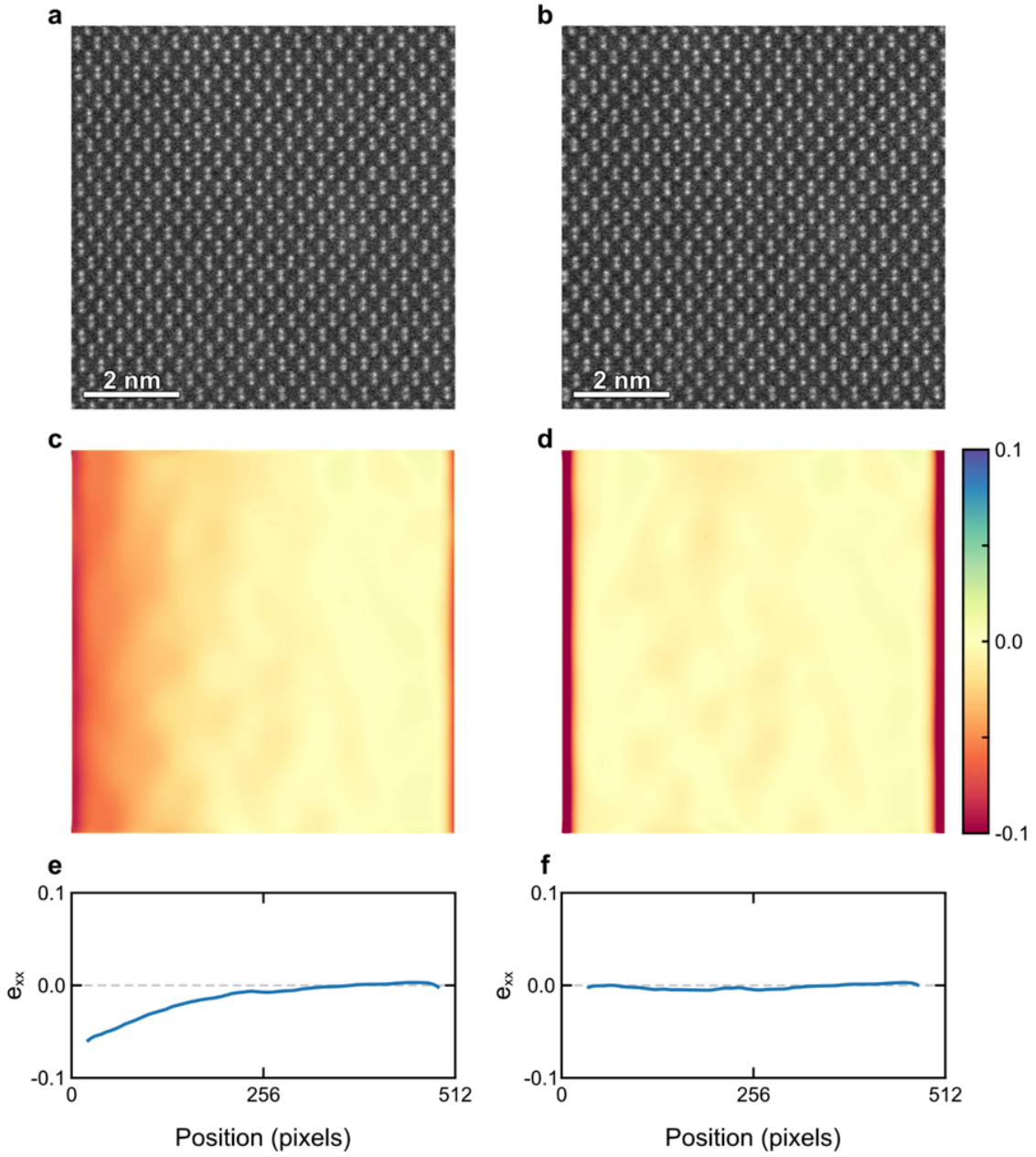

Figure 4.9.: HAADF image of Si <110> captured with a dwell time of 1 μs, a line flyback time of 60 μs, and an image size of 512 $\times$ 512 pixels. **a** and **b** show the image before and after flyback hysteresis correction, respectively. **c** and **d** show e_{xx} distortion maps from **a** and **b** respectively. **e** and **f** show profiles of the median distortion from **c** and **d**, respectively, where the edge artefacts have been excluded. Image from [121].

final parameter to consider is scan rotation, with this covered in the next section.

4.5.3. Extending to Rotating Image Series

It has been previously stated in this thesis that multiframe imaging, and specifically multiframe imaging with scan rotation between each frame is a superior way to capture data compared to a single long exposure [67, 128]. This is as multiple observations allow for easier separation of the noise and drift from the "ground truth", i.e., the image. However, when a rotating multiframe image series is captured with the presence of flyback hysteresis, the effect can be devastating. No longer is one side of the image corrupted, but all sides.

Furthermore, when aligning this dataset via rigid registration the different compression artefacts in each scanning direction reduces the quality of the correlation used to align the data, leading to poorer drift correction. For non-rigid registration where the average frame is used as a starting estimate, such as with the SmartAlign algorithm, the degraded starting average frame can reduce the quality of the registration. The solution then is to correct the compression artefact in each single frame before any aligning is performed.

To correct the compression artefact as performed previously, the variation of A and b with rotation angle is first characterised. To do so, a total of 50 images were captured by changing the rotation angle in steps of 15° from 0° to 360°. At each angle, an image was captured with a dwell time of 5 μs and line flyback times of both 0 μs and 20 μs. The compression artefact was diagnosed at each of these settings, with the results shown in **Figure 4.10**.

Figure 4.10 shows that while b does not appear to vary in a meaningful way

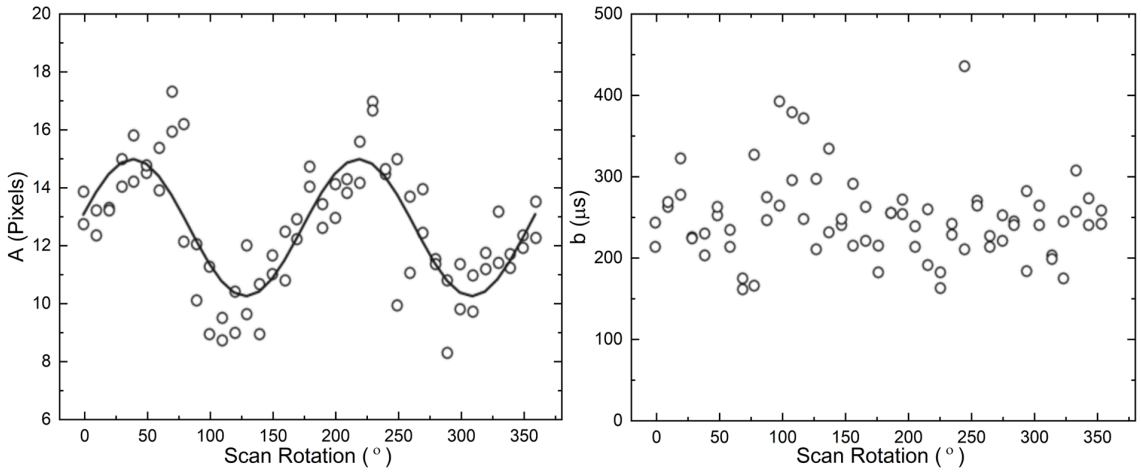

Figure 4.10.: The variation of A and b with rotation angle for a dwell time of 5 μs and line flyback times of 0 μs and 20 μs. The rotation angle increases in steps of 15° from 0° to 360°.

with rotation angle, A shows a sinusoidal variation with rotation angle. While a sole explanation is not sought, a possible explanation could be a difference in the coil windings in the x and y scan coils. Another point to note in this figure is that the maximum of the graph is not at zero rotation angle. This could be explained by a misalignment in the physical assembly or a manufacturer firmware offset (e.g., for orienting the stage to the Ronchigram camera). An offset was allowed in the fit to account for this. Although the physical origin of this effect is not known, it can be seen that there are two cycles of the sinusoid in a full rotation through 360° corresponding to the two-fold rotation symmetry of the scan coils. Knowing the variation of the scan coils with rotation angle it is now possible to correct the compression artefact in a rotating multiframe image series, as shown in **Figure 4.11**.

In **Figure 4.11** we see the same dataset twice, once where flyback hysteresis correction is applied as the first step, and the other without. When not applied, the

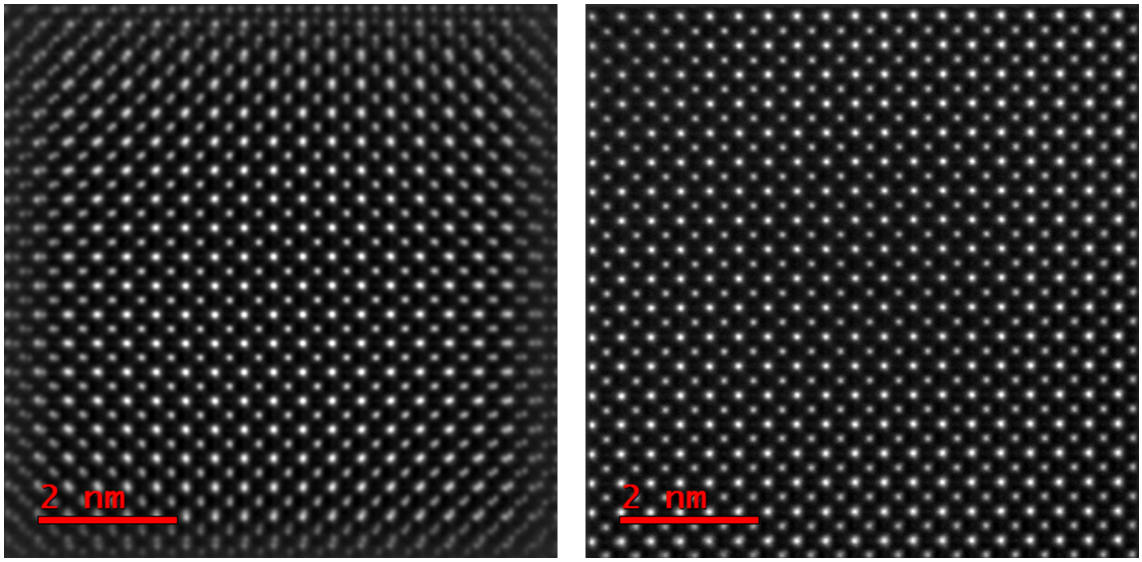

Figure 4.11.: Aligned average of 100 image frames of STO captured with a scan-rotation of 90° between frames and with a line flyback time of 20 μs. The image series is shown without flyback hysteresis correction applied before aligning (left), and with the correction applied before aligning (right). The compression artefact which degrades all sides of the image without the correction is eliminated in the image on the right. Image from [121].

compression artefact is very noticeable on all four sides of the final image. However, when the correction is applied before aligning and averaging, visual fidelity is maintained across the entire image.

Recalling that the original motivation for correcting the effects of flyback hysteresis is to increase scanning efficiency, we see why it is essential that flyback hysteresis correction is compatible with rotating multiframe image captures. This is because we see the largest increases in scanning efficiency when imaging at low dwell times, but when operating at low dwell times the SNR is lower, and multiframe imaging becomes a necessary to achieve a suitable signal level.

4.6. Conclusions

That concept introduced in this chapter is that while lowering the electron dose is naturally an important step towards lowering sample damage, it alone is not enough. This is because of scanning efficiency, where it was shown that when operating at the most widely accessible low-dose conditions (using low beam currents and short dwell times), often less than half of the electrons damaging the sample are producing useful information. This is because of the line and frame flyback times, which occupy an increasingly larger proportion of the duration of each image when dwell times are lowered.

The solution proposed then, was to lower the line flyback time. While simple to do so in practice, the line flyback time has the important role of allowing the electron beam to reach a constant velocity before beginning each scan line. When shortened to a time where this is no longer possible, a compression artefact in seen at the beginning of each line in the image as the electron beam is lagging behind

its intended position. However, it was observed that this compression artefact was reproducible and followed an exponential form, making diagnosing and correcting the artefact in post-processing possible.

It was found that the magnitude A of the compression artefact has an inverse decay relation with the dwell time and varies sinusoidally with rotation angle, while the decay constant b increases linearly with dwell time and does not vary with rotation angle. Equations describing the inverse decay, linear fit, and sinusoid variation were fit, allowing for parameters to correct the compression artefact to be found for any imaging settings. With these results, it is now possible to see large increases in scanning efficiency for no losses in image quality, an essential part of low-dose imaging.

Chapter 5.

Ongoing Work & Future Work, & Conclusions

In this thesis, multiple new approaches to low dose-rate imaging have been introduced, from hardware based, to software , and also simulation based. While results have been obtained and the power of these techniques shown, in many ways these approaches are in their infancy and promise exciting future results, from both within the research group and with new collaborators. This exciting future, and some new results which have been obtained already will be explored in this chapter.

5.1. Alternate Scan Patterns

The topic of the previous chapter was scanning efficiency, and how for many microscopes used today, the one way to increase this is to reduce the line flyback time. A natural extension of this concept is to not only reduce the duration of the line flyback time, but to reduce the *number* of line flyback times in an image (beyond

simply reducing the number of image lines). Alternate scan patterns beyond the usual raster scan are one way to do so, with frame interlacing being one method chosen here to adopt to the STEM.

Interlacing, where only half of the lines in each frame are displayed at once (typically alternating between showing the even and odd lines on subsequent frames), is not a new technology. It was in fact developed for televisions in 1936, with the key outcome being that for the same frame rate and image resolution, interlaced video required half the bandwidth compared to a fully sampled video [129]. Conversely, for a given bandwidth, a doubling of the frame rate can be achieved. When applied to the STEM, this means that the frame rate can be doubled, and the number of line flyback times reduced for a given image size, increasing scanning efficiency. Furthermore, when used with deinterlacing techniques to reduce the losses of resolution and precision, this becomes a powerful approach to imaging, as detailed in [13].

When considering deinterlacing, there are many different algorithms which can be used, varying both in computation speed and reconstruction accuracy, with the latter also depending on the sample being imaged. The recommended approach from the paper is to begin with a fully sampled, representative image, artificially interlace it by removing half the lines, and then deinterlace it. As the goal of the reconstruction is known (the original image), each deinterlaced image can be compared against it, finding which algorithm is most suitable for each user's needs, with a Python script to enable this shared publicly in the paper. An example of this process is shown in **Figure 5.1**.

The key outcomes of this work are that, depending on the scan generator used, a near 100 % increase in framerate can be achieved. Furthermore, as a greater number of frames are produced for a given electron dose, interlacing and frame registration

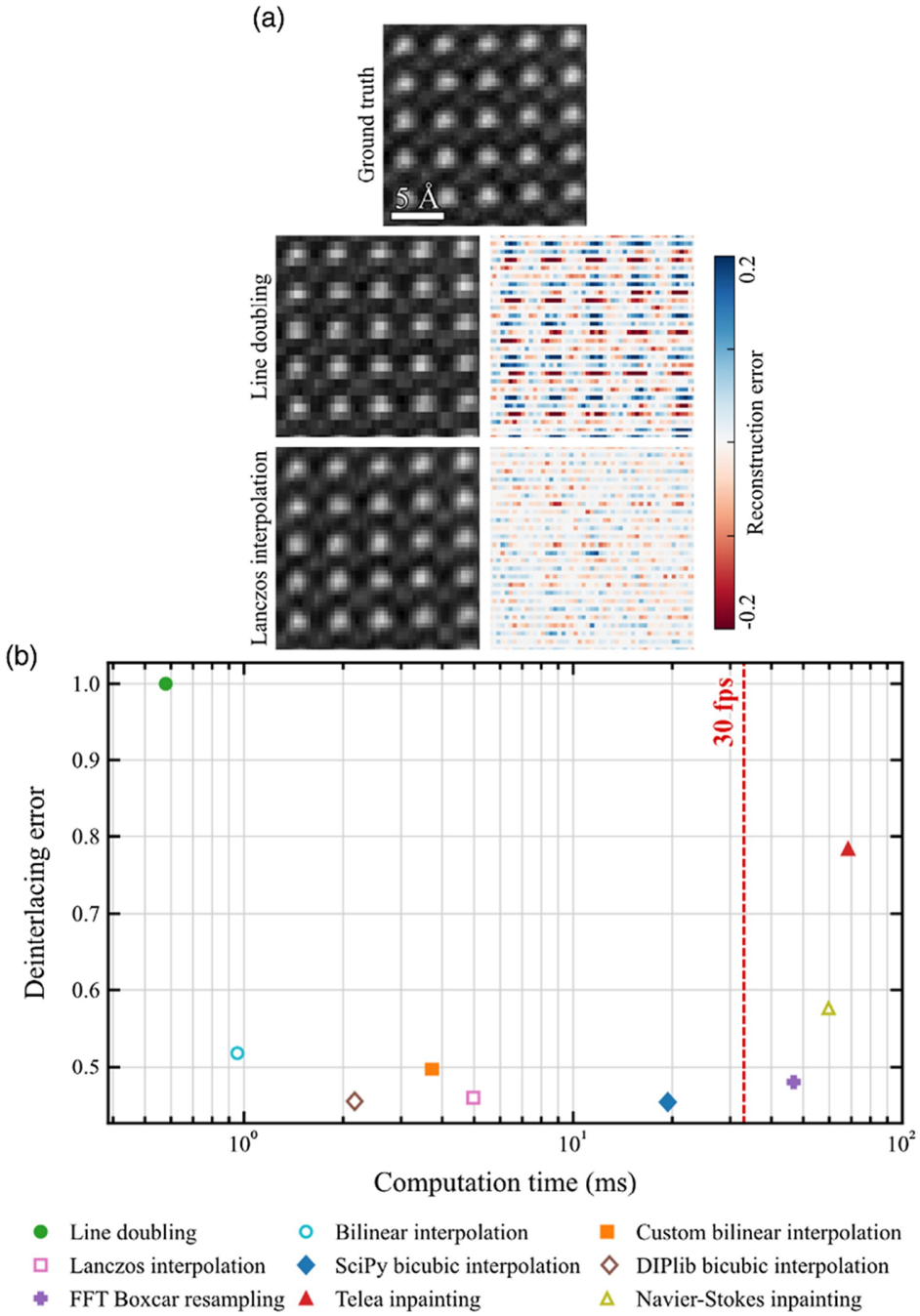

Figure 5.1.: (a): Experimental, fully sampled image of $PbZr_{0.2}Ti_{0.8}O_3$ and two images which have been artificially interlaced and deinterlaced using line doubling and Lanczos deinterlacing methods, with their associated reconstruction errors [130]. **(b)**: Deinterlacing error, calculated as the root mean square error from the fully sampled image, versus computation time for a selection of deinterlacing methods. The computation times are the average of 1,000 calculations performed on an Intel i7-10700. Image adapted with permission from [13].

naturally work well together. Indeed, for a given dose, capturing twice as many interlaced frames showed an increase in strain precision of 1.4 ± 0.1 when compared to half the number of fully sampled frames on an experimental image series of STO. Apparent probe displacements resulting from uncorrelated, randomised scan distortions can be considered to have a Gaussian-like distribution [94]. In this case, the width of this distribution should decrease as $1/\sqrt{n}$ when averaging multiple image frames (where n is the number of frames). This explains this result, as capturing twice as many frames results in an additional $\sqrt{2}$, or $sim1.4$ improvement.

One natural extension to this work currently being investigated is the use of scan patterns with no line flyback times at all. Examples of such patterns are serpentine or snake scanning, Hilbert space filling curves, and spiral scans, which have been previously discussed and demonstrated [85, 86]. The use of a Point electronic DISS 6 scan generator has allowed our own exploration of these scan patterns, with serpentine scanning, where the beam moves left to right, then a single pixel downwards, then right to left, showing promising results. This is because the artefacts which appear in images captured this way show distortions similar to that caused by lowering the line flyback time for a regular raster scan, and can be corrected in the same way. With this approach it is possible to achieve imaging with no line flyback time, or indeed frame flyback time, achieving 100 % scanning efficiency.

5.2. Machine Learning

It was previously shown in this thesis that digital images do not contain various sources of noise such as signal streaking and detector afterglow, and, as digitisation

only counts electrons, nor does it contain Gaussian noise. One fundamental source of noise which remains however, is Poisson noise. Poisson noise arises due to the quantised nature of the electron beam and cannot be eliminated experimentally, increasing as the electron dose decreases according to the relation:

$$N \propto \frac{1}{\sqrt{d}}, \tag{5.1}$$

where n is the noise, and d is the dose. As this cannot be eliminated experimentally, one approach is to instead turn to machine learning. To do so, an experimental digital dataset of a gold nanoparticle on an amorphous carbon background was provided to a collaborator working on a denoising algorithm for STEM images [131]. The dataset provided was an aligned stack of 20 low-dose image frames, where differing number of frames in the stack could be summed to produce higher SNR images to test the algorithm at varying dose levels. A visual comparison of the data before and after denoising for three different dose levels is shown in **Figure 5.2**.

In this image, improvements in image quality are seen at all dose levels, but the performance of the denoising algorithm improves with increasing dose. Despite this, even at low-doses the increase in image quality is great enough to readily recognise the five crystallites which form the gold nanoparticle.

5.3. Digital DPC

While only digital HAADF images have been shown in this thesis, with enough inputs, this technique can be readily extended to imaging modes where more than a single datastream is required to form an image, such as differential phase-contrast

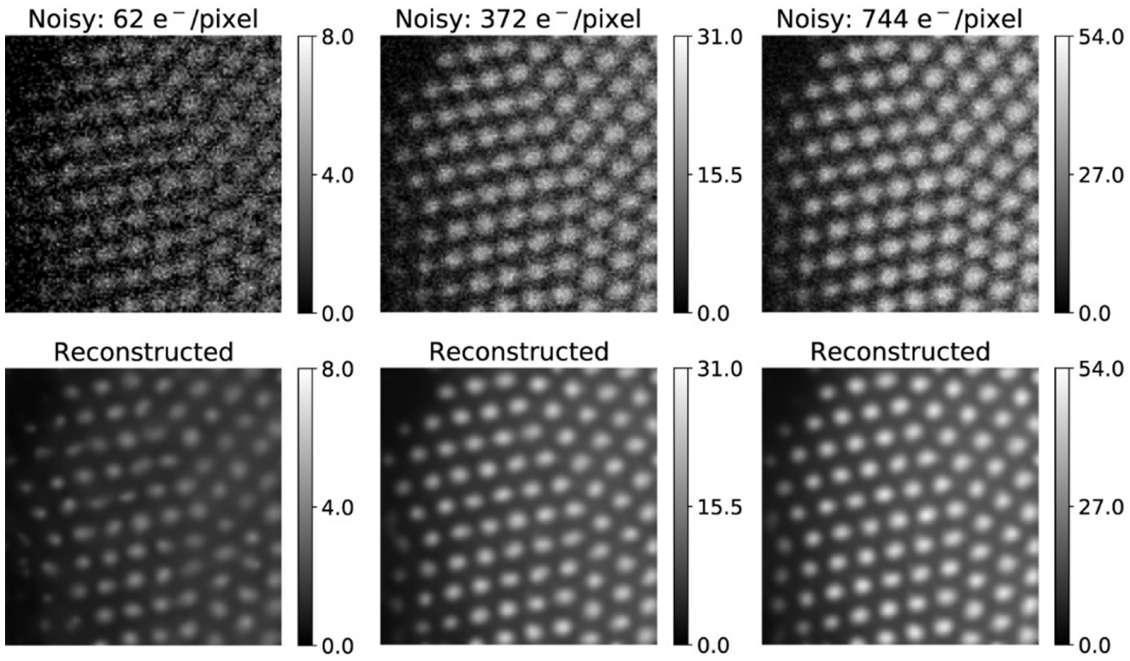

Figure 5.2.: In the top row, three images of the same sample of a gold nanoparticle on an amorphous carbon background are shown for increasing electron dose. Below this row are the corresponding images after application of the denoising algorithm. In each case, a significant visual improvement can be seen. Image adapted with permission from [131].

(DPC) imaging.

Electric or magnetic fields in a sample can deflect electrons in the beam, resulting in an intensity distribution within the beam. This intensity distribution can be measured using an appropriate detector, and then used to calculate fields in the sample. Doing so requires a detector with multiple readout channels, such as pixelated or segmented detectors [132]. By using a four-segmented detector, deflection can be measured in two mutually perpendicular directions, as shown in **Figure 5.3**.

As shown in this figure, when an electromagnetic field is present in the sample, the signal level is not equal in all segments of the detector. In this case, the difference in signal levels in opposite detector segments is non-zero, and this can be related

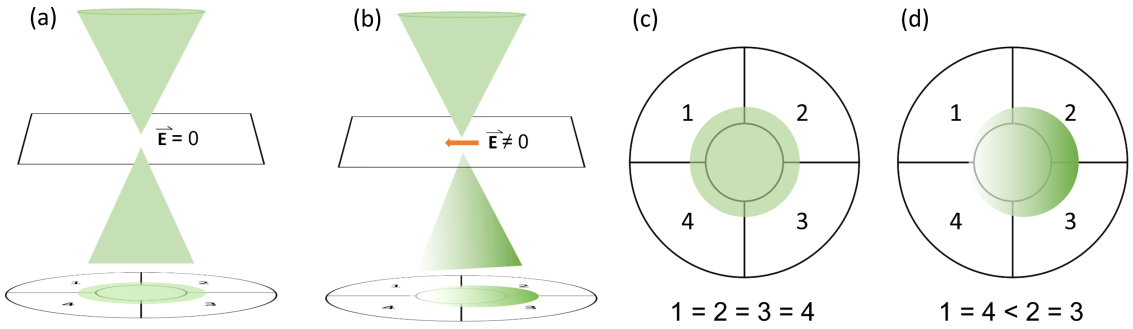

Figure 5.3.: **(a)**: In a sample containing no electric field the beam is not deflected. **(b)**: When the electric field is non-zero, the beam is deflected and intensity is redistributed within the beam. **(c)**: Overhead view of the detector when no electric field is present. The electron beam intensity is equal in all segments. **(d)**: Overhead view of the detector in the presence of an electric field. Segments 2 and 3 now have a greater signal level than segments 1 and 2.

to the fields in the sample. An interesting question arises when considering DPC imaging at very low doses, where the signal level in opposite segments may differ by a small number of electrons. In this case, when the difference signal is so small, statistical fluctuations in the distribution of the electrons may lead to falsely large values for the fields in the sample.

Furthermore, if operating at low-dose conditions, signal streaking again becomes a factor. While signal streaking has been investigated for ADF imaging in this thesis, how this artefact propagates when combining multiple channels of information has not. Research into this area has begun with a PhD student in the group, who has adapted the streaking simulation code to STEM-DPC imaging, and also compared the SNR between analog and digital DPC [133]. An example of the streaking simulation code applied to STEM-DPC data is shown in **Figure 5.4**.

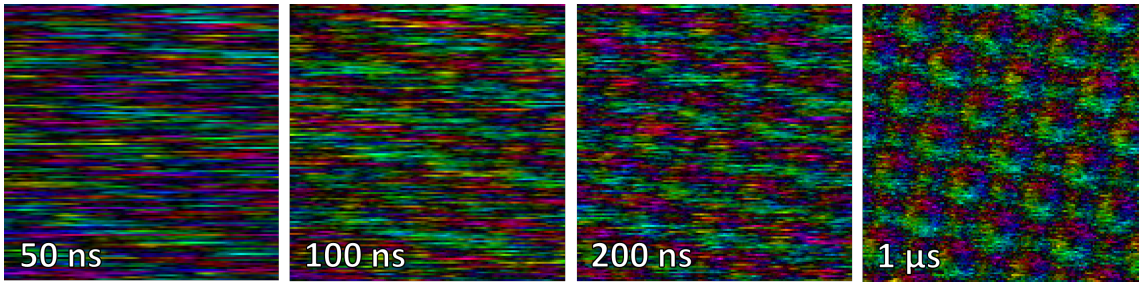

Figure 5.4.: Simulated STEM-DPC images of STO where signal streaking has been added. The dwell time of each image is shown in the bottom left corner.

5.4. Tempo STEM

While the ability to count electrons was developed to create digital images, it has gone on to enable the creation of a new STEM imaging mode. This imaging mode, **t**rigger-**e**vent **m**odulated **p**robability **o**bservation (Tempo) STEM, combined electron counting with beam blanking to create images of similar, or identical, SNRs to a regular image with large reductions in the dose required [134].

Instead of imaging for a fixed pixel dwell time, with Tempo STEM a fixed number of electrons are counted at each pixel, and the time taken to count this number of electrons is used to calculate the rate of arrival of electrons. As heavier elements scatter more electrons than lighter ones, they also scatter them at a greater rate, resulting in brighter pixels, the same as ADF STEM imaging. When this number has been reached, beam blanking is used to prevent unnecessary damage to the sample until the next pixel.

By increasing the required number of electron events per pixel the SNR of the final image can be increased. Hence, by setting the appropriate number of electrons required the reach the required signal level, no more sample damage than is absolutely required occurs. Initial results have shown dose savings of ∼60 % when

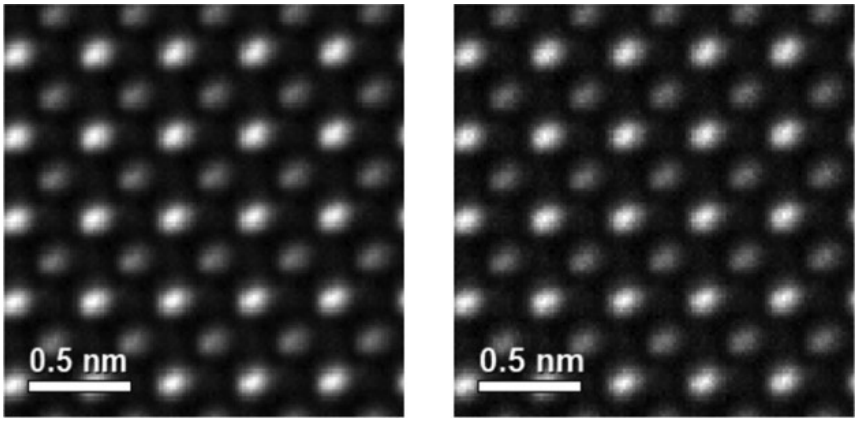

Figure 5.5.: Symmetry averaged ADF STEM image of STO (left), with a simultaneously acquired Tempo STEM image (right). The dwell time is 20 μs on the left, and the number of electron impacts per pixel is 6 on the right. Despite using $\sim$60 % of the dose of the conventional image, the Tempo STEM image is nearly identical in appearance. Reprinted with permission from [134], with permission from Oxford University Press.

imaging STO using electron counting and an IDES electrostatic dose modulation system for beam blanking, as shown in **Figure 5.5** [134, 135].

5.5. Graphene Results

Though results from two different experiments on graphene have been shown in this thesis, there is further work currently being undertaken to gain a greater understanding. For example, understanding the behaviour of the cluster of five silicon atoms requires density functional theory (DFT), a powerful but complex computational quantum mechanical modelling method [136]. DFT can reveal, for example, the bonding of the silicon cluster to the host graphene, the energy of the conformation change of the cluster, and how the structure of the cluster varies to that of a free cluster. While such calculations have been performed for a cluster of six silicon atoms on graphene, doing so here would demonstrate how the data could be

captured at high framerates (33 f.p.s.) while still achieving the necessary resolution to identify the conformation changes [111].

One other experiment performed on graphene was imaging of a monovacancy. Knowing that 2000 image frames would need be aligned, the original motivation for imaging this region of the sample was to use the monovacancy to aid in alignment, effectively using it as a fiducial marker. However, upon aligning and summing the data, brighter atoms around the vacancy were observed, corresponding to those atoms having larger Debye-Waller factors. Observing this indicated the precision of the image due to the digital methods used, and future comparisons with simulations will be used to verify how close to the ground-truth that this image is.

5.6. Conclusions

This thesis begins by detailing decades of STEM history, and how the need to increase microscope performance was the key driving force behind numerous new technologies and techniques. Through many impressive developments, we have now arrived at a time where, for many samples, instrument performance is no longer the limiting factor. Instead, damage to the sample caused by focusing ever more electrons into finer probes is often the limiting factor. The solution then, is to develop new, low-dose imaging techniques, with those I have developed during my PhD shown here.

Chapter 2 begins by introducing a universally accessible approach to low-dose imaging; using a lower beam current and faster scanning speeds. However, when operating under these conditions, signal streaking appears. This occurs when signal which should be localised to one pixel instead streaks into subsequent pixels due

to the finite decay time of the detector and readout electronics used. To combat this, hardware capable of digitising the signal was created, capable of eliminating not only signal streaking, but other sources of noise in images.

To demonstrate the benefits of digitisation, images of a biological tissue and a lamella were captured. In the analog versus digital image comparison of the biological tissue signal streaking is eliminated, massively increasing image quality at low current and high speeds, allowing this fragile sample to be imaged. In the lamella comparison, afterglow is notably missing in the digital image and the vacuum appears far more black as only electron impacts are counted as signal. In all cases, as the digital signal is formed by counting electrons, pixel values in images become quantitative and are no longer arbitrary grey values.

One further experiment chosen was to image graphene, to demonstrate how the choice between temporal and spatial resolution is not required when using digitisation, as the noise level in each image is so low. The dynamics of a silicon cluster on graphene are demonstrated at a framerate of ∼31 f.p.s. while atomic resolution images can still be formed, showing an improvement in temporal resolution of ∼200 compared to similar, previous experiments. Digitisation represents not only a way to allow the use of the most widely available low-dose imaging conditions, but also a sustainable, retrofittable way to increase the performance of existing detectors.

In **Chapter 3**, the quantitative improvements that digitisation makes are explored by looking at the effect of digitisation on detector performance and by simulating signal streaking. Detector maps are commonly used to evaluate detector performance, whether simply to measure imperfections, or to incorporate these imperfections into simulated images. Examples of imperfections are an uneven, inhomogeneous response, a non-ideal shape, or even damage suffered by the detector. In this chapter,

simultaneously captured analog and digital detector maps from eight detectors are used to quantify the increase in performance.

Upon digitisation, the average flatness, roundness, and smoothness deviations of the detectors from the ideal decreased by 6.78 %, 9.97 %, and 32.06 % respectively. This brings detectors closer to their counterparts used in simulations, and in turn the images they produce. One other aspect of detector performance improved by digitisation is their speed. Measurements of the response of the detectors show overall response times ranging from approximately 200 ns, to over 1.5 μs. In the digital signal all electron impacts are localised to exactly one time value, hence the absence of signal streaking.

To further investigate the effects of signal streaking, code was written to add signal streaking as it would appear on various detectors to simulated images, isolating its effects. Comparisons were generated for both fixed imaging settings for a range of detectors, and for a fixed choice of detector with varying dwell times. In each case, as signal streaking becomes more severe, whether due to slower detector speeds or shorter dwell times, images appear streaked, and a loss in intensity in the Fourier transforms is seen. A purely simulation based approach which matches an experimental example is used to show how these effects are caused solely by signal streaking, highlighting its negative effects. A route to measure the detector decay time from the intensity profile is identified, with the future goal of defining the Temporal Transfer function.

Signal streaking is the primary drawback of scanning at high-speeds, but the line flyback time leads to another issue under these imaging conditions. In **Chapter 4** the topic of scanning efficiency is raised, and how, for a fixed line flyback time, this decreases massively (from over 90 % to less than 20 %) when the dwell time is

decreased from 38 μs to 50 ns. The solution proposed is to decrease the line flyback time, but this also leads to a compression artefact in the image.

This artefact arises as there is a non-zero response time between current changes in the current in the scan coils and changes in the driving voltage, leading to a lag between the intended position of the electron beam and its actual position. Due to this hysteresis, the beam scans an overly large area until it reaches a constant velocity, and fitting this extra area into the image causes the data to appear compressed at the start of each line. This is particularly damaging when an image series with scan rotation between frames is used, as this artefact becomes present on each side of the image.

The solution found is to measure this compression via comparison with a distortion free reference, such as a single crystal. This artefact is found to be replicable, and by capturing images for varying line flyback times, dwell times, and scan rotations, a semi-empirical model of the hysteresis could be created. Using this model, which only needs to be created once, the compression artefact can be removed from any data captured on the instrument, regardless of imaging settings used.

Removing the compression artefact on the Digiscan II controlled Nion UltraSTEM used to capture the data increased the scanning efficiency from 50 % to 70 % when decreasing the line flyback time from 600 μs to 20 μ. Even larger increases in scanning efficiency could be achieved (to over 95 %) if the frame flyback time, measured to be $\sim$0.25 s, could be reduced or eliminated. Scan rotation is an effective way to increase SNR in low-dose data, and so it is important that it was shown that correction of the compression artefact is possible on data captured using this method, allowing distortion-free, low-dose, high-SNR images to be formed.

Chapter 5 details further ongoing work, as well as plans for future work which

has resulted from my PhD. This includes ongoing work into alternate scan patterns such as interlacing and serpentine scanning to eliminate the line flyback time, and the use of machine learning to decrease the effects of Poisson noise on digital data. Future work on digital STEM-DPC data, a new imaging mode which utilises electron counting, and further exploration of the maths underlying signal streaking are just some of the exciting prospects mentioned, all working towards the ultimate goal of counting every electron, and making every electron count.

Bibliography

[1] Mullarkey, T., Downing, C., and Jones, L., *Development of a Practicable Digital Pulse Read-Out for Dark-Field STEM*, Microscopy and Microanalysis **27** (2020), 99–108.

[2] Feynman, RP., *There's Plenty of Room at the Bottom*, Engineering and Science **23** (1960), 22–36.

[3] Krivanek, O., Chisholm, MF., Nicolosi, V., Pennycook, T., Corbin, GJ., Dellby, N., Murfitt, M., Own, CS., Szilagyi, ZS., Oxley, MP., Pantelides, ST., and Pennycook, SJ., *Atom-by-atom structural and chemical analysis by annular dark-field electron microscopy*, Nature **464** (2010), 571–4.

[4] Qiao, Q., Zhang, Y., Contreras-Guerrero, R., Droopad, R., Pantelides, ST., Pennycook, SJ., Ogut, S., and Klie, RF., *Direct observation of oxygen-vacancy-enhanced polarization in a SrTiO3-buffered ferroelectric BaTiO3 film on GaAs*, Applied Physics Letters **107** (2015).

[5] Chang, HJ., Kalinin, SV., Morozovska, AN., Huijben, M., Chu, YH., Yu, P., Ramesh, R., Eliseev, EA., Svechnikov, GS., Pennycook, SJ., and Borisevich, AY., *Atomically Resolved Mapping of Polarization and Electric Fields Across*

Ferroelectric/Oxide Interfaces by Z-contrast Imaging, Advanced Materials **23** (2011), 2474–2479.

[6] Ruska, E., *The Development of the Electron Microscope and of Electron Microscopy (Nobel Lecture)*, Angewandte Chemie International Edition in English **26** (1987), 595–605.

[7] Lord Rayleigh, F., *XXXI. Investigations in optics, with special reference to the spectroscope*, The London, Edinburgh, and Dublin Philosophical Magazine and Journal of Science **8** (1879), 261–274.

[8] Huang, B., *Super-resolution optical microscopy: multiple choices*, Current Opinion in Chemical Biology **14** (2010), 10–14.

[9] NobelPrize.org, , *The Nobel Prize in Chemsitry 2014*, https://www.nobelprize.org/prizes/chemistry/2014/summary/, Accessed August 2023.

[10] Rose, HH., *Historical aspects of aberration correction*, Journal of Electron Microscopy **58** (2009), 77–85.

[11] Busch, H., *Berechnung der Bahn von Kathodenstrahlen im axialsymmetrischen elektromagnetischen Felde*, Annalen der Physik **386** (1926), 974–993.

[12] Knoll, M. and Ruska, E., *Das Elektronenmikroskop*, Zeitschrift für Physik **78** (1932), 318–339.

[13] Peters, JJP., Mullarkey, T., Gott, JA., Nelson, E., and Jones, L., *Interlacing in Atomic Resolution Scanning Transmission Electron Microscopy*, Microscopy and Microanalysis **29** (2023), 1373–1379.

[14] Ruska, E., *The development of the electron microscope and of electron microscopy*, Reviews of Modern Physics **59** (1987), 627–638.

[15] Haguenau, F., Hawkes, P., Hutchison, J., Satiat–Jeunemaître, B., Simon, G., and Williams, D., *Key Events in the History of Electron Microscopy*, Microscopy and Microanalysis **9** (2003), 96–138.

[16] Bain, A., *Electric time-pieces and telegraphs*, British Patent No. 9745 (1843).

[17] McMullan, D., *Scanning electron microscopy 1928-1965*, Scanning **17** (2006), 175–185.

[18] Knoll, M., *Aufladepotential und Sekundaremission elektronenbestrahlter Korper*, Zeitschrift für technische Physik **16** (1935), 467–475.

[19] Zworykin, VA., Hillier, J., and Snyder, RL., *A scanning electron microscope.*, 1942.

[20] Liu, JJ., *Advances and Applications of Atomic-Resolution Scanning Transmission Electron Microscopy*, Microscopy and Microanalysis **27** (2021), 943–995.

[21] von. Ardenne, M., *Das Elektronen-Rastermikroskop. Praktische Ausführung (The scanning electron microscope — practical construction)*, Zeitschrift für Physik **19** (1938), 407–416.

[22] Von Ardenne, M., Hawkes, P., and Mulvey, T., *On the history of scanning electron microscopy, of the electron microprobe, and of early contributions to transmission electron microscopy*, in The Beginnings of Electron Microscopy - Part 1, Hawkes, PW. and Hÿtch, M., eds., vol. 220 of Advances in Imaging and Electron Physics, Elsevier, 2021, 25–50.

[23] von. Ardenne, M., *Das elektronen-rastermikroskop. Praktische ausführung*, Zeitschrift für technische Physik **19** (1938), 407–416.

[24] ——, *Die Grenzen für das Auflösungsvermögen des Elektronenmikroskops*, Zeitschrift für Physik **108** (1938), 338–352.

[25] ——, *Das Elektronen-Rastermikroskop. Theoretische Grundlagen*, Zeitschrift für Physik **109** (1938), 553–572.

[26] ——, *Intensitätsfragen und Auflösungsvermögen des Elektronenmikroskops*, Zeitschrift für Physik **112** (1939), 744–752.

[27] ——, *Über das Auftreten von Schwärzungslinien bei der elektronenmikroskopischen Abbildung kristalliner Lamellen*, Zeitschrift für Physik **116** (1940), 736–738.

[28] Crewe, AV., *A new kind of scanning microscope*, J Microsc **2** (1963), 369–371.

[29] Crewe, AV., *Scanning Electron Microscopes: Is High Resolution Possible?*, Science **154** (1966), 729–738.

[30] Oatley, CW., Nixon, WC., and Pease, RFW., *Scanning Electron Microscopy*, in Advances in Electronics and Electron Physics, Marton, L., ed., Academic Press, 1966, 181–247.

[31] Pease, RFW. and Nixon, WC., *High resolution scanning electron microscopy*, Journal of Scientific Instruments **42** (1965), 81–85.

[32] Crewe, AV., Eggenberger, DN., Wall, J., and Welter, LM., *Electron Gun Using a Field Emission Source*, Review of Scientific Instruments **39** (1968), 576–583.

[33] Crewe, A. and Wall, J., *A scanning microscope with 5 Å resolution*, Journal of Molecular Biology **48** (1970), 375–393.

[34] Crewe, AV., Wall, J., and Langmore, J., *Visibility of Single Atoms*, Science **168** (1970), 1338–1340.

[35] Engel, A., Wiggins, JW., and Woodruff, DC., *A comparison of calculated images generated by six modes of transmission electron microscopy*, Journal of Applied Physics **45** (1974), 2739–2747.

[36] Misell, DL., Stroke, GW., and Halioua, M., *Coherent and incoherent imaging in the scanning transmission electron microscope*, Journal of Physics D: Applied Physics **7** (1974), L113–L117.

[37] Burge, RE. and Dainty, JC., *Partially coherent image formation in the scanning transmission electron microscope (STEM)*, Optik **46** (1976), 229–240.

[38] Engel, A., *Molecular weight determination by scanning transmission electron microscopy*, Ultramicroscopy **3** (1978), 273–281.

[39] Humphreys, C., Sandstrom, R., and Spencer, J., *Contrast enhancement from single atoms and crystals using energy analysis*, in Proceedings of the 6th Annual SEM Symposium, Johari, O., ed., Chicago, IL., 1973, IIT Research Institute, 233–242.

[40] Crewe, AV., Langmore, J., and Isaacson, M., *No Title*, in Physical Aspects of Electron Microscopy and Microbeam Analysis, Siegel, B. and Beaman, D., eds., Wiley, New York, NY, 1975, 47–62.

[41] Treacy, MMJ., Howie, A., and Wilson, CJ., *Z contrast of platinum and palladium catalysts*, Philosophical Magazine A **38** (1978), 569–585.

[42] Treacy, M., Howie, A., and Pennycook, S., *No Title*, in Electron Microscopy and Analysis 1979, Mulvey, T., ed., Brighton, 1980, Institute of Physics, 261–266.

[43] Pennycook, SJ., *Study of supported ruthenium catalysts by STEM*, Journal of Microscopy **124** (1981), 15–22.

[44] Pennycook, SJ. and Narayan, J., *Direct imaging of dopant distributions in silicon by scanning transmission electron microscopy*, Applied Physics Letters **45** (1984), 385–387.

[45] Rafferty, B., Nellist, D., and Pennycook, J., *On the origin of transverse incoherence in Z-contrast STEM*, Microscopy **50** (2001), 227–233.

[46] Jesson, DE. and Pennycook, SJ., *Incoherent imaging of crystals using thermally scattered electrons*, Proceedings of the Royal Society of London. Series A: Mathematical and Physical Sciences **449** (1995), 273–293.

[47] Scherzer, O., *Uber einige Fehler von Elektronenlinsen*, Zeitschrift für Physik **101** (1936), 593–603.

[48] Crewe, AV., Cohen, D., and Meads, P., *A multipole element for the correcting of spherical aberration*, in Proceedings of the 4th Regional Conference of Electron Microscopy I, 1968, 183.

[49] Beck, V. and Crewe, AV., *A quadrupole octupole corrector for a 100 keV*

STEM, in Proceedings of the Annual Meeting of the Electron Microscopy Society of America, vol. 32, Cambridge University Press, 1974, 426–427.

[50] Crewe, A., *Some Chicago Aberrations*, Microscopy and Microanalysis **10** (2004), 414–419.

[51] Zach, J. and Haider, M., *Aberration correction in a low voltage SEM by a multipole corrector*, Nuclear Instruments and Methods in Physics Research Section A: Accelerators, Spectrometers, Detectors and Associated Equipment **363** (1995), 316–325.

[52] Haider, M., Braunshausen, G., and Schwan, E., *Correction of the spherical aberration of a 200 kV TEM by means of a hexapole-corrector*, Optik **99** (1995), 167–179.

[53] Rose, H., *Outline of a spherically corrected semiaplanatic medium-voltage transmission electron microscope*, Optik **85** (1990), 19–24.

[54] Krivanek, OL., Dellby, N., Spence, AJ., Camps, RA., and Michael Brown, L., *On-Line Aberration Measurement and Correction in STEM*, Microscopy and Microanalysis **3** (1997), 1171–1172.

[55] Krivanek, OL., Dellby, N., Spence, AJ., Camps, RA., and Brown, LM., *Aberration correction in the STEM*, in Proceedings of the Institute of Physics Electron Microscopy and Analysis Group Conference 1997, CRC Press, CRC Press, 2022, 35–40.

[56] Pennycook, SJ., *The impact of STEM aberration correction on materials science*, Ultramicroscopy **180** (2017), 22–33.

[57] *In recognition of aberration-corrected TEM*, Nature Nanotechnology **15** (2020), 417–417.

[58] MacLaren, I., Macgregor, TA., Allen, CS., and Kirkland, AI., *Detectors—The ongoing revolution in scanning transmission electron microscopy and why this important to material characterization*, APL Materials **8** (2020), 110901.

[59] Faruqi, A. and McMullan, G., *Direct imaging detectors for electron microscopy*, Nuclear Instruments and Methods in Physics Research Section A: Accelerators, Spectrometers, Detectors and Associated Equipment **878** (2018), 180–190.

[60] Jones, L., *Quantitative ADF STEM: acquisition, analysis and interpretation*, IOP Conference Series: Materials Science and Engineering **109** (2016), 012008.

[61] Pennycook, SJ. and Nellist, PD., *Scanning Transmission Electron Microscopy*, Springer New York, New York, 2011.

[62] Pennycook, SJ. and Howie, A., *Study of single-electron excitations by electron microscopy II. Cathodoluminescence image contrast from localized energy transfers*, Philosophical Magazine A **41** (1980), 809–827.

[63] Pennycook, SJ., Brown, LM., and Craven, AJ., *Observation of cathodoluminescence at single dislocations by STEM*, Philosophical Magazine A **41** (1980), 589–600.

[64] Kirkland, EJ. and Thomas, MG., *A high efficiency annular dark field detector for STEM*, Ultramicroscopy **62** (1996), 79–88.

[65] Everhart, TE. and Thornley, RFM., *Wide-band detector for micro-microampere low-energy electron currents*, Journal of Scientific Instruments **37** (1960), 246–248.

[66] Frame, PW., *A history of radiation detection instrumentation*, Health Physics **87** (2004), 111–135.

[67] Sang, X. and LeBeau, JM., *Revolving scanning transmission electron microscopy: Correcting sample drift distortion without prior knowledge*, Ultramicroscopy **138** (2014), 28–35.

[68] Autrata, R., Schauer, P., Kvapil, J., and Kvapil, J., *A single crystal of YALO3: Ce3+ as a fast scintillator in SEM*, Scanning **5** (1983), 91–96.

[69] Kaneko, T., Saitow, A., Fujino, T., Okunishi, E., and Sawada, H., *Development of a high-efficiency DF-STEM detector*, Journal of Physics: Conference Series **522** (2014), 012050.

[70] Ophus, C., *Four-Dimensional Scanning Transmission Electron Microscopy (4D-STEM): From Scanning Nanodiffraction to Ptychography and Beyond*, Microscopy and Microanalysis **25** (2019), 563–582.

[71] Savitzky, BH., Zeltmann, SE., Hughes, LA., Brown, HG., Zhao, S., Pelz, PM., Pekin, TC., Barnard, ES., Donohue, J., Rangel DaCosta, L., Kennedy, E., Xie, Y., Janish, MT., Schneider, MM., Herring, P., Gopal, C., Anapolsky, A., Dhall, R., Bustillo, KC., Ercius, P., Scott, MC., Ciston, J., Minor, AM., and Ophus, C., *py4DSTEM: A Software Package for Four-Dimensional Scanning Transmission Electron Microscopy Data Analysis*, Microscopy and Microanalysis **27** (2021), 712–743.

[72] Gnanasekaran, K., de. With, G., and Friedrich, H., *Quantification and optimization of ADF-STEM image contrast for beam-sensitive materials*, Royal Society Open Science **5** (2018), 171838.

[73] Buban, JP., Ramasse, Q., Gipson, B., Browning, ND., and Stahlberg, H., *High-resolution low-dose scanning transmission electron microscopy*, Journal of Electron Microscopy **59** (2010), 103–112.

[74] Chen, Q., Dwyer, C., Sheng, G., Zhu, C., Li, X., Zheng, C., and Zhu, Y., *Imaging Beam-Sensitive Materials by Electron Microscopy*, Advanced Materials **32** (2020), 1907619.

[75] Egerton, R., *Radiation damage to organic and inorganic specimens in the TEM*, Micron **119** (2019), 72–87.

[76] B. Carlson, D. and E. Evans, J., *Low-Dose Imaging Techniques for Transmission Electron Microscopy*, in The Transmission Electron Microscope, Maaz, K., ed., InTechOpen, Rijeka, apr 2012, ch. 5, 85 – 98.

[77] Csencsits, R. and Gronsky, R., *Damage of zeolite Y in the TEM and its effects on TEM images*, Ultramicroscopy **23** (1987), 421–431.

[78] Karuppasamy, M., Karimi Nejadasl, F., Vulovic, M., Koster, AJ., and Ravelli, RBG., *Radiation damage in single-particle cryo-electron microscopy: effects of dose and dose rate*, Journal of Synchrotron Radiation **18** (2011), 398–412.

[79] Meents, A., Gutmann, S., Wagner, A., and Schulze-Briese, C., *Origin and temperature dependence of radiation damage in biological samples at cryogenic*

temperatures, Proceedings of the National Academy of Sciences **107** (2010), 1094–1099.

[80] Egerton, R., *Control of radiation damage in the TEM*, Ultramicroscopy **127** (2013), 100–108.

[81] NobelPrize.org, , *The Nobel Prize in Chemistry 2017*, https://www.nobelprize.org/prizes/chemistry/2017/summary/, Accessed August 2023.

[82] Elbaum, M., *Quantitative Cryo-Scanning Transmission Electron Microscopy of Biological Materials*, Advanced Materials **30** (2018), 1706681.

[83] Stark, H., Zemlin, F., and Boettcher, C., *Electron radiation damage to protein crystals of bacteriorhodopsin at different temperatures*, Ultramicroscopy **63** (1996), 75–79.

[84] Egerton, R., *Chemical measurements of radiation damage in organic samples at and below room temperature*, Ultramicroscopy **5** (1980), 521–523.

[85] Velazco, A., Nord, M., Béché, A., and Verbeeck, J., *Evaluation of different rectangular scan strategies for STEM imaging*, Ultramicroscopy **215** (2020), 113021.

[86] Sang, X., Lupini, AR., Unocic, RR., Chi, M., Borisevich, AY., Kalinin, SV., Endeve, E., Archibald, RK., and Jesse, S., *Dynamic scan control in STEM: spiral scans*, Advanced Structural and Chemical Imaging **2** (2016), 6.

[87] Béché, A., Goris, B., Freitag, B., and Verbeeck, J., *Development of a fast*

electromagnetic beam blanker for compressed sensing in scanning transmission electron microscopy, Applied Physics Letters **108** (2016), 093103.

[88] Kovarik, L., Stevens, A., Liyu, A., and Browning, ND., *Implementing an accurate and rapid sparse sampling approach for low-dose atomic resolution STEM imaging*, Applied Physics Letters **109** (2016), 164102.

[89] Stevens, A., Yang, H., Carin, L., Arslan, I., and Browning, ND., *The potential for Bayesian compressive sensing to significantly reduce electron dose in high-resolution STEM images*, Microscopy **63** (2014), 41–51.

[90] Anderson, HS., Ilic-Helms, J., Rohrer, B., Wheeler, J., and Larson, K., *Sparse imaging for fast electron microscopy*, in IS&T/SPIE Electronic Imaging, Bouman, CA., Pollak, I., and Wolfe, PJ., eds., vol. 8657, feb 2013, 86570C.

[91] Van den Broek, W., Reed, BW., Beche, A., Velazco, A., Verbeeck, J., and Koch, CT., *Various Compressed Sensing Setups Evaluated Against Shannon Sampling Under Constraint of Constant Illumination*, IEEE Transactions on Computational Imaging **5** (2019), 502–514.

[92] Muller, A. and Grazul, J., *Optimizing the environment for sub-0.2 nm scanning transmission electron microscopy*, Journal of Electron Microscopy **50** (2001), 219–226.

[93] Muller, DA., Kirkland, EJ., Thomas, MG., Grazul, JL., Fitting, L., and Weyland, M., *Room design for high-performance electron microscopy*, Ultramicroscopy **106** (2006), 1033–1040.

[94] Jones, L., Wenner, S., Nord, M., Ninive, H., Løvvik, OM., Holmestad, R., and Nellist, PD., *Optimising multi-frame ADF-STEM for high-precision atomic-resolution strain mapping*, Ultramicroscopy **179** (2017), 57–62.

[95] Jones, L., Varambhia, A., Beanland, R., Kepaptsoglou, D., Griffiths, I., Ishizuka, A., Azough, F., Freer, R., Ishizuka, K., Cherns, D., Ramasse, QM., Lozano-Perez, S., and Nellist, PD., *Managing dose-, damage- and data-rates in multi-frame spectrum-imaging*, Microscopy **67** (2018), 98–113.

[96] Jones, L., Yang, H., Pennycook, TJ., Marshall, MSJ., Van Aert, S., Browning, ND., Castell, MR., and Nellist, PD., *Smart Align—a new tool for robust non-rigid registration of scanning microscope data*, Advanced Structural and Chemical Imaging **1** (2015), 1–16.

[97] Berkels, B., Binev, P., Blom, DA., Dahmen, W., Sharpley, RC., and Vogt, T., *Optimized imaging using non-rigid registration*, Ultramicroscopy **138** (2014), 45–56.

[98] Baccaro, S., Blažek, K., de. Notaristefani, F., Maly, P., Mares, J., Pani, R., Pellegrini, R., and Soluri, A., *Scintillation properties of YAP:Ce*, Nuclear Instruments and Methods in Physics Research Section A: Accelerators, Spectrometers, Detectors and Associated Equipment **361** (1995), 209–215.

[99] Sang, X. and LeBeau, JM., *Characterizing the response of a scintillator-based detector to single electrons*, Ultramicroscopy **161** (2016), 3–9.

[100] Mittelberger, A., Kramberger, C., and Meyer, JC., *Software electron counting for low-dose scanning transmission electron microscopy*, Ultramicroscopy **188** (2018), 1–7.

[101] Krause, FF., Schowalter, M., Grieb, T., Müller-Caspary, K., Mehrtens, T., and Rosenauer, A., *Effects of instrument imperfections on quantitative scanning transmission electron microscopy*, Ultramicroscopy **161** (2016), 146–160.

[102] Mullarkey, T., Geever, M., Peters, JJP., Griffiths, I., Nellist, PD., and Jones, L., *How Fast is Your Detector? The Effect of Temporal Response on Image Quality*, Microscopy and Microanalysis **29** (2023), 1402–1408.

[103] Ubizskii, S., Poshyvak, O., Afanassyev, D., Luchechko, A., Rabyk, V., and Zhydachevskyy, Y., *Role of Afterglow in Optically Stimulated Luminescence of YAP:Mn*, Acta Physica Polonica A **141** (2022), 379–385.

[104] Yamada, S., Ito, T., Gouhara, K., and Uchikawa, Y., *Electron-count imaging in SEM*, Scanning **13** (1991), 165–171.

[105] Uchikawa, Y., Gouhara, K., Yamada, S., Ito, T., Kodama, T., and Sardeshmukh, P., *Comparative study of electron counting and conventional analogue detection of secondary electrons in SEM*, Journal of Electron Microscopy **41** (1992), 253–260.

[106] Ishikawa, R., Lupini, AR., Findlay, SD., and Pennycook, SJ., *Quantitative annular dark field electron microscopy using single electron signals*, Microscopy and Microanalysis **20** (2014), 99–110.

[107] Agarwal, A., Simonaitis, J., Goyal, VK., and Berggren, KK., *Secondary electron count imaging in SEM*, Ultramicroscopy **245** (2023), 113662.

[108] Agarwal, A., Simonaitis, J., and Berggren, KK., *Image-histogram-based sec-*

ondary electron counting to evaluate detective quantum efficiency in SEM, Ultramicroscopy **224** (2021), 113238.

[109] Peters, JJP., Mullarkey, T., Hedley, E., Müller, KH., Porter, A., Mostaed, A., and Jones, L., *Electron counting detectors in scanning transmission electron microscopy via hardware signal processing*, Nature Communications **14** (2023), 5184.

[110] Ishikawa, R., Jimbo, Y., Terao, M., Nishikawa, M., Ueno, Y., Morishita, S., Mukai, M., Shibata, N., and Ikuhara, Y., *High spatiotemporal-resolution imaging in the scanning transmission electron microscope*, Microscopy **69** (2020), 240–247.

[111] Lee, J., Zhou, W., Pennycook, SJ., Idrobo, JC., and Pantelides, ST., *Direct visualization of reversible dynamics in a Si6 cluster embedded in a graphene pore*, Nature Communications **4** (2013), 1650.

[112] Singhal, A., Yang, J., and Gibson, J., *STEM-based mass spectroscopy of supported Re clusters*, Ultramicroscopy **67** (1997), 191–206.

[113] LeBeau, JM. and Stemmer, S., *Experimental quantification of annular dark-field images in scanning transmission electron microscopy*, Ultramicroscopy **108** (2008), 1653–1658.

[114] Macarthur, KE., Jones, LB., and Nellist, PD., *How flat is your detector? Non-uniform annular detector sensitivity in STEM quantification*, Journal of Physics: Conference Series **522** (2014), 1198–1199.

[115] Findlay, SD. and LeBeau, JM., *Detector non-uniformity in scanning transmission electron microscopy*, Ultramicroscopy **124** (2013), 52–60.

[116] Buzzetti, S., Guazzoni, C., and Longoni, A., *EROIC: a BiCMOS pseudo-gaussian shaping amplifier for high-resolution X-ray spectroscopy*, Nuclear Instruments and Methods in Physics Research Section A: Accelerators, Spectrometers, Detectors and Associated Equipment **512** (2003), 150–156.

[117] Rangel DaCosta, L., Brown, HG., Pelz, PM., Rakowski, A., Barber, N., O'Donovan, P., McBean, P., Jones, L., Ciston, J., Scott, M., and Ophus, C., *Prismatic 2.0 – Simulation software for scanning and high resolution transmission electron microscopy (STEM and HRTEM)*, Micron **151** (2021), 103141.

[118] Heideman, MT., Johnson, DH., and Burrus, CS., *Gauss and the history of the fast Fourier transform*, Archive for History of Exact Sciences **34** (1985), 265–277.

[119] Cooley, JW. and Tukey, JW., *An Algorithm for the Machine Calculation of Complex Fourier Series*, Mathematics of Computation **19** (1965), 297.

[120] Mainprize, JG. and Yaffe, MJ., *The effect of phosphor persistence on image quality in digital x-ray scanning systems*, Medical Physics **25** (1998), 2440–2454.

[121] Mullarkey, T., Peters, JJP., Downing, C., and Jones, L., *Using Your Beam Efficiently: Reducing Electron Dose in the STEM via Flyback Compensation*, Microscopy and Microanalysis **28** (2022), 1428–1436.

[122] IDES Inc., , *EDS True Area Scan*, https://ides-inc.com/products/eds/, Accessed August 23.

[123] Hÿtch, M., Snoeck, E., and Kilaas, R., *Quantitative measurement of displacement and strain fields from HREM micrographs*, Ultramicroscopy **74** (1998), 131–146.

[124] Zhu, Y., Ophus, C., Ciston, J., and Wang, H., *Interface lattice displacement measurement to 1 pm by geometric phase analysis on aberration-corrected HAADF STEM images*, Acta Materialia **61** (2013), 5645–5663.

[125] Peters, JJ., Beanland, R., Alexe, M., Cockburn, JW., Revin, DG., Zhang, SY., and Sanchez, AM., *Artefacts in geometric phase analysis of compound materials*, Ultramicroscopy **157** (2015), 91–97.

[126] Rečnik, A., Möbus, G., and Šturm, S., *IMAGE-WARP: A real-space restoration method for high-resolution STEM images using quantitative HRTEM analysis*, Ultramicroscopy **103** (2005), 285–301.

[127] Sanchez, AM., Galindo, PL., Kret, S., Falke, M., Beanland, R., and Goodhew, PJ., *An approach to the systematic distortion correction in aberration-corrected HAADF images*, Journal of Microscopy **221** (2006), 1–7.

[128] Ophus, C., Ciston, J., and Nelson, CT., *Correcting nonlinear drift distortion of scanning probe and scanning transmission electron microscopies from image pairs with orthogonal scan directions*, Ultramicroscopy **162** (2016), 1–9.

[129] Kell, R., Bedford, A., and Trainer, M., *Scanning Sequence and Repetition Rate of Television Images*, Proceedings of the IRE **24** (1936), 559–576.

[130] Duchon, CE., *Lanczos Filtering in One and Two Dimensions*, Journal of Applied Meteorology **18** (1979), 1016–1022.

[131] Gambini, L., Mullarkey, T., Jones, L., and Sanvito, S., *Machine-learning approach for quantified resolvability enhancement of low-dose STEM data*, Machine Learning: Science and Technology **4** (2023), 015025.

[132] Shibata, N., Seki, T., Sánchez-Santolino, G., Findlay, SD., Kohno, Y., Matsumoto, T., Ishikawa, R., and Ikuhara, Y., *Electric field imaging of single atoms*, Nature Communications **8** (2017), 15631.

[133] Bekkevold, JM., Peters, JJP., Mullarkey, T., and Jones, L., *Retrofitting and Reconfiguring Existing Microscopes for Digital DPC: an Accessible Approach to Low-Dose Phase Mapping*, Microscopy and Microanalysis **29** (2023), 1878–1879.

[134] Peters, JJP., Reed, BW., Jimbo, Y., Porter, A., Masiel, D., and Jones, L., *A New Low-dose STEM Imaging Mode with Probability Driven Intra-pixel Beam Blanking*, Microscopy and Microanalysis **29** (2023), 1754 – 1755.

[135] Reed, BW., Bloom, RS., Eyzaguirre, G., Henrichs, C., Moghadam, AA., and Masiel, DJ., *Electrostatic Switching for Spatiotemporal Dose Control in a Transmission Electron Microscope*, Microscopy and Microanalysis **28** (2022), 2230–2231.

[136] Hohenberg, P. and Kohn, W., *Density functional theory (DFT)*, Physical Review **136** (1964), B864.

Appendix A.

Appendix A

A.1. Reference Generation

Finding the parameters used for correcting the compression artefact requires comparison with an undistorted reference image, with two methods proposed here. The first is comparison with an image captured with a large line flyback time, e.g., 1ms, and the second is through comparison with the right half of the image containing the flyback hysteresis effects. **Figure A.1** show images of a single crystal of silicon captured with a long, 1 ms line flyback time, and a short, 20 μs line flyback time. The results of GPA of both images are also included along with their average strain profiles, with a strain of zero expected from the perfect single crystal [123]. The 1 ms line flyback time image shows zero strain across the entire image, while the 20 μs image is heavily distorted on the left side of the image, further evidenced in the average strain profiles.

With reducing dwell times it may be expected that the distortion free area of the shorter line flyback time image may become unsuitable as a reference, however this

was not found in practice. While less simple in practice than the use of the long flyback time reference, using an reference from the same image that is to be corrected has the added advantages of being captured under the exact same microscope conditions, e.g., aberrations and sample drift. Similarly, where low dwell times are used the SNR is often low and multiframe imaging may need to be used. As the use of any frame alignment during this process will alter the perceived hysteresis effects, directly summing the frames must be used, which leads to image blurring when any stage drift is present. These effects reduce error in the least square fitting procedure and can increase the quality of the fit. Regardless of choice of reference image, the crystallography must be aligned with the image to be corrected.

To generate a reference image from the right half of the same image an oversized reference is produced from self-tiling, similar to the template matching algorithms used in Smart Align [96]. Beginning with the undistorted right half of the image, cross correlation is used to find two non-collinear, non-zero vectors that map the image onto itself. This can be achieved in two steps, first by cross-correlating the top and bottom halves of the undistorted image to obtain one vector, and then repeated with the left and right halves to obtain the other. The image is then tiled using these vectors to produce an area larger than the original image, with this process having the advantage of reducing noise in the reference and minimising any small strain which may still be present. This oversized image is then cross-correlated with the undistorted image so that an aligned image can be extracted from the oversized image, suitable to be use as a reference. This process was shown previously in **Figure 4.5**.

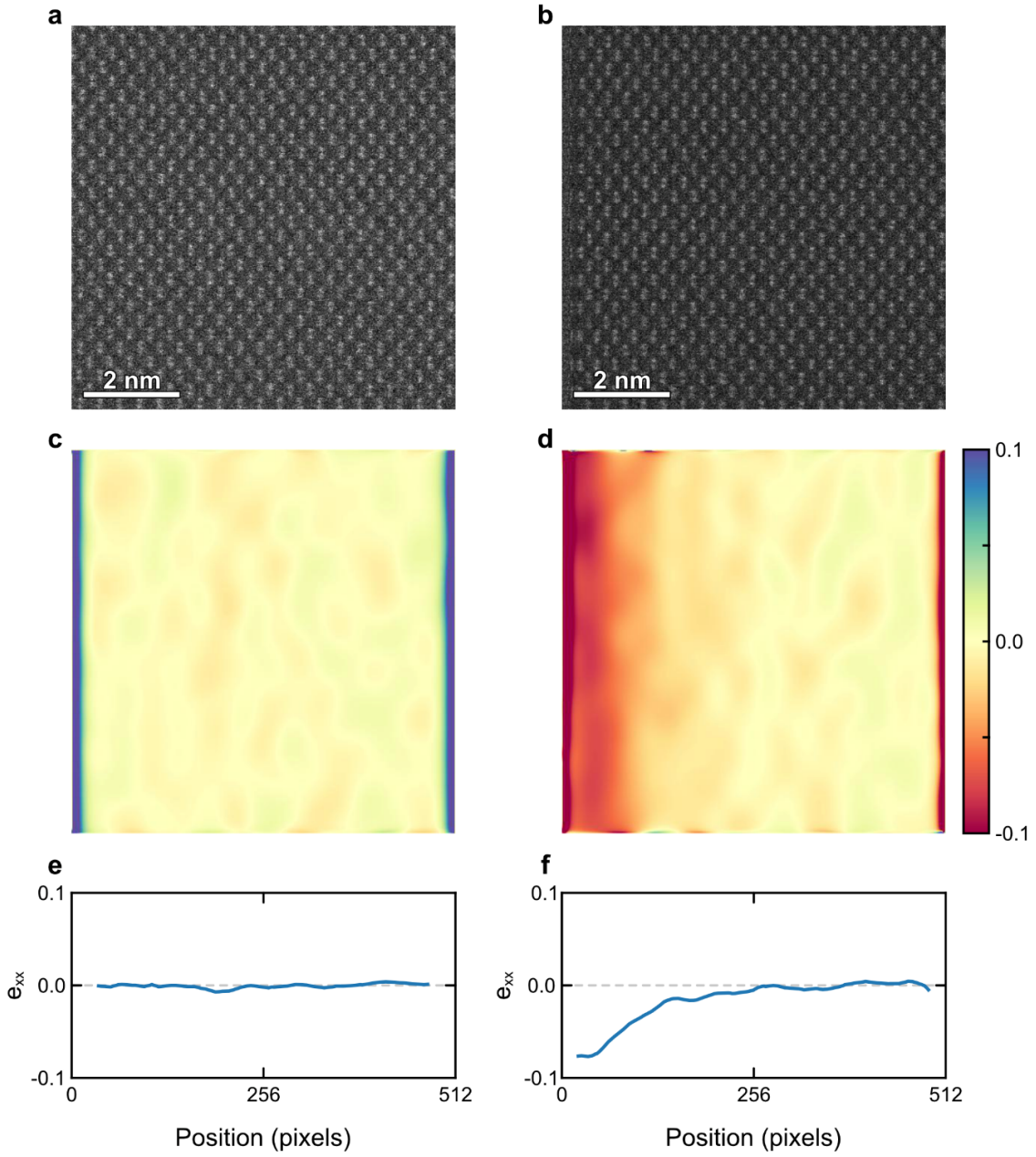

Figure A.1.: HAADF image of Si <110> for **(a)** a 1 ms line flyback time, and **(b)**, a 20 μs line flyback time. Both images were captured using a dwell time of 2 μs, are 512 × 512 pixels in size, and are the sum of five frames. **(c)** and **(d)** show the corresponding e_{xx} distortion maps from **(a)** and **(b)** respectively. **(e)** and **(f)** show profiles of the median distortions from the distortion maps, with edge effects excluded. Image from [121].